Searches for top-antitop resonances in proton-proton collisions at a center of mass energy of 7 TeV with the ATLAS detector

by

Jean-Raphael Lessard
B.Sc., McGill University, 2006

A Dissertation Submitted in Partial Fulfillment of the
Requirements for the Degree of

DOCTOR OF PHILOSOPHY

in the Department of Physics and Astronomy

Searches for top-antitop resonances in proton-proton collisions at a center of mass energy of 7 TeV with the ATLAS detector

by

Jean-Raphael Lessard
B.Sc., McGill University, 2006

Supervisory Committee

Dr. M. Lefebvre, Supervisor
(Department of Physics and Astronomy)

Dr. R. McPherson, Departmental Member
(Department of Physics and Astronomy)

Dr. A. Ritz, Departmental Member
(Department of Physics and Astronomy)

Dr. A. H. Monahan, Outside Member
(School of Earth and Ocean Sciences)

Supervisory Committee

Dr. M. Lefebvre, Supervisor
(Department of Physics and Astronomy)

Dr. R. McPherson, Departmental Member
(Department of Physics and Astronomy)

Dr. A. Ritz, Departmental Member
(Department of Physics and Astronomy)

Dr. A. H. Monahan, Outside Member
(School of Earth and Ocean Sciences)

ABSTRACT

The LHC and the ATLAS detector offer an unprecedented opportunity to test theories beyond the Standard Model of particle physics. Some of these theories predict heavy particles that would decay predominantly into a top and an antitop quark. This thesis presents a technique to experimentally measure the invariant mass ($M_{t\bar{t}}$) of top-antitop pairs, event-by-event, allowing for a complete reconstruction of the $M_{t\bar{t}}$ spectrum. Two different models of heavy narrow resonances were considered: a particle X with a negligible mass width, and a Z′ particle. Under these models, no resonances in the $M_{t\bar{t}}$ spectrum were found in 35.3 pb^{-1} of 7 TeV centre of mass proton-proton collision data. An upper limit on the production cross section times the branching ratio of the heavy particle decaying into a top-antitop (σ_{up}) as a function of its mass (M_X or $M_{Z'}$) was established at a 95% confidence level. Including systematic errors, the observed (expected) σ_{up} at 95% varies from 3.2 pb ($27.9^{+11.3}_{-19.9}$ pb) to 77.7 pb ($9.8^{+10.7}_{-5.6}$ pb) for M_X ranging from 760 GeV to 1000 GeV, and from 2.9 pb ($55.9^{+56.9}_{-47.0}$ pb) to 43.4 pb ($7.8^{+8.9}_{-4.7}$ pb) for $M_{Z'}$ ranging from 700 GeV to 1000 GeV.

Contents

List of Tables

List of Figures

ACKNOWLEDGEMENTS

Life is not a straight path. I feel that every person I had the chance, or mischance, to interact with through the years deserves some credit for this thesis. I obviously will not be able to acknowledge everyone explicitly, but I intend to mention the main protagonists.

I can never be grateful enough towards my parents, Jean Lessard and Maryse Huppé, for providing me with an ideal environment where I could thrive to my full potential. Their constant support transformed my life into a world of exceptional opportunities. I also would like to thank all my siblings, Sandrine, Ludovick and Odre-Anne, for forging my personality and character throughout my childhood. The friends I met during elementary and high school, and that I kept through the years, also played a major part in defining who I am today. Without knowing it, they have been of tremendous help during my Ph.D., allowing me to relieve academic stress and frustration every time I had a chance to visit them in Québec. I must also mention the many teachers and professors who influenced me, especially Chantale Gagnon who taught me physics in my second last year of high school. She inspired me to pursue higher education in physics, and I return the favor by giving her the latest LHC news anytime she invites me for one of her famous vegetarian dinners. A lot of my initial passion for physics also comes from the good friends I had as an undergraduate student at McGill. The multiple discussions we had regarding the fundamental nature of the world were extremely enlightening intellectually. The parties were good too. Lastly, in the list of people who are not directly linked to my research but played a beneficial role for my mental health, I would like to acknowledge all the people in the physics department at UVic and the people at CERN who became good friends of mine. They made everyday life, both in Victoria and Geneva, a lot more enjoyable. A special mention goes to Lorraine Courneyea for sharing time both at UVic and CERN, and for agreeing to review my thesis.

If the people mentioned above are largely responsible for the man I am today, Dr. Lefebvre is largely responsible for the professional I have become. Any remaining weakness in my professional profile should be attributed to me uniquely, as I consider Dr. Lefebvre a model of professionalism. Many will say that he has an unconditional passion for physics; this is true. However, I realized through the years that it goes well beyond this; he has an unconditional passion for work being done to the highest standard. The foremost lesson he taught me is: “It is not because everybody else is

doing it wrong that you have to do it wrong too." Dr. Lefebvre has been extremely patient on the multiple occasions that I stubbornly argued certain topics with him. The point is not that he ended up being right most of the time, but rather that by letting me argue at length, I learned more than any lecture could ever have achieved. I hope he got something out of it too. I am also grateful to Dr. Lefebvre for the invaluable tips he provided on how to write papers and applications. I think this explains why I was so successful applying for scholarships. I also enjoyed the personal interactions I had with Dr. Lefebvre, especially when he would enrich the conversation with one of his diverse french expressions or historical references.

There are many other people I would like to acknowledge at a professional level. This includes all the people on ATLAS, especially those in the UVic group, for their help on various topics. It also includes the people in the ATLAS Top, Exotic and Jet/$E_{\mathrm{T}}^{\mathrm{miss}}$ groups for their feedback on many aspect of my research. I also want to thank everyone who participated in developing the Top EDM with me, with a special mention to A. Gaponenko who helped debug my code on multiple occasions. I would also like to acknowledge all the people I had the chance to work with in the Jet/$E_{\mathrm{T}}^{\mathrm{miss}}$ Data Quality group. This includes R. Seuster who provided me with the initial code that became the jet monitoring software and all the people that joined me later (in order that they joined): M. Consonni, R. Rezvani, M. Petteni, M. Kim, I. Pedraza and E. Ouellette.

Finally, I am extremely grateful to the institutions and private donors that funded me during my Ph.D. through the following scholarships: M.A. & D.E. Breckenridge Graduate Awards, David F. Strong Scholarship, Nora & Mark deGoutire Memorial Scholarship, NSERC Postgraduate Scholarship, President's Research Scholarship, R.M. Pearce Memorial Fellowship, NSERC Alexander Graham Bell Canada Graduate and the University of Victoria Fellowship.

God doesn't play dice
Albert Einstein
Don't tell God what to do with his dice.
Neils Bohr

DEDICATION

Je dédis cette thèse à mes parents, Jean and Maryse, comme étant un petit dividende sur leur investissement.

Chapter 1

Introduction

One of the major achievements of particle physics in the last century was to formulate the Standard Model (SM). The SM is a theory that describes all the known elementary particles and the forces through which they interact. Strong support for the SM followed from its ability to predict fundamental particles before their discovery. To this day, only one postulated SM fundamental particle has not yet been observed experimentally, the Higgs boson. The SM is reviewed in section 2.1.

One way to identify a new massive particle is by reconstructing the invariant mass spectrum of its decay products. A resonance in this spectrum would indicate the presence of a particle with a mass that can be determined by the position of the resonance. One possible decay channel is a top-antitop ($t\bar{t}$) pair. The top and antitop quarks are discussed in section 2.2. In the SM, the only particle predicted to decay into a top and an antitop quark is a suitably heavy Higgs boson. However, Beyond the Standard Model (BSM) theories postulate various particles that could decay into a $t\bar{t}$ pair, section 2.3. The purpose of this analysis is to experimentally reconstruct the top-antitop invariant mass ($M_{t\bar{t}}$) spectrum and search for resonances.

The analysis uses data collected in 2010 with the ATLAS detector at the Large Hadron Collider (LHC), consisting of proton-proton collisions at a center of mass energy of $\sqrt{s} = 7$ TeV. These high energy collisions allow a search for particles with masses above the ElectroWeak (EW) scale; they provide a test of BSM theories featuring particles decaying into $t\bar{t}$. Chapter 3 briefly describes the LHC, the ATLAS detector, and the experimental signatures relevant to this analysis.

Chapter 4 discusses the strategy to ensure that the collected data is of acceptable quality. Chapter 5 then elaborates on the algorithm used to reconstruct $M_{t\bar{t}}$ event-by-event. Both the theoretical motivation underlying the algorithm and its

implementation are discussed in detail.

The data analysis and results are presented in chapter 6. Included in this chapter are the analysis procedure (section 6.1), the performance in reconstructing $t\bar{t}$ (section 6.2), and the final result on the search for $t\bar{t}$ resonances (section 6.3). The results are discussed in chapter 7, before concluding in chapter 8. Appendix A and B are a supplement to chapter 4 on data quality.

Chapter 2

Theory

2.1 Standard Model of Particle Physics

The SM describes the most elementary particles and their interactions. The experimentally observed particles in the SM are shown in Figure 2.1. These particles are believed to be "point like" and therefore irreducible. The SM also postulates the existence of a scalar field, the Higgs field, and the Higgs mechanism. A particularity of the Higgs field is that its expectation value is non-null in vacuum. The Higgs mechanism generates the mass of particles from their interaction with the omnipresent Higgs field. Associated with this field, the SM predicts a Higgs particle. This particle has not been discovered to date. Omitting the unobserved Higgs boson, the SM is considered to be complete given that it explains all the matter and interaction forces measured empirically. Gravity is not part of the SM and is not discussed further.

As shown in Figure 2.1, the known SM particles can be separated in two main groups: matter and radiation. Fermions, particles with intrinsic spin of $\hbar/2$, form matter. They have the property that two particles cannot be in the same quantum state. This is in opposition to vector bosons (intrinsic spin of $\hbar$) that can have the same quantum state. The vector bosons mediate the forces in the SM and therefore form radiation. The Higgs boson is a scalar, it is the only particle with a spin of zero in the SM. It is neither considered matter nor radiation.

The fermions of the SM can be separated further into two groups, quarks and leptons. There are three generations of quarks and leptons. The first, second and third generation correspond to the first, second and third columns in Figure 2.1. Each of the higher generation particles has the same fundamental properties as its

associated particle from the previous generation with the exception that its mass is heavier. The reason why there are three generations of quarks and leptons is not known.

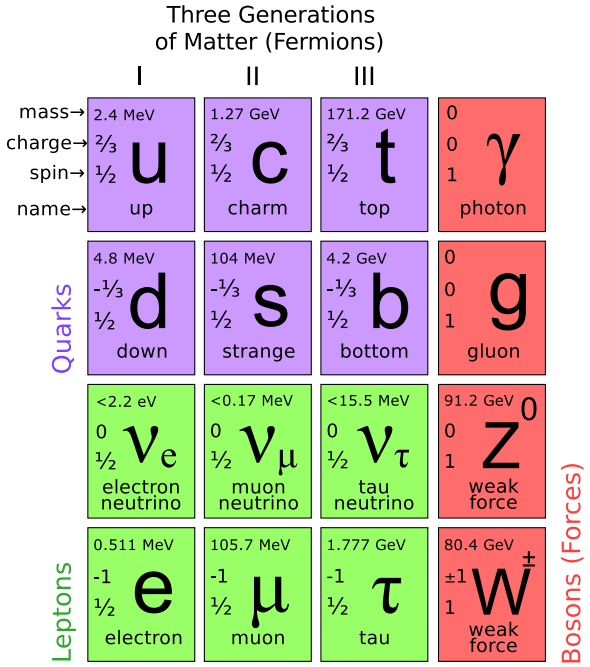

Figure 2.1: Matter (fermions) and radiation (bosons) particles in the SM [1].

2.1.1 Quantum Electrodynamic

The behavior of ElectroMagnetic (EM) charged particles is classically well described by Maxwell's famous equations. Nevertheless, these equations make no attempt at explaining the fundamental origin of the EM forces. With the formulation of quantum theory, these forces could be understood through the exchange of virtual photons between EM charged particles. This is the basis for the theory of Quantum Electro-Dynamics (QED). According to this theory, any observable involving photons and EM charged particles can be calculated perturbatively. In practice, calculation are performed using a pertubative expansion of the scattering amplitudes. The n-th order terms in the expansion series are proportional to α^n, where $\alpha \simeq 1/137$ is the fine-structure constant in the low energy regime[1]. It is therefore possible to obtain

[1]The EM α increases slowly as a function of the energy scale probed. Nevertheless, even for the energies considered at the LHC, $\alpha \ll 1$.

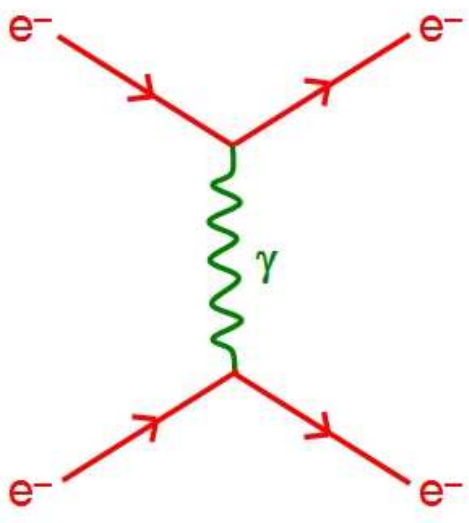

Figure 2.2: The leading order Feynman diagram for $e^-e^- \rightarrow e^-e^-$ scattering. The initial state is on the left of the diagram, while the final state is on the right. Arrows goes from left to right for particles and right to left for antiparticles.

an accurate calculation by using only the leading order terms of the series. Thinking of QED in term of a perturbative sum is useful beyond calculation considerations. Indeed, each term of the sum can be represented schematically by what is called a Feynman diagram. These diagrams provide an intuitive image of the main mechanisms that underlies an EM scattering process. For example, Figure 2.2 shows the leading order Feynman diagrams for the scattering process $e^-e^- \rightarrow e^-e^-$. The diagram shows an exchange of a photon between both electrons.

One of the issues with the perturbative approach in QED is that some diagrams are divergent meaning that the contribution from the term they represent tends to infinity. This issue can be corrected by recognizing that these divergences enter directly into the calculation of the mass and EM charge of the particle(s). It is possible to absorb these divergences by using the experimentally measured mass and charge of the particle(s) involved leaving a finite result. Due to this, QED is said to be a renormalizable theory.

The fundamental particles with an EM charge are the electron, muon and tau leptons with charge of $-e$, the up, charm and top quarks with charge of $+2/3e$ and the down, strange and bottom quarks with charge of -1/3e, where e denotes the elementary charge equivalent to approximatively 1.602×10^{-19} coulombs. For each

EM charged particle, its associated anti-particle (with the same mass) has opposite charge. One of the force carriers, the W boson, has charge of $\pm e$. The photon has no EM charge, but plays a fundamental role in QED by coupling to particles that are EM charged. This is responsible for the repulsive (attractive) force between particles of same (opposite) sign EM charge. The photon is the EM force carrier.

2.1.2 Quantum Chromodynamic

Quantum ChromoDynamics (QCD) is a theory which describes strong force interactions. In QCD, there are 3 charges and each of these charges has a corresponding anti-charge. For convenience, these charges are referred to as red, blue and green and strong force charges are referred to as color charge in general. The combination of a red, blue and green charge results into a neutral (colorless) state[2]. The same is true for the combination of a color charge with its anti-color charge. Every quark carries one unit of color charge. The gluons are responsible for mediating the strong force. However, contrary to photons in QED, gluons have a charge. This means that gluons can couple with each other. This leads to an attractive force between the gluons which then results in color confinement.

Color confinement describes the fact that color charges have never been observed individually. That is, color charged particles are always bound together to form a color singlet state. It is not possible to separate the color charges since the force between them increases with their separation distance. This is because by attracting each other, the gluons do not propagate the strong field evenly throughout space. Most of the field lines (virtual gluons) are concentrated in a line between the interacting strong particles[3]. Having this picture in mind, one could think that the force between the strong particles is constant as a function of their separation distance. However, the fact that a gluon can pair produce into two gluons explains why the force increases. A larger distance between the strong particles results in a greater chance of the production of a gluon pair, yielding more field lines and therefore a larger attracting

[2]To be more rigorous, to have no strong charge, a particle needs to form a color singlet. All color singlets are colorless, but the reverse is not true. For example, there are only eight gluons in the SM and they form a color octet. They therefore all have a strong charge. However, some of the gluons are colorless.

[3]Note that this statement does not contradict how nuclear forces work. In a nucleus, colorless protons and neutrons interact through the strong force in a similar way than Van der Waals forces hold EM neutral molecules together. Strong charge polarization of the colorless nucleons can happen even though the strong field does not propagate evenly throughout space.

force[4]. This is in sharp contrast with QED where the virtual photons are free to propagate throughout space resulting in a force between EM charged particles which is inversely proportional to the square of their separating distance ($F \propto 1/r^2$).

Despite color confinement, it is possible to separate two quarks if extra quarks are created in the process that allow the separated quarks to form color singlets after separation. This is possible since a gluon can pair produce quarks. So when the energy injected to separate the two quarks is large enough, the virtual gluons mediating the strong force between the two quarks start creating extra quarks. These extra quarks can then bind with each other or the initial quarks to form color singlet states. When they do, they stop interacting with the rest of the system[5]. Since the momentum of the virtual gluons is along the axis formed by the two initial quarks, most of the momentum that the extra quarks and later color singlet particles carry is along this same axis. The newly formed particles will end up moving more or less in the same direction as one of the two initial quarks. All the particles that are produced along the direction of a quark are referred to as the jet created by this quark. In general, a jet contains meson particles (a quark bound with its corresponding anti-quark) such as pions and kaons, and baryons (three quarks of different color bound together) such as protons and neutrons. The process of separating two quarks can be easily generalized to separating many quarks and/or gluons. In each case, if sufficient energy is available, there can be one jet created by initial parton (quark or gluon).

QCD calculations can be done perturbatively for interactions at large energies (small distances), but not at small energies (large distances). This is because the perturbation is done in term of the strong coupling constant (α_s) which *runs* from 0.12 to 0.32 for energy scales going from the Z boson mass to 2 GeV. This is in contrast with the EM coupling constant of $\alpha \approx 1/127$ at the Z boson mass energy scale and $\alpha \approx 1/137$ at low energy scale.

[4]For examples of how the strong potential could behave as a function of the separation distance refer to [2].

[5]They can still interact with the system as a color singlet state, as do protons and neutrons in a nucleus. However, this interaction should have only a small impact on the trajectory of the bound state. More importantly, once bounded into a color singlet state, it is not expected that the quarks will be dissociated. In other words, once an hadron in created in the separation process, it is expected to remain to the end of the process.

2.1.3 Electroweak Interactions

The remaining force, the weak force, was unified by Salam, Glashow and Weinberg with the EM force to form the EW theory [3]. Under this theory, the EW force is described using the hypercharge (Y_W) and the weak isospin (T). The EW interactions have to conserve the third component of the weak isospin (T_3). Left-handed fermion particles (negative chirality) have $T_3 = \pm 1/2$ and the right-handed ones have $T_3 = 0$. Under this unification scheme, there is only one lepton and one quark per generation which can take three different values of T_3. So for example, the left-handed electron, right-handed electron and left-handed electron neutrino are the same "electron" but with a T_3 value of +1/2, 0 and -1/2 respectively. The neutrino is massless in the SM while the electron is not. The difference in the mass of the particles is caused by the different coupling strengths with the Higgs boson, Yukawa's couplings. The W^+ and W^- bosons carry a value of $T_3 = 1$ and -1 respectively. Therefore, when a W^+ (W^-) couples to a particle of $T_3 = +1/2$ (-1/2), it will change it into a particle which has a T_3 of -1/2 (+1/2). That is, W bosons can change electrons into electron neutrinos and vice versa. The same is true for the other generations of leptons as well as the three generations of quarks; for example an up quark can be changed into a down quark. The W bosons couple only to left handed particles and carry no hyperweak charge. The Z boson, with $T_3 = 0$, couples to particles through their weak isospin and hypercharge without changing the weak isospin or the hypercharge of the particles. The same is true for the photon. The photon mediates the EM force with the electric charge of a particle given by

$$Q = T_3 + \frac{Y_W}{2} \quad . \tag{2.1}$$

The photon does not couple to neutrinos.

Within a generation of leptons, there exists a unique mapping between the values of T_3 and Y_W, and the particle type (electron vs electron neutrino for example) and whether the particle is chiral-right or chiral-left. In this thesis, type and chirality will be used to describe a particle.

The heavy masses of the W and Z bosons limit the range of the weak interaction and, effectively, its strength. This is actually the origin of the name "weak force". The neutrinos are the only SM particles that only interact through the weak force. As a consequence, the neutrinos interact weakly between themselves or with other particles. Experimentally, it makes their detection difficult.

When the SM was formulated, the neutrino was thought to be massless. In recent years however, it was found that neutrinos in free space can oscillate between their "generation" flavors; an electron neutrino can become a muon neutrino or tau neutrino and so on. This means that the neutrinos mass eigenstates are not the same as the neutrino flavor eigenstates. It constitutes a proof that neutrinos actually have a mass.

2.2 Top Quarks

The discovery of the top quark in 1995 at Fermilab was an important milestone for the SM. It completed the third (and last) family of quarks. Its high mass ($M_{top} = 172.5 \pm 2.6$ GeV) is the highest of all known elementary particles, about a factor of two higher than the EW bosons [3]. As a consequence, no particles in the SM decay into a top-antitop quark pair ($t\bar{t}$). The Higgs boson could be an exception, but only if its mass is twice the top quark mass.

However, many new theoretical models propose to enlarge the SM with new heavy particles. These models are refereed to as BSM theories [4]. Technicolor and extra spatial dimensions are examples of BSM theories in which heavy new particles could decay into $t\bar{t}$. Before considering details of BSM theories, the properties of the process $pp \to t\bar{t}$ within the SM will be explored.

2.2.1 Top Production

The processes that generate a top-antitop quark pair from proton-proton collisions ($pp \to t\bar{t}$) are well known in the SM. The main Feynman diagrams that contribute to the top-antitop cross section ($\sigma_{t\bar{t}}$) are shown in Figure 2.3, where gluons (g) or quarks (q) come from the protons.

Top quarks can also be produced individually (single top production). The leading processes that can create single top in proton-proton collisions are $pp \to t\bar{b}$, $pp \to tW$ and $pp \to tq$. When the $\sqrt{s}$ of the pp collision is 7 TeV, the cross section for single top production is about half the $t\bar{t}$ cross section production, 90^{+32}_{-22} pb (t-channel only)[6] [6] versus $171 \pm 20(\text{stat.}) \pm 14(\text{syst.})^{+8}_{-6}(\text{lum.})$ [7].

[6]The t-channel is the dominant contribution to single top production.

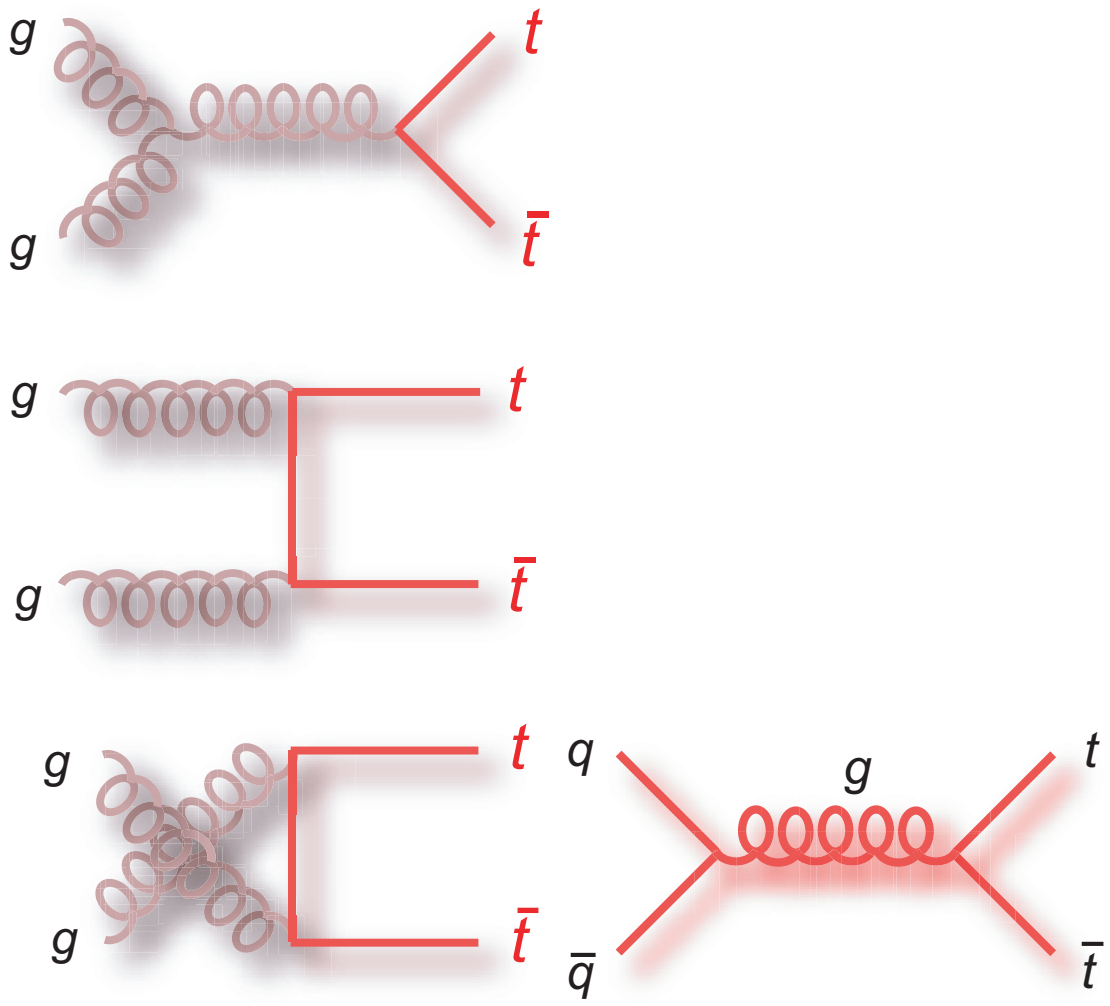

Figure 2.3: Leading order Feynman diagrams for the process $pp \to t\bar{t}$ [5].

2.2.2 Decay of $t\bar{t}$

Once produced, the top quark[7] is highly unstable with a lifetime of 5×10^{-25} s [8]. This is about 20 times shorter than the timescale for strong interactions. A top quark will therefore decay before it starts hadronizing. More than 99% of the time, the decay products will be a W boson and a bottom (b) quark. Then, the W boson can either decay into a pair of light quarks (hadronically) or into a lepton-neutrino pair (leptonically). The overall decay channel for the top pair is therefore characterized by the way the W^+ from the top quark and W^- from the antitop quark decay. The fully hadronic (alljets) channel refers to both W bosons decaying hadronically. The lepton + jets channel is when one W boson decays hadronically while the other decays leptonically. Finally, the dileptons channel is when both W bosons decay leptonically. The branching ratio for each of these channels is presented in Figure 2.4.

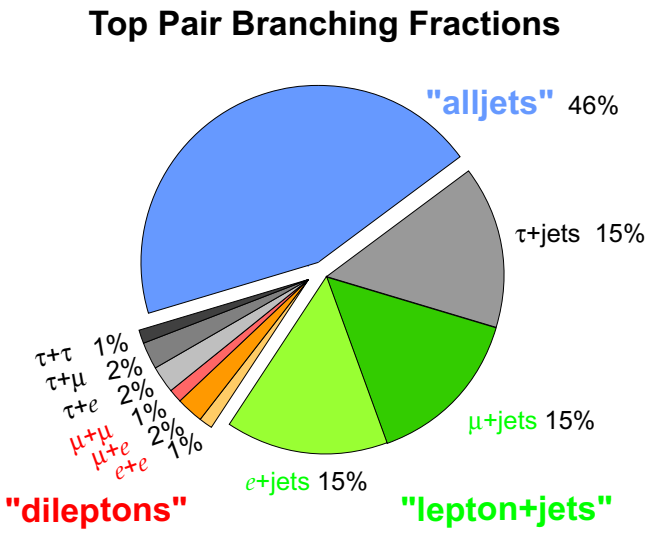

Figure 2.4: Branching ratio of the different decay channels of a top pair event [5].

2.2.3 Lepton + Jets Channel

The fully hadronic (6 jets) channel represents a large fraction of the top events, but is difficult to identify experimentally. From QCD, there are many processes that generate events with six or more jets [9]. The cross section for these processes is

[7] Every time a top quark is mentioned, it should be understood that the equivalent is true for the antitop quark.

many orders of magnitude higher than the one for top production. Consequently, it is difficult to separate fully hadronic top events from QCD background events.

The lepton + jets channel typically leaves a signature of 4 jets, a lepton and a neutrino. None of the dominant QCD backgrounds generate a lepton and a neutrino. It is therefore possible to have a sample with high purity when considering the lepton + jets channel. Note, however, that while the electrons (muons) are stable (have life times long enough to be detected), tau leptons decay before reaching the detector. Therefore, hadronic decays of taus are often mis-identified as jets from quarks. For this reason, most of the analyses that use the lepton + jets channel as signal consider only channels with an electron, or a muon, but not a tau. Figure 2.5 shows an example of a Feynman diagram for the lepton + jets process.

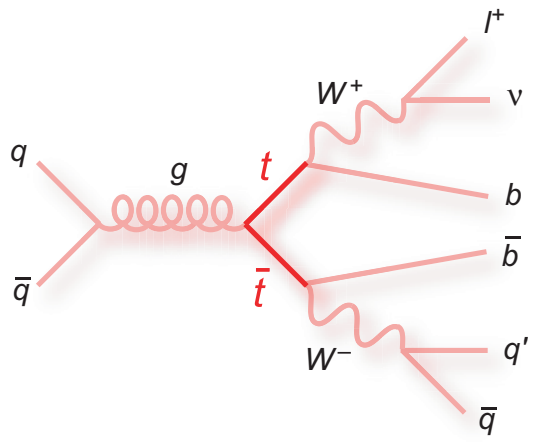

Figure 2.5: Example of a Feynman diagram for a lepton + jets $t\bar{t}$ decay, l stands for lepton (e or μ) [5].

Reconstructing $t\bar{t}$ events from the fully leptonic channel is challenging because of the information lost from having two undetected neutrinos. It can be suitable for $t\bar{t}$ cross section analyses, but it is harder to study parton level quantities such as the invariant mass of the $t\bar{t}$ event.

2.3 Top-Antitop Invariant Mass Spectrum

The top-antitop invariant mass ($M_{t\bar{t}}$) defined in equation (2.2) is an important observable in $t\bar{t}$ events,

$$\mathrm{M}_{\mathrm{t\bar{t}}} \equiv \sqrt{(p^{\mathrm{top}} + p^{\mathrm{antitop}})^2} \ , \tag{2.2}$$

where p^{top} and p^{antitop} are the top and antitop four-momenta[8]. In particular, the $\mathrm{M}_{\mathrm{t\bar{t}}}$ spectrum $\frac{1}{\sigma_{\mathrm{t\bar{t}}}}\frac{\mathrm{d}\sigma_{\mathrm{t\bar{t}}}}{\mathrm{dM}_{\mathrm{t\bar{t}}}}$ can be studied in both SM and BSM contexts.

2.3.1 $\mathrm{M}_{\mathrm{t\bar{t}}}$ Spectrum in the SM Context

Although the processes that generate $\mathrm{t\bar{t}}$ are known, the theoretical cross section $\sigma_{\mathrm{t\bar{t}}}$ has a large uncertainty. This uncertainty on $\sigma_{\mathrm{t\bar{t}}}$ is of the same order of magnitude as the variation of $\sigma_{\mathrm{t\bar{t}}}$ from the uncertainty on the top mass. Therefore, it is not possible to precisely estimate $\mathrm{M}_{\mathrm{top}}$ from a measurement of $\sigma_{\mathrm{t\bar{t}}}$. However, studying the $\mathrm{M}_{\mathrm{t\bar{t}}}$ spectrum opens new possibilities. It has been shown [10] that the mean of $\mathrm{M}_{\mathrm{t\bar{t}}}$, $\langle \mathrm{M}_{\mathrm{t\bar{t}}} \rangle$, is strongly correlated to the mass of the top quark:

$$\frac{\Delta \mathrm{M}_{\mathrm{top}}}{\mathrm{M}_{\mathrm{top}}} = 1.2 \frac{\Delta \langle \mathrm{M}_{\mathrm{t\bar{t}}} \rangle}{\langle \mathrm{M}_{\mathrm{t\bar{t}}} \rangle} + 0.005 \ , \tag{2.3}$$

where $\Delta \mathrm{M}_{\mathrm{top}}$ is the uncertainty on the top mass $\mathrm{M}_{\mathrm{top}}$ inferred from a measurement of $\langle \mathrm{M}_{\mathrm{t\bar{t}}} \rangle$ with uncertainty $\Delta \langle \mathrm{M}_{\mathrm{t\bar{t}}} \rangle$. A measurement of $\langle \mathrm{M}_{\mathrm{t\bar{t}}} \rangle$ with a 1% statistical uncertainty would result in a 1.7% uncertainty on $\mathrm{M}_{\mathrm{top}}$ [10]. This assumes a full reconstruction of the $\mathrm{M}_{\mathrm{t\bar{t}}}$ distribution. Experimental considerations, such as removing background from signal, will reduce the detector efficiency of $\mathrm{t\bar{t}}$ events. Having a partially reconstructed $\mathrm{M}_{\mathrm{t\bar{t}}}$ spectrum will slightly reduce the power to probe $\mathrm{M}_{\mathrm{top}}$. This technique offers a cross check of $\mathrm{M}_{\mathrm{top}}$ obtained with more direct approaches.

2.3.2 $\mathrm{M}_{\mathrm{t\bar{t}}}$ Spectrum in the BSM Context

For many BSM theories, the $\mathrm{M}_{\mathrm{t\bar{t}}}$ spectrum is the key observable. Indeed, due to the high mass of the top quark, some heavy BSM particles would primarily decay into a top-antitop quark pair. The Topcolor Z′ (leptophobic or not) [11] and Kaluza-Klein(KK)-gluon/graviton [12]/[13] are examples of such BSM particles that would reveal themselves as resonances in the $\mathrm{M}_{\mathrm{t\bar{t}}}$ spectrum. Figure 2.6 and 2.7 show how the $\mathrm{M}_{\mathrm{t\bar{t}}}$ distribution would be affected. Note that the mass and width of these resonances

[8] A clear notation is required to appropriately differentiate the various type of vectors throughout the thesis. Multidimensional Euclidean vectors are identified using bold notation, $\mathbf{v}$. For a three-dimensional Euclidean vector an arrow is used, $\vec{v}$. For a four-momentum, the italic letter p is used. A superscript label is used to differentiate between four-momenta.

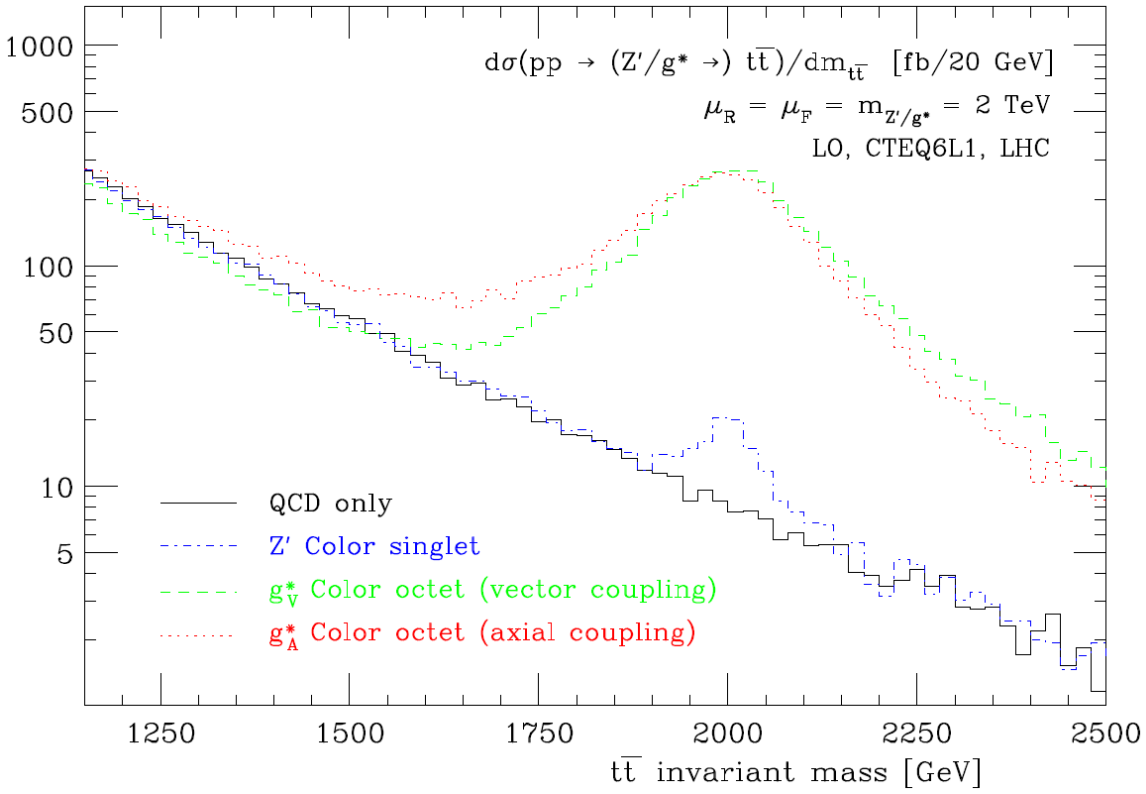

Figure 2.6: $M_{t\bar{t}}$ spectrum for different resonances at 2 TeV: Z′ color singlet in blue and color octet vector (axial) coupling in green (red) [10]. The y-axis is $d\sigma(pp \to (Z'/g^* \to)\ t\bar{t})/dM_{t\bar{t}}$ in units of fb/20 GeV.

are model dependent and somewhat arbitrary at this stage. For more models, see [10].

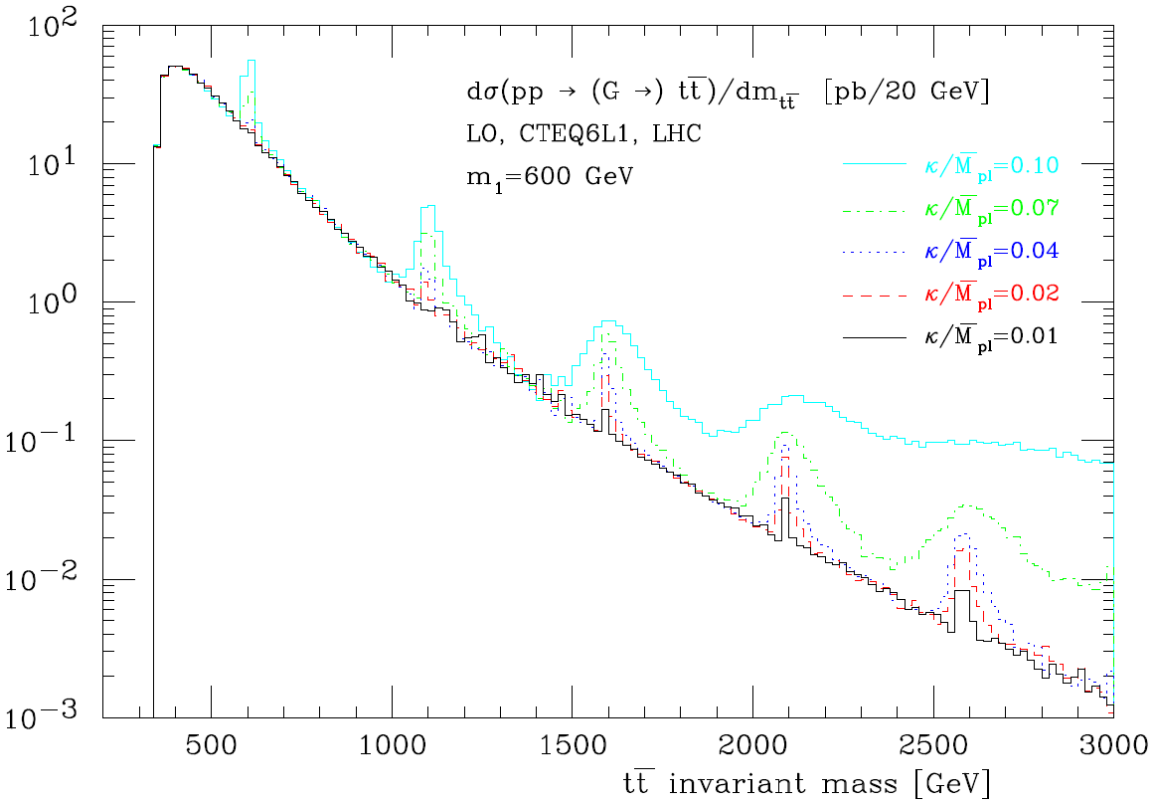

Figure 2.7: $M_{t\bar{t}}$ spectrum in the presence of KK-gravitons. The first mass (600 GeV) is arbitrary while the masses of the other KK-gravitons follow from the zeros of the Bessel function $J_1(x)$ [10]. The y-axis is $d\sigma(pp \to (G \to)\ t\bar{t})/dM_{t\bar{t}}$ in units of pb/20 GeV.

Chapter 3

Experiment

3.1 Large Hadron Collider

3.1.1 Experiment Set Up

The Large Hadron Collider (LHC) is an underground particle accelerator ring that started operating in November 2009. Its large circumference of 27 km and its powerful superconducting dipole magnets designed to provide 8.4 T will eventually allow proton-proton[1] (pp) collisions at a center of mass energy of $\sqrt{s} = 14$ TeV. To reduce the risks of hardware failure, the dipole magnets are not yet operating at maximum power. A major shut down, planned in 2013, will be needed to improve the dipole magnet connections and related quench protection hardware to allow the LHC to reach the design beam energy. The LHC operates at $\sqrt{s} = 7$ TeV since the 30th of March 2010. This is the highest $\sqrt{s}$ ever recorded in the laboratory.

The high $\sqrt{s}$ is not the only impressive feature of the LHC. Its large instantaneous luminosity ($\mathscr{L}$), designed to be $10^{34}\text{cm}^{-2}\text{s}^{-1}$, ensures that analyses requiring many events (collisions) can be performed within a reasonable period of time. The rate R of events observed for a given process is given by,

$$R = \epsilon\sigma\mathscr{L} \quad , \tag{3.1}$$

where ϵ is the detection efficiency and σ is the cross section. The corresponding total number of events (N) is given by

[1] The LHC can also collide heavy ions, but this aspect of the experiment will not be discussed in this thesis.

$$N = \epsilon\sigma\mathcal{L} \ , \tag{3.2}$$

where $\mathcal{L} \equiv \int \mathscr{L} \mathrm{dt}$ is the integrated luminosity. While the cross section is a fixed, measurable quantity, the luminosity and the efficiency are determined by the LHC and the detector respectively. For the 2010 LHC data period, $\mathscr{L}$ varied roughly between 10^{30} and 10^{32} $\mathrm{cm}^{-2}\mathrm{s}^{-1}$.

At the LHC, collisions occur at four interaction points, each one housing a detector: the A Toroidal LHC ApparatuS (ATLAS), CMS, LHCb and ALICE detectors. ALICE was designed to reconstruct heavy ions collisions, LHCb specializes in analyzing b-quark physics, while ATLAS and CMS are multipurpose detectors. The analysis presented in this work is performed on data collected by the ATLAS detector. The total delivered integrated luminosity in 2010 at the ATLAS detector was 48.1 pb^{-1}.

3.1.2 Physics of Proton-Proton Collision

A proton is composed of three valences quarks, two up quarks and one down quark, that are confined together by the strong force. This strong force is mediated by virtual gluons that can pair produce into virtual quarks or gluons (partons). These virtual partons can be probed in sufficiently high energy processes, such as proton-proton collisions at the LHC. In fact, most hard scatters at the LHC are between gluons; but hard scatters of sea and valence quarks are also possible. It is therefore important to know the probability of finding a given type of parton in the proton since quark-quark hard scattering will lead to different processes compared to quark-gluon or gluon-gluon hard scattering. The production processes are also affected by the relative momentum of the colliding partons. For a given energy scale Q, the parton density functions dictate the probability density $f(x)$ of finding a type of parton with a fraction x of the proton's momentum. The parton density functions cannot yet be computed since they are not in the perturbative domain of Quantum ChromoDynamics (QCD); they are established empirically. An example of parton density function for $Q = 2$ GeV is shown in Figure 3.1.

The parton density functions also depend on the value of Q; this scaling violation is a consequence of QCD. Hard scattering of partons with large x most likely involve the valence quarks (up or down), with a up quark being about twice more likely than a down quark. Processes involving partons with small x are dominated by a gluon interacting with another gluon. At the LHC, most of the production processes

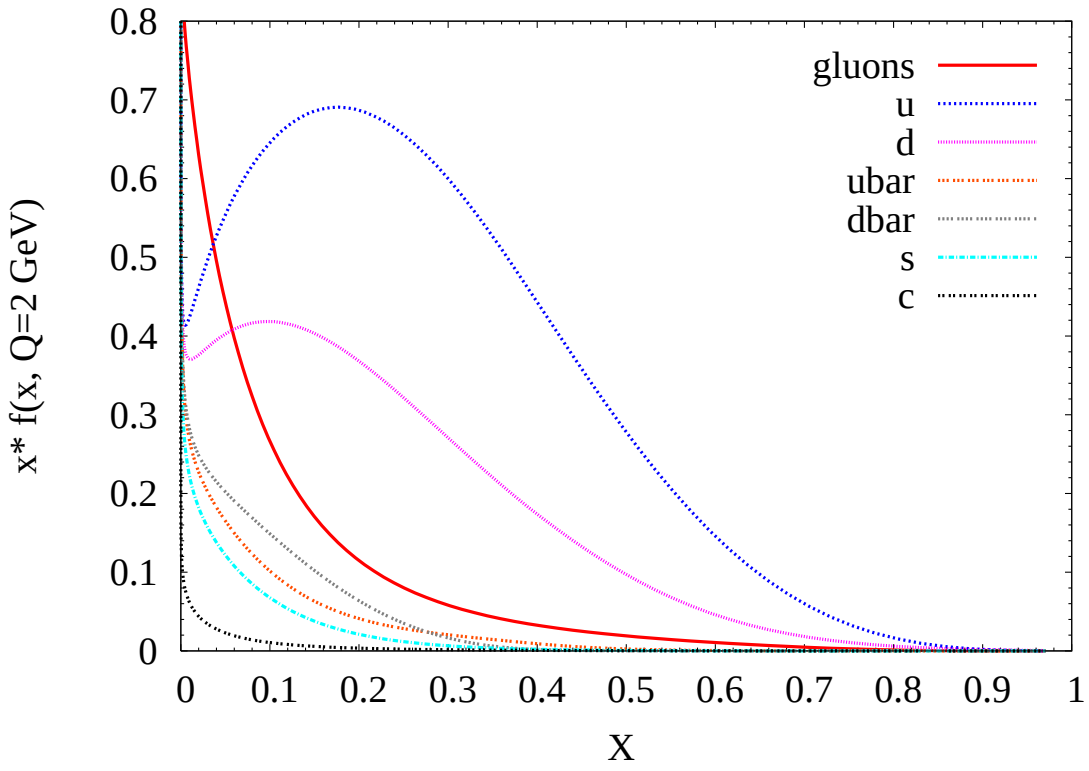

Figure 3.1: Example of parton density function with $Q = 2$ GeV. The u, d, s and c refer respectively to up, down, strange and charm quarks while the ubar and dbar refer to anti-up and anti-down quarks [14].

studied are at the ElectroWeak (EW) scale where Q is of the order 100 GeV. The $\sqrt{s}$ of the collisions at the LHC is approximatively 100 larger than the EW scale, therefore the x of the partons involved in the EW processes must be around 0.01. This small x means that these processes are dominated by gluon-gluon scattering. The valence quarks become more important when studying hypothetical Beyond the Standard Model (BSM) objects with mass closer to $\sqrt{s}$.

Normally in a proton-proton collision, only two partons will hard scatter. The rest of the partons from the two protons undergo small deflections and give rise to a soft spectrum of particles. These particles that are not associated with the hard scattering process but are from the same colliding proton pair; they form what is called the underlying event.

3.2 ATLAS Detector

The ATLAS detector, Figure 3.2, can be divided into three sub-detectors: the Inner Detector (ID), the calorimeter and the muon spectrometer. The ID, composed of the Pixel Detector and SCT/TRT Trackers, enables the reconstruction of charged particle momenta as well as identifying the primary vertices of the event. The calorimeter is divided in two parts, the ElectroMagnetic (EM) calorimeter and the hadronic calorimeter. They measure the energy deposited by EM particles (electrons and photons) and by hadrons (protons, neutrons, charged pions, etc.), respectively. The EM calorimeter is located in the Liquid Argon (LAr) calorimeter, while the hadronic calorimeter is in the end cap region of the LAr calorimeter and in the Tile calorimeter. The muon spectrometer is designed to accurately reconstruct muon momenta. In addition to the three sub-detectors, a magnet system produces the magnetic field required to curve charge particle trajectories, therefore allowing a measurement of their momenta. The solenoid magnet is used by the inner detector while the toroid magnets service the muon detectors. Not shown in Figure 3.2 are forward detectors used to determine the collision luminosity. Finally, the trigger system allows to record only the most interesting events for analysis. The different components of the ATLAS detector are described in more detail in the following subsections. For further details, please refer to [15].

In ATLAS a right-handed coordinate system with the z-axis along the beam pipe is used. The x-axis points to the center of the LHC ring, and the y axis points upward. Cylindrical coordinates (r,ϕ) are used in the transverse plane, ϕ being the azimuthal

angle and r the distance to the origin in the transverse plane. The pseudorapidity is defined in terms of the polar angle θ, as $\eta \equiv -\ln[\tan(\theta/2)]$. Transverse momemtum and energy are defined as $p_{\mathrm{T}} = |\vec{p}|\sin\theta$ and $E_{\mathrm{T}} = E\sin\theta$, respectively. This allows to define the pseudorapidty-azimuthal angle space, also referred to as R space, which has the useful property that a distance in this space, $\Delta\mathrm{R} = \sqrt{\Delta\eta^2 + \Delta\phi^2}$, is invariant under a longitudinal (z-axis) Lorentz boost.

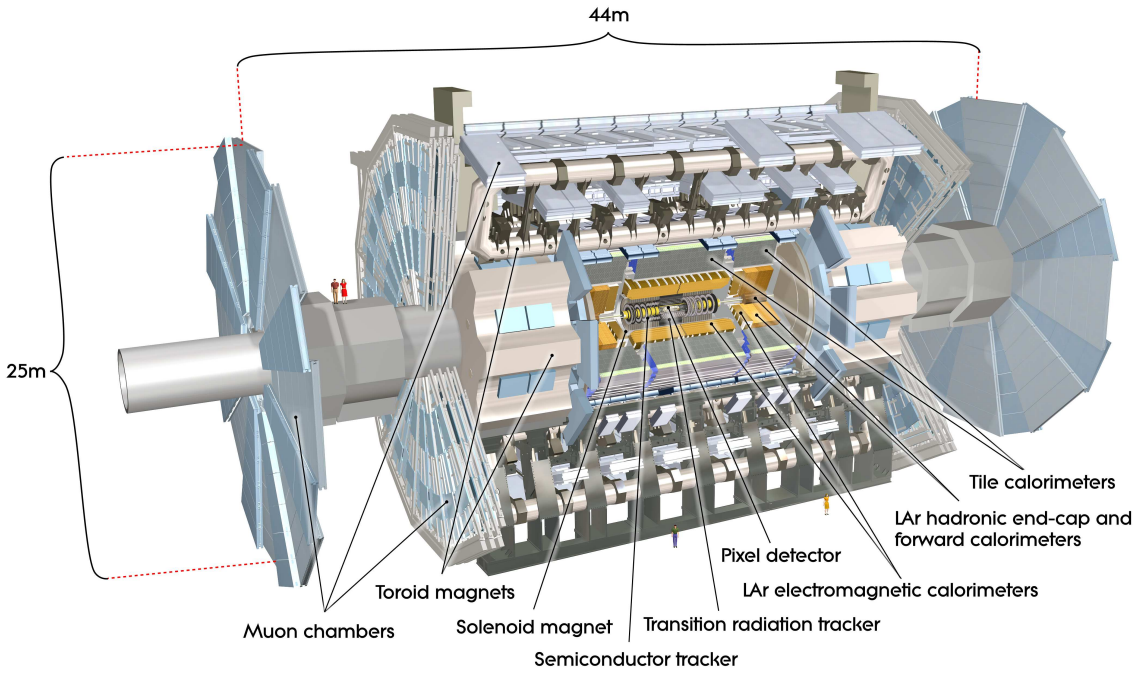

Figure 3.2: Cut-away view of the ATLAS detector where the main sub-detectors are identified as well as the overall dimensions[15].

3.2.1 Inner Detector

The ID, shown in Figure 3.3, measures the momentum of EM particles and finds their common origin (vertex of interaction). This must be achieved with minimal impact on the particles' momenta. To this end, the ID is immersed in a 2 T magnetic field generated by a surrounding solenoid 5.3 m in length and 2.5 m in diameter. The momentum can be deduced from the curvature of each reconstructed track, while the primary vertices of interaction are points where a group of tracks intersect. It is also important to identify secondary vertices created by particles that travel some

distance before decaying. This requires good track resolution in the vicinity of the interaction. Therefore, a silicon pixel detector, with pixel size of 50×400 μm^2, is used to provide an intrinsic accuracy of 10 μm (r $-$ ϕ) and 115 μm (z) over the range 50.5 mm $<$ r $<$ 122.5 mm and $0 < |z| < 650$ mm, where r refers to the perpendicular distance from the center of the beam pipe. Surrounding the pixel detector is the silicon microstrip (SCT) tracker. The SCT uses small-angle (40 mrad) stereo strips to measure both coordinates, with one set of strips, out of eight per layer, parallel to the beam direction measuring r $-$ ϕ. An overall intrinsic accuracy of 17 μm (r $-$ ϕ) and 580 μm (z) can be obtained over the range 275 mm $<$ r $<$ 560 mm and $0 < |z| < 2797$ mm. At the outer edge of the ID is the Transition Radiation Tracker (TRT) composed of straw tubes. It provides r $-$ ϕ intrinsic accuracy of 130 μm per straw in the transverse direction. The straws are 4 mm in diameter and have lengths that vary between 37 cm to 114 cm. The straw hits at the outer radius contribute significantly to the momentum measurement, since the lower precision per point compared to the silicon is compensated by the large number of measurements and longer measured track length. The TRT also enhances electron identification through the detection of transition-radiation photons in the xenon-based gas mixture of the straw tubes. The ID can reconstruct tracks within $|\eta| < 2.5$.

3.2.2 Calorimeter

The calorimeter, Figure 3.4, measures the energy of most particles produced in an event with the exception of muons[2] and neutrinos. ATLAS uses a sampling calorimeter to perform this task. A sampling calorimeter consists of alternating layers of absorber and active material. The goal of the absorber is to contain EM and hadronic showers within a limited depth. The active material measures the energy of the charged particles through ionization. There are two active materials used in ATLAS, LAr and scintillating tiles. The Tile calorimeter surrounds (2.28 m $<$ r $<$ 4.25 m) the LAr calorimeter. Its absorber is steel, for a total Tile calorimeter thickness of 9.7 interaction lengths λ at $\eta = 0$. An interaction length is defined as the mean free path of an hadronic particle. The Tile calorimeter is divided in two parts, the barrel and extended barrel, which cover $|\eta| < 1.0$ and $0.8 < |\eta| < 1.7$ respectively. Its main purpose is the measurement of energy deposited by hadronic showers. The EM LAr calorimeter is mainly used to measure the energy of electromagnetic showers initiated by

[2]The muons leave a small fraction of their energy in the calorimeter.

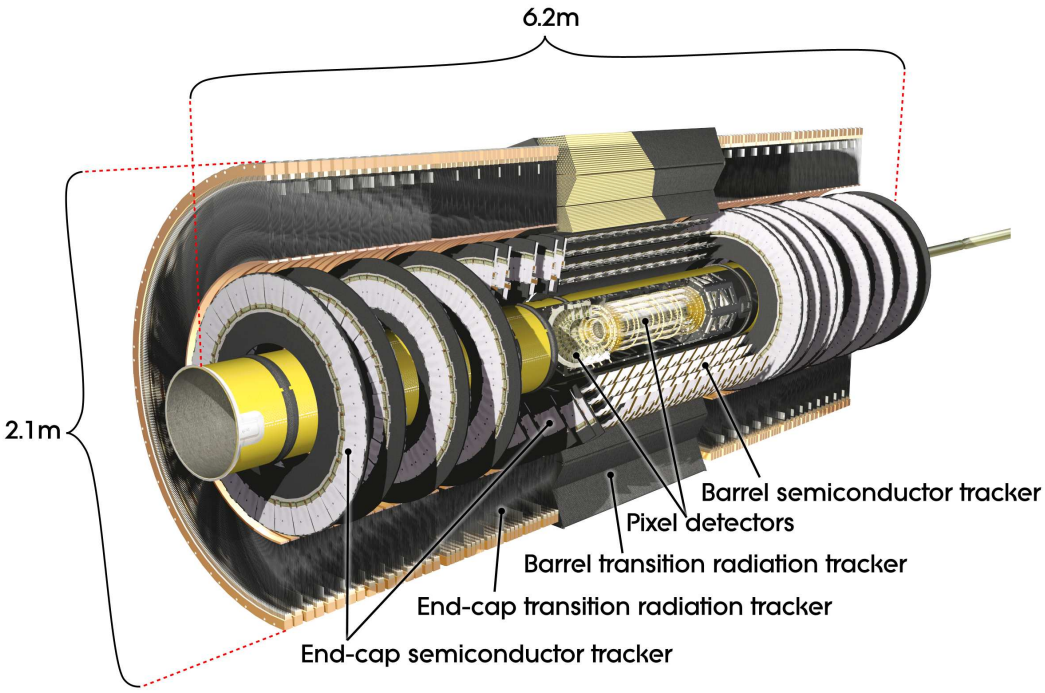

Figure 3.3: Cut-away view of the ATLAS inner detector and its main components [15].

photons and electrons, but a significant fraction of the energy deposited by hadronic showers is also detected. The LAr Hadronic End-Cap Calorimeter (HEC) and the LAr Forward Calorimeter (FCal) are optimised for the detection of hadronic showers. These LAr calorimeters respectively use lead, copper, and copper (first FCAL module) and tungsten (two last FCAL modules). The LAr EM calorimeter is itself divided in two parts, the barrel ($|\eta| < 1.475$) and the end-caps ($1.375 < |\eta| < 3.2$). The gap between the two sections ($1.375 < |\eta| < 1.475$) is often referred to as "the crack region" where the identification of electrons and photons is less accurate. The effective thickness of the LAr EM is greater than 22 radiation lengths (X_0), where X_0 is defined as the mean distance over which an electron will lose all but $1/e$ of its energy. The HEC and FCal are located on each external sides of the LAr EM End-Caps (EMEC) and respectively cover the regions $1.5 < |\eta| < 3.2$ and $3.1 < |\eta| < 4.9$.

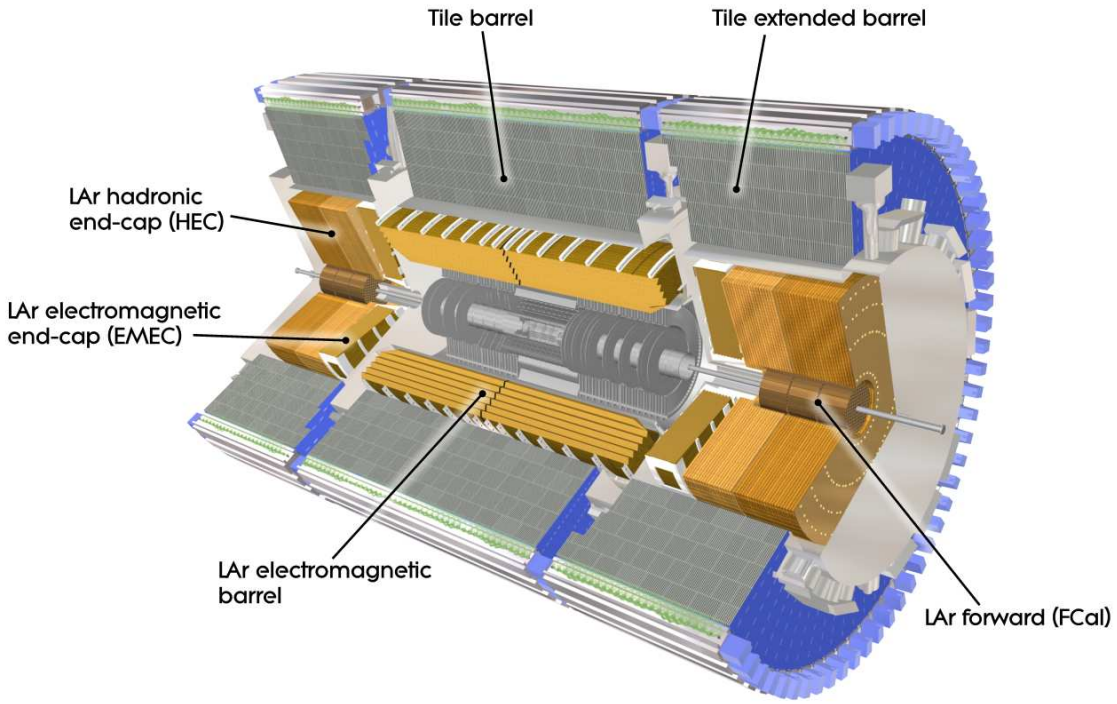

Figure 3.4: Cut-away view of the ATLAS calorimeter system and its main components [15].

The ATLAS calorimeter is a non-compensating calorimeter with $e/h > 1$: electrons and photons have their energy accurately measured, but hadronic particles have their energy systematically under-estimated. The nature of hadronic and EM

showers explain this difference. Hadronic showers undergo nuclear interactions while EM showers do not. A significant fraction of the energy of such interactions goes undetected (invisible energy). For example, it is not possible to detect the binding energy consumed in the nuclear fission of a nucleus. Moreover, the particles composing the hadronic showers are different from those composing EM showers. This leads to a different calorimeter response. Further calibration is therefore required to take into account these two effects and bring the energy of hadronic showers to their correct energy scale, the hadronic scale. There are various techniques to obtain the hadronic scale. The simplest techniques reconstruct observables (such as jets, see subsection 3.3.3) in the calorimeter at the EM scale and then apply global correction factors. More sophisticated techniques calibrate cells locally first and then perform the reconstruction of the observables from calibrated cells.

3.2.3 Muon Spectrometer

The design of the Muon Spectrometer, Figure 3.5, is driven by the large superconducting air-core toroid magnets. These magnets can be separated into the barrel toroid magnets which provide magnetic field over the range $|\eta| < 1.4$, and the end-cap toroid magnets covering the range $1.6 < |\eta| < 2.7$. In between, $1.4 < |\eta| < 1.6$, the magnetic field is weaker and results from a mixture of the barrel and end-cap fields. The purpose of the magnetic field is to bend the trajectory of muons in order to measure their momentum. The orientation of the magnets is such that the magnetic field is perpendicular, as much as possible, to the muons trajectory hence optimizing the momentum resolution. The trajectory is measured through the trigger and high-precision tracking chambers. The principal tracking system which covers most of the η range is the Monitored Drift Tubes (MDT). Each wire in the drift tubes filled with gas is isolated and detects a hit when the gas is ionized by a muon. The other technology employed for track detection are Cathod Strip Chambers (CSC), which were optimized to sustain the higher rate in the $2 < |\eta| < 2.7$ region. The trigger system, $|\eta| < 2.4$, is composed of Resistive Plate Chambers (RPC) in the barrel region and Thin Gap Chambers (TGC) in the end-cap region. The trigger chambers provide bunch-crossing identification and measure the muons coordinate in the direction orthogonal to that determined by the MDT and CSC. The efficiency of the muon spectrometer relies heavily on an accurate mapping of the relative position of the MDT chambers and of the magnetic field. To this end, 1200 precision-mounted

aligment sensors and 1800 Hall sensors are deployed to continually monitor these two maps.

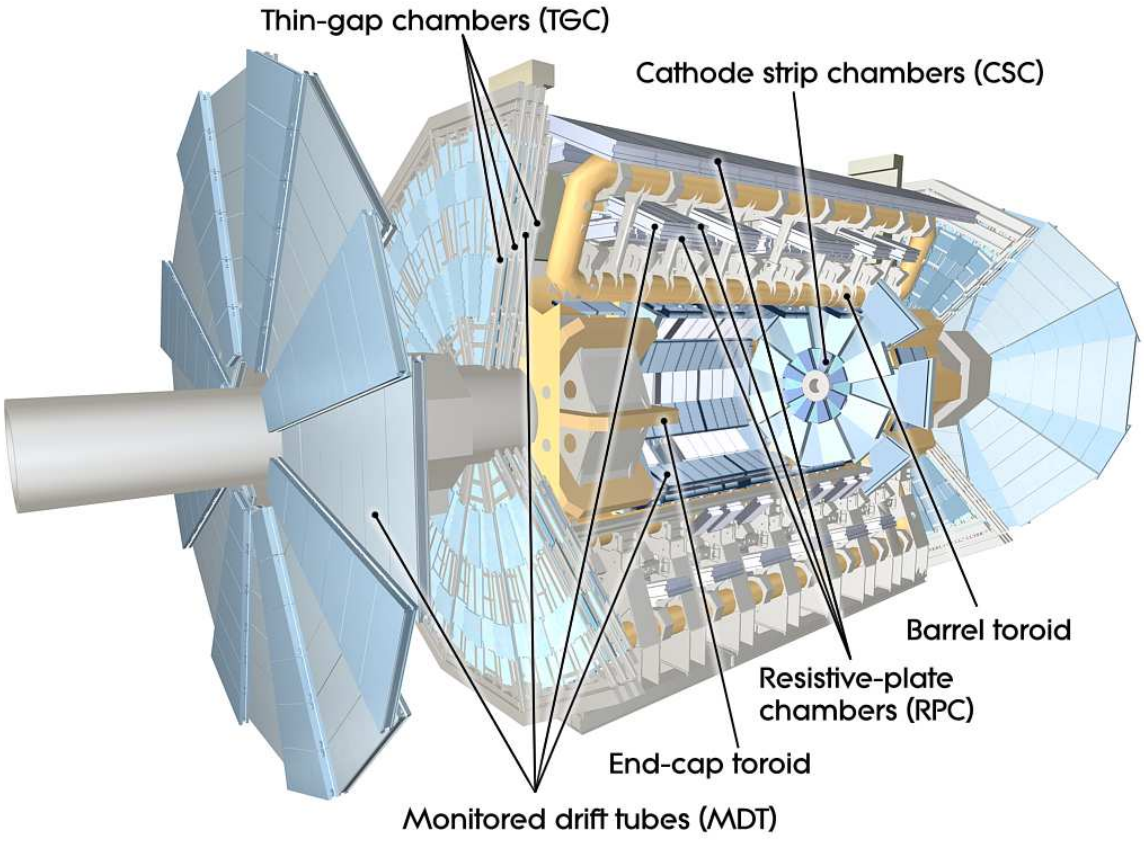

Figure 3.5: Cut-away view of the ATLAS muon system [15].

3.2.4 Forward Detectors

The instantaneous luminosity delivered to ATLAS is measured by two detectors, LUminosity measurement using Cerenkov Integrating Detector (LUCID) and Absolute Luminosity For ATLAS (ALFA). LUCID is located at ±17 m from the interaction point and identifies the relative luminosity through the detection of inelastic pp scattering in the forward direction. This detector is the main online relative-luminosity monitor for ATLAS. ALFA is located further away at ±240 m and is as close as 1 mm to the beam. It allows a better estimation of the absolute luminosity delivered. There is a third forward detector, the Zero-Degree Calorimeter, which is used only for heavy ions collisions.

3.2.5 Trigger

The Trigger and Data Acquisition (collectively TDAQ) system is the infrastructure that allows the recording of the Readout Drivers (ROD) of the multiple ATLAS sub-detector readout channels into a common event. Since at designed luminosity there are over 40 millions collisions per second and an event is of the order of one megabyte (MB) in size, it is impossible to record the information about all collision events. Luckily, only a small fraction of the collisions are of interest for physics analyses. The challenge is to quickly identify these events and discard the others. This task is performed by the trigger system. The task is colossal since it must reduce the event rate from 40 MHz to about 200 Hz. This is achieved through three levels of trigger. The first one, L1 trigger, searches for high p_{T} muons, electron, photons, jets, and other observables of interest. It can only access a small subset of the detector information to make a decision on whether to keep an event or not. In addition to reducing the rate to about 75 kHz, the L1 trigger also identifies Region-of-Interest (RoI). The second level trigger, L2 trigger, then uses the RoIs identified by the L1 trigger to make a more refined decision. It has access to the full detector granularity within each RoI, representing about 2% of the total event information. The L2 trigger must reduce the rate by a factor of 20, to a value of 3.5 kHz. The final trigger decision is made by the event filter, which uses offline analysis procedures on complete events to further reduce the rate to about 200 Hz.

Another system closely related to the TDAQ is the Detector Control System (DCS) that monitors the ATLAS hardware to ensure a coherent and safe operation of the detector. It measures quantities such as temperature, humidity and voltages.

3.2.6 Software

Events that pass the event filter trigger are recorded to disk in a raw data format called Byte-Stream. This data format is then transformed into the Raw Data Object (RDO) format which consists of the same information stored in an object oriented fashion. The raw data of the RDO is then processed into a detailed event reconstruction format, Event Summary Data (ESD). The ESD contains information that allows particle identification, track re-fitting, jet calibration, etc. Finally, the information is further reduced into Analysis Object Data (AOD) to contain only the information needed for most common analyses. For AOD, the targeted memory size per event is about 100 kB. All these data formats (RDO, ESD, AOD) are produced and can be ac-

cessed using a software called ATHENA. This software is also used to perform physics analyses, including Monte Carlo (MC) simulations. There are frequent new versions of the ATHENA software, known as releases. Releases can vary in the exact information stored for the different pool data formats, in the reconstruction algorithms used, and to some extent, in the structure of the program itself. The detector geometry and conditions are stored in a database referred to as LCG conditions database product (COOL). The COOL database is accessed within ATHENA. ATHENA is written in C++ and job options used to modified non-data related input of an analysis are controlled using a python interface.

ATLAS is expected to collect on the order of 10 PetaBytes(PB) of data per year. To process this large amount of data, the Grid, which consists of interconnected computing resources worldwide, is employed. Central to the Grid is the Tier-0 center, located at the European Organization for Nuclear Research (CERN), which processes data as they are acquired by ATLAS. The RDOs are then distributed to several Tier-1 sites around the world, including one in Vancouver, where derived formats can be created. Many of the ESDs and AODs are then distributed to numerous Tier-2 and Tier-3 (user computer) sites around the world to perform physics analyses. Tier-2 sites are also extensively used to produce various MC simulations. The University of Victoria hosts a Tier-2 site.

An important concept related to the processing of the raw data into user accessible formats such as ESDs and AODs is the one of data reprocessing. Examples that could justify a reprocessing of the data are when a new release of ATHENA with significant improvements to the reconstruction algorithms is released, or when the assumed detector geometry in the COOL database changes. Reprocessings are usually performed at Tier-1 sites, a few times per year.

3.3 Experimental Signatures

This section discusses how the final experimental signatures described in section 2.1 are reconstructed from raw data. Only experimental signatures relevant to the lepton + jets channel will be detailed. Moreover, Combined Performance (CP) object will be used interchangeably with experimental signature. The term CP comes from the name given to groups in ATLAS that study experimental signatures. For example, the e/gamma CP group is responsible for the reconstruction of electrons and photons.

3.3.1 Electrons

There are three different algorithms used to reconstruct electrons: one for high p_{T} electrons, one for low p_{T} electrons and another one for forward electrons. Only the reconstruction of high p_{T} electrons will be described since they are used in this analysis. In what follows, *electrons* refer to high p_{T} electrons, excluding foward electrons ($|\eta| > 2.5$).

Electron reconstruction is first seeded by the presence of an energy cluster in the EM calorimeter. This cluster is identified using a sliding window algorithm which consists of searching for an energy above a predetermine threshold contained within a window of $\Delta\eta \times \Delta\phi$. The size of the window can be varied. Once located, refined techniques are used to establish the exact position and energy of the cluster. An electron should leave a track in the inner detector. Consequently, it is required that the identified EM cluster matches a track in the inner detector. That is, the momenta of the track and its position at the EM cluster should be, within experimental uncertainty, the same as the energy and position of the EM cluster. Unfortunately, this requirement is not sufficient in itself to ensure that the signature was caused by an electron. Indeed, charged mesons and baryons contained within a jet will leave tracks in the inner detector. They will also sometime deposit a significant amount of their energy in the EM calorimeter. Many strategies are used to reduce jets faking an electron. First, there should not be a large amount of energy leaking into the hadronic calorimeter. Second, most of the energy of the EM shower energy should be in the second sampling of the EM calorimeter. These two criteria significantly reduce fake electrons from high energy mesons and baryons while maintaining a high efficiency for true electron. However, this is not sufficient to remove all fake electrons. Jets often contain high energy π^0 which decay to two photons. To avoid reconstructing such jets as electrons, it is required that some energy be deposited in the EM presampler. Photons do not deposit energy in the EM presampler because they are not charged and their first interaction often is at the calorimeter. Moreover, since two photons are created by π^0, two energy maxima can sometime be observed within the same shower. This allows to further reduce fake electrons from π^0.

3.3.2 Muons

Contrarily to electrons, muons are not stopped by the ATLAS calorimetry. Muons are 206 times heavier than electrons; Bremsstranhlung radiation is consequently sup-

pressed. A muon will still lose some of its energy in the calorimetry through ionization, but this amount is relatively small for the high momentum muons, $p_{\mathrm{T}} > 20$ GeV, of interest for this study. These muons are Minimum Ionization Particles (MIPs) and the average energy they deposit in the calorimeter is known to be approximatively 3 GeV.

Muon reconstruction therefore relies primarily on the muon spectrometer. The first piece of information used is the presence of a track in the bending plane of a muon station. These segment candidates are required to be consistent with a particle coming from the center of the detector. Two or more segment candidates are joined together to reconstruct a muon track. From the curvature of the track, the momentum of the muon is calculated. The calculation takes into account multiple scattering and energy loss in the calorimeter. This reconstruction is referred to as *stand-alone*.

It is possible to refine this measurement by adding information from the ID; this is referred to as *combined muon* reconstruction. In this case, the reconstructed track in the spectrometer is required to match a track reconstructed in the ID. The muon momentum is then recalculated by either refitting a single track from hits in both the ID and muon spectrometer together or by doing a statistical combination of the momentum measured in the ID and muon spectrometer.

3.3.3 Jets

Jets are fuzzier observables since they are defined by the algorithm used to reconstruct them. That is, there is no fundamental definition of what a jet is. Jets are the observables used as a proxy to the fundamental objects of interest, the hard scattered partons. Comparing the theoretical predictions with the experiment requires that partons can be mapped onto jets. To achieve this, it is the current norm to require that a jet algorithm satisfies two main requirements, infrared safety and collinear safety. Both requirements aim at reconstructing one jet per initial high p_{T} parton. An infrared safe algorithm means that the emission of a soft gluon in between two close by jets should not alter the reconstruction of the two jets. In particular, the two jets should not become merged into a single jet. Similarly, a collinear safe algorithm ensures that one high p_{T} parton will not be reconstructed as two jets because a gluon was emitted collinearly to the jet.

Before going into jet algorithm details, it is important to describe the input. In MC simulations, it is possible to input the list of all stable particle 4-momenta within

an event to the algorithm. From there, the algorithm identifies which particles should be associated to the same jet and calculates the jet 4-momentum from summing the particle 4-momenta. Clearly, the list of particle 4-momenta is not available experimentally. A reasonable alternative is to use a 4-momentum for each calorimeter cell. The energy of a 4-momentum calorimeter cell is given by the energy deposited in the cell, while the direction is given by the position of the cell with respect to the interaction point. The mass is taken to be zero. Since the number of calorimeter cells is about 200 000 in ATLAS, and that most of the cells will have very low energy coming mainly from electronic noise and pileup, it is necessary to pre-cluster cells. They are grouped using topological clusters (topoclusters) [16]. The 4-momenta used as input are often referred to as constituents of the jet algorithm.

Some jet algorithms were developed to satisfy the infrared and collinear safe criteria. The one favored by the ATLAS collaboration and described here is the Anti$-k_{\mathrm{T}}$ algorithm [17]. It is based on the following two equations:

$$d_{ij} = \min\left(\frac{1}{k_{\mathrm{T}i}^2}, \frac{1}{k_{\mathrm{T}j}^2}\right)\frac{(\Delta \mathrm{R})_{ij}^2}{\mathrm{R}^2} \quad , \tag{3.3}$$

$$d_{iB} = \frac{1}{k_{\mathrm{T}i}^2} \quad , \tag{3.4}$$

where $k_{\mathrm{T}i}$ and $k_{\mathrm{T}j}$ refer to the transverse momentum of constituents i and j. The parameter R is set to roughly represent the desired size of the jets in (η, ϕ) space. Therefore, d_{ij} is a momentum weighted distance between constituent i and j. With this definition of distance, d_{iB} can be loosely interpreted to be the distance between the constituent i and the beam pipe. To establish which constituent should be merged into a jet, a list of all the distances d is computed. If d_{ij} is the smallest, constituents i and j are combined and the list is remade. If d_{iB} is the smallest, constituent i is considered a complete jet and is removed from the list. The process is repeated until all constituents belong to a jet. Furthermore, there is a p_{T} threshold of 7 GeV for a jet to be kept after reconstruction.

After the clustering of the constituents into jets, one step remains: the calibration of the jets. There are two criteria useful to compare calibration techniques. One, the Jet Energy Resolution (JER) should be good and uniform as much as possible in η. The resolution (σ) of the jet energy (E) can usually be parametrized using the following equation:

$$\frac{\sigma(E)}{E} = \frac{a}{\sqrt{E}} \oplus \frac{b}{E} \oplus c \ , \tag{3.5}$$

where a is the sampling term, b the noise term, c the constant term and $\oplus$ refers to the quadratic sum of the terms. Notice that these terms are a function of the η of the jets. Moreover, there is a systematic error on the calibrated energy of the jets called Jet Energy Scale (JES) uncertainty.

The favored calibration by the top working group for the 2010 data is called EM+JES. This calibration is fully derived from MC studies to bring the EM jet energy scale to its hadronic energy scale on average. This calibration has a slightly worse resolution and JES uncertainty than more advanced calibration techniques, but has the advantage of being robust and well understood. This is appropriate for the early data period.

3.3.4 Flavor-Tagging

It is sometimes possible to identify the flavor of the quark that hadronized into a jet. This type of identification is called flavor-tagging. It is a function of the mass difference between the quarks. For the three lightest quarks, this mass difference is too small to allow a distinction. However, the charm and bottom quarks have a significant enough mass to leave a special signature in the jet[3]. The heavy quark will bound with another quark during the hadronization to form an heavy meson. This meson will eventually decay to lighter particles. However, the life time of the meson is long enough to travel a detectable distance from the primary vertex before decaying. This secondary vertex can be identified by reconstructing tracks in the ID.

For analyses involving top quarks, tagging b-jets is a powerful tool to reject background events. There are multiple b-tagging algorithms available. For this analysis, a simple robust algorithm called SV0 was used. A tag weight corresponding to the distance between the primary and secondary vertices divided by the error on this distance is assigned to each jet [16]. A decision on whether a jet originated from a b-quark or not can be taken from this tag weight. The threshold (cut) tag weight should be chosen to have an appropriate balance between purity and efficiency. A

[3]Top quarks do not hadronize, but highly boosted tops can yield a single jet that exhibits features, such as substructure and mass, that may allow it to be tagged as originating from a top quarks. The author took part in studies involving such techniques [18], but this will not be discussed in this thesis.

higher cut will lead to a better purity at the cost of a lower efficiency. The tag weight cut used for this analysis was 5.85, chosen to correspond to a b-tagging efficiency of 50%.

MC simulation of b-jets is not modeled well enough to estimate the tagging efficiency. To be able to compare MC to data, one needs to know the Scale Factor (SF) defined as:

$$SF_{\text{Flavor}}(p_{\text{T}}, \eta) = \frac{\epsilon^{\text{Data}}_{\text{Flavor}}(p_{\text{T}}, \eta)}{\epsilon^{\text{MC}}_{\text{Flavor}}(p_{\text{T}}, \eta)} \ , \tag{3.6}$$

where $\epsilon^{\text{Data}}_{\text{Flavor}}(p_{\text{T}}, \eta)$ and $\epsilon^{\text{MC}}_{\text{Flavor}}(p_{\text{T}}, \eta)$ are the tagging efficiencies for a given flavor (for a chosen b-tagging algorithm and cut weight). The flavor is taken from the MC truth. A weight can be assigned to each jets using

$$w_{\text{jet}} = \begin{cases} SF_{\text{Flavor}}(p_{\text{T}}, \eta) & \text{if jet b-tagged in MC} \\ \frac{1-\epsilon^{\text{Data}}_{\text{Flavor}}(p_{\text{T}}, \eta)}{1-\epsilon^{\text{MC}}_{\text{Flavor}}(p_{\text{T}}, \eta)} & \text{if jet not b-tagged in MC} \end{cases} \tag{3.7}$$

Finally, an event weight is defined as

$$w_{\text{event}} = \prod_{\text{jets}} w_{\text{jet}} \ , \tag{3.8}$$

where the product goes over all the jets in the MC event. By applying this weight to the MC events when performing the analysis (filling histograms), the event selection efficiency of the MC should match the one of the data. The systematic error of the SF is of the order of 10%. This usually results in a large systematic uncertainty of the event selection efficiency estimated from MC simulations for analyses that use b-tagging.

3.3.5 $E_{\text{T}}^{\text{miss}}$

When some particles produced in a collision are undetected by the ATLAS detector due to their non-interacting nature, missing transverse energy ($E_{\text{T}}^{\text{miss}}$) is observed. To be unobservable, a particle needs to interact only through weak interaction. In the Standard Model (SM), only neutrinos have this property. Nevertheless, it is not excluded that some BSM particles could exhibit the same behavior, making $E_{\text{T}}^{\text{miss}}$ an important observable for discoveries.

The idea behind $E_{\text{T}}^{\text{miss}}$ is that, due to momentum conservation, the total momen-

tum in the plane transverse to the beam pipe ($\sum_{\text{particles}} \vec{p}_{\text{T}}$) after the collision has to be equal to its value before the collision, namely, zero. If $\sum_{\text{particles}} \vec{p}_{\text{T}}$ is not zero, one or many undetected particles are inferred. In the good approximation that the masses of the detected particles are negligible, $\sum_{\text{particles}} \vec{p}_{\text{T}} = -\vec{E}_{\text{T}}^{\text{miss}}$. The $\vec{E}_{\text{T}}^{\text{miss}}$ is an estimate of the neutrino $\vec{p}_{\text{T}}$ when there is only one high p_{T} neutrino. The longitudinal momentum (p_{z}) of the neutrino remains unknown however.

As for the jets, to estimate $E_{\text{T}}^{\text{miss}}$, the particles are approximated by the calorimeters cells that constitute topoclusters. The $E_{\text{T}}^{\text{miss}}$ is then calculated using:

$$E_{\text{x}}^{\text{miss}} = -\sum_{i} E_{\text{x}}^{i} \ , \quad E_{\text{y}}^{\text{miss}} = -\sum_{i} E_{\text{y}}^{i} \ , \tag{3.9}$$

$$E_{\text{T}}^{\text{miss}} = \sqrt{(E_{\text{x}}^{\text{miss}})^2 + (E_{\text{y}}^{\text{miss}})^2} \ , \tag{3.10}$$

where i runs over all the cells in the topoclusters and, E_{x}^{i} and E_{y}^{i} are the energy of the i-th cell in the x-direction ($E^i \cos\phi$) and y-direction ($E^i \sin\phi$) respectively. The energy of the cells must be adjusted depending on whether the topocluster is associated with a jet or an electron since the calorimetric response is different. Finally, since muons are not detected by the calorimeter, their E_{x} and E_{y} need to be added when calculating equation (3.9). Their energy is taken from their *combined muon* reconstruction and a correction to $E_{\text{T}}^{\text{miss}}$ is applied for the small fraction of energy they deposited in the calorimeter to avoid double counting. When all these corrections are applied to calculated $E_{\text{T}}^{\text{miss}}$, the algorithm is referred to as MET_RefFinal [19]. This is the algorithm used for this analysis.

3.3.6 Overlap Removal

The algorithms that identify the various reconstructed objects created by an event in ATLAS are applied independently. This means that a detector signature can be reconstructed twice as two different objects. This is particularly problematic in the case of electrons since, in addition to be identified by the electron reconstruction algorithm, they are also systematically identified as jets since they form topoclusters in the calorimeter. It is therefore important to remove jets that overlap with electrons. More precisely, jets within a cone of radius 0.2 in ΔR around an electron are removed. When other objects overlap, like a muon with an electron or a jet, the situation is

flagged, but no action is taken. Different analyses will deal differently with these cases. For the analysis described in this thesis, the details about object isolation requirements will be given in section 6.1.4.

Chapter 4

Data Quality

4.1 Data Quality Overview

Problems with the detector hardware or the reconstruction software can lead to the reconstruction of unphysical objects. The aim of Data Quality (DQ) is to remove events with unphysical objects. This is done by specifying a Good Run List (GRL)[1]. GRLs are created from DQ flags that act as traffic lights. Primary DQ flags indicate if the detectors, Combined Performance (CP) objects and triggers were performing well. The CP Data Quality flags are set by looking at the distribution of various observables associated with the CP objects, but without considering the state of the detectors or triggers. The final decision on whether a CP object is good for physics or not is taken by combining the relevant primary DQ flags to form a virtual flag[2]. GRLs are produced by specifying a combination of virtual flags based on the physical objects needed for various analyses.

The status (i.e. green, yellow, red) of the Data Quality flags can evolve with time. In particular, when initially there are DQ problems, but also a potential to correct them, a yellow flag is used. By the time an official GRL is created, each yellow DQ flag must be set green or red. This decision is taken by the DQ experts. To ensure reproducibility, the DQ flags assigned after the first Tier-0 processing and the subsequent reprocessing of the data are tagged and frozen.

It should be noted that the color green does not mean "perfect" but rather "as

[1] A good run list actually specifies the list of good luminosity blocks for each run.

[2] The name comes from the fact that primary flags are saved to the COOL database, while only the combination logic is stored for virtual flags. This ensures consistency between primary and virtual DQ flags.

good as we can get at the current stage of the experiment". Objects from luminosity blocks with green DQ flags might therefore need extra processing at the analysis level to be suitable for physics analysis. Jet cleaning cuts described in section A.4 are examples of such processing.

It should be noted that the DQ group recently evolved away from the concept of flags favoring the concept of defects. The idea is to list, for each run, the potential problems referred to as defects. Later on, the experts can decide which defects can be tolerated and which cannot; the color green or red can be assigned to each run. This greatly improved the flexibility in assessing the DQ of the runs and removed the ambiguity that the yellow flag could cause. The experts no longer need to review one by one the runs flagged yellow by the shifters. The users can therefore have access to data more rapidly.

Another change that occurred as the LHC runs started to be increasingly stable is the use of a 36 hour calibration loop. The principle is to present the DQ shifters and experts with a subset of the data that can be rapidly reconstructed through the *express stream*. Based on their observations, an attempt is made to fix any defects before the bulk reconstruction of all the data is launched 36 hours later. For example, if a detector channel becomes very noisy, the DQ group could decide to mask this channel before the start of the complete reconstruction of the events for the run. Before the introduction of the 36 hours calibration loop, the fix could only be applied to successive runs and the defect(s) in the run could only be recovered months later when all the runs would be reprocessed.

4.2 Jets Data Quality

This section is dedicated to how the DQ for the jets is established. An emphasis is put on jets DQ not only due to the importance of jets in the reconstruction of tops, but also because the author was significantly involved in this task. At the beginning of the 2010 data period, the concept of DQ on CP objects (such as electrons or jets) was in its infancy. Only the detectors status was reported run by run. The Jet/$E_{\mathrm{T}}^{\mathrm{miss}}$ group was the first of the CP group to implement a strategy to asses DQ. Today, there are five experts and over 50 shifters ensuring, run by run, that the jets are suitable for physics analysis.

The jet DQ assessment relies almost entirely on monitoring the distributions of jet observables. The corresponding histograms are centrally published on the web

using the web-display interface created by the DQ group. This tool is first used by the shifters to identify problems. In the first months of collision, each monitored distribution had to be checked by the shifter. The identification of defects would rely entirely on the shifter's ability to spot anomalies in the distributions. As a reference, the distributions of a previous run judged good would be overlaid to the current run distributions. This reference could, however, be misleading since the run conditions could change significantly from run to run in early data taking. As the run conditions stabilized with time, the reference became more and more reliable to the point where algorithms that compare distributions to their reference could be used. However, the thresholds to flag a discrepancy need to be optimized; there might be features indicating a problem in the distributions that the algorithms cannot identify because this problem had not been considered when designing the algorithm. For these reasons, today, a shifter is still needed to confirm the outcome of the automatic checks. The shifter then reports his/her observations to the central ATLAS e-log. There are two 4-hours Jet/$E_{\mathrm{T}}^{\mathrm{miss}}$ shifts per day.

The problems reported are then analyzed by one of the Jet/$E_{\mathrm{T}}^{\mathrm{miss}}$ expert. The role of the expert is to confirm whether or not the problems found are significant enough to warrant a deeper investigation. Following this investigation, if possible, a fix should be implemented. A bug tracker called Savanah is used to do the follow-up of the reported problems. Since most of the problems observed in jet DQ are a consequence of a problem with the detector, the Jet/$E_{\mathrm{T}}^{\mathrm{miss}}$ experts need to work in close collaboration with the DQ experts of the various detectors. The solutions can be as simple as requesting a noisy cell to be masked, or as complex as modifying the jet reconstruction algorithm. The time needed to implement the fix will vary according to the complexity. As a result, not all the problems can be fixed before the bulk processing of the data starts, and later reprocessing of the data is still sometimes needed.

An overview of the jet DQ monitoring software is presented in appendix A. This appendix contains an extensive list of all the histograms and algorithms used to identify jet defects. An example histogram is shown in Figure 4.1. This simple distribution of the number of jets as a function of η and ϕ for a given run is used extensively to identify problematic regions in the detector. For example, a significant excess in a bin could indicate the presence of a noisy cell.

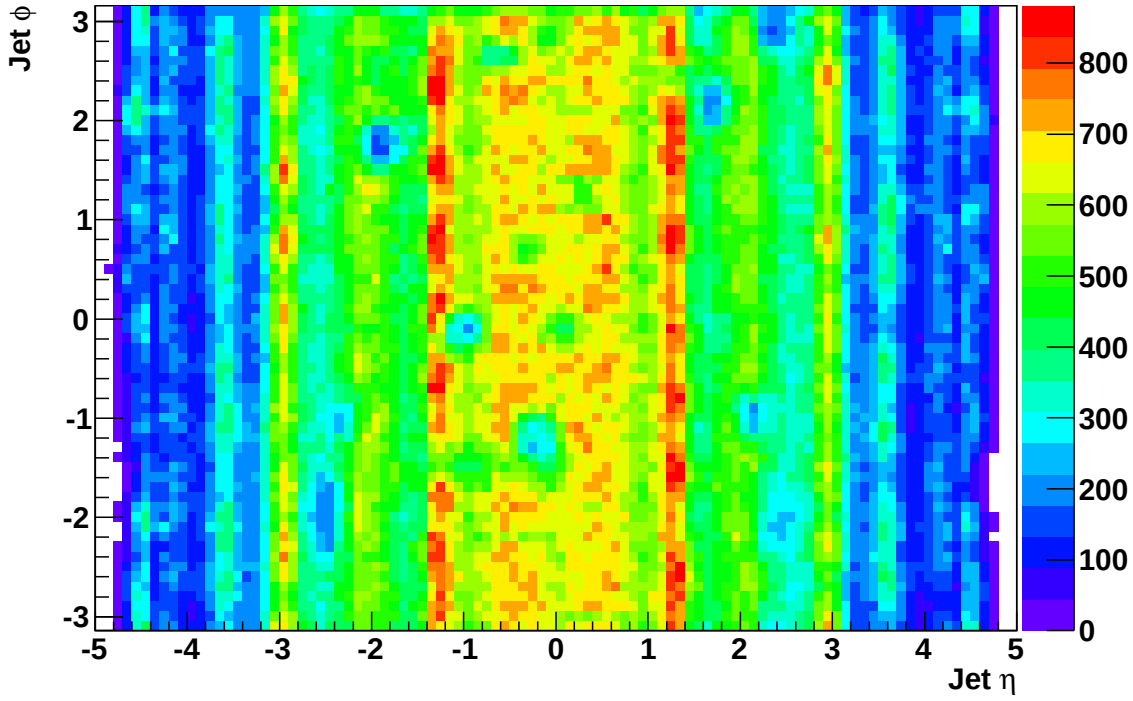

Figure 4.1: Number of jets in the $\eta - \phi$ plane in 0.1×0.1 bins over an entire run.

4.3 Top Good Run Lists

In collaboration with the top quark working group, the author established and produced the GRLs that would be used for all top analyses in ATLAS. Many GRL were produced for this purpose since differences in top analyses lead to different DQ requirements. A first GRL was generated with minimal requirements: 7 TeV stable beams with green DQ flags[3] for ATLAS Global (ATLGL), L1 central trigger (L1CTP) and luminosity determination (LUMI). Then, eleven GRLs with the minimal requirements and some extra virtual flags were generated, see Table 4.1. The numbers in the table are obtained for data contained within periods E4 to I2, periods used in this analysis following the recommendation of the top working group. They correspond to data taken after the 6th of August 2010 up to the first LHC shutdown in December 2010. Periods A to E3 represent less than one pb^{-1}. Note that the following luminosity blocks were removed because the electron or muon trigger used for data selection was pre-scaled: 143-222 (run 162764), 122-284 (run 162882) and 3-7 (run 165817). Not having to deal with trigger pre-scaling greatly simplifies the analysis. Since the luminosity blocks with trigger pre-scale represent a negligible fraction of the total integrated luminosity, 200 nb^{-1} out of 44.51 pb^{-1}, they are not used for analyses.

	muon	electron	jets	metcalo	metmuon	btag	tracking	utrig	etrig	%
all channels	✓	✓	✓	✓	✓	✓	✓	✓	✓	82.3
all channels no b-tag	✓	✓	✓	✓	✓			✓	✓	82.3
trig echannel	✓	✓	✓	✓	✓				✓	82.3
trig muchannel	✓	✓	✓	✓	✓			✓		82.3
noveto echannel		✓	✓	✓					✓	85.0
noveto muchannel	✓		✓	✓	✓			✓		82.3
track echannel		✓	✓	✓			✓		✓	85.0
track muchannel	✓		✓	✓			✓	✓		82.3
met			✓	✓	✓					84.6
met nomuon			✓	✓						88.4
jets			✓							88.4
%	91.5	85.4	88.8	88.4	94.7	100.0	95.4	96.5	96.0	

Table 4.1: Virtual flags used in each of the 11 top GRLs. The percentage of the luminosity remaining for each top GRL is shown in the last column, while the percentage of the luminosity remaining after using each of the virtual flags individually is shown in the last row. The luminosity remaining is divided by the luminosity obtained when using only top minimal selection (44.51 pb^{-1}).

The *muon*, *electron*, *jets*, *metcalo* and *metmuon* and *btag* virtual flags are described in appendix B. Notice that the btag DQ flag was not used for any of the

[3]These flags ensure that there were no major problems with the TDAQ, clock or data header. No lumi-block should be trusted when these DQ flags are not green.

Top GRLs since it was not set for the earlier periods. This is why it is assigned 100%. The tracking virtual flag requires that all the Inner Detector (IDGL, IDVX, PIXB, PIXEA, PIXEC, SCTB, SCTEA, SCTEC, TRTB, TRTEA, TRTEC) and its alignment (IDAL) DQ flags were green. The *utrig* and *etrig* flags stand for muon trigger slice and electron trigger slice and are set by the trigger group.

From Table 4.1, it can be seen that there is a very small difference in the remaining integrated luminosity between the 11 top GRLs: 88.4% (of the top minimal requirement integrated luminosity) when using the jets GRL to 82.3% when using the most restrictive of the GRL, the *all channels* GRL. This is because all the GRLs use the jets virtual flags, which indirectly requires the LAr DQ flags. For the period analyzed, the LAr detector is the one that had the lowest efficiency in terms of DQ: 88.4%, as can be seen from Table 4.2. The table shows the integrated luminosity when requiring that only one of the detectors is green in addition to the minimal requirements. In this case, a detector is considered green when all the primary flags of this detector used in the top GRLs are green. When the electron virtual flag is also used for a GRL, the range width narrows down to 2.7% (85.0% for *noveto echannel* and 82.3% for *all channels*). If the muon virtual flag is used for a GRL, there is then no difference (82.3% for *noveto muchannel* and 82.3% for *all channels*). Since all top analyses use either a muon or an electron, and because the gain in integrated luminosity from using channel specific GRLs is very small, it was decided, to ease comparisons, that all top analyses should use the *all channels* GRL.

Detector	Luminosity after cut (pb^{-1})	Percent of top_minimal_7TeV GRL
Toroid	44.51	100
Solenoid	44.51	100
InDet	42.45	95.4
Muon	43.81	98.4
LAr	39.37	88.4
Tile	44.51	100
top_minimal_7TeV	44.51	100

Table 4.2: Integrated luminosity after requiring each detector to be green individually. The minimal selection GRL is used as a reference.

The correlation between the virtual flags and the detector flags was also studied, see Figure 4.2. It can be seen from Figure 4.2 a) that the *electron*, *muon* and *jets* virtual flags are sufficient to filter all the luminosity blocks that should be removed for top analyses. Part of the reason is that only the ID, muon and LAr detectors had

defects over the data period studied. It can be seen in Figure 4.2 b) that there are no clear correlations between the down time of these detectors, except for the ID and muon detectors.

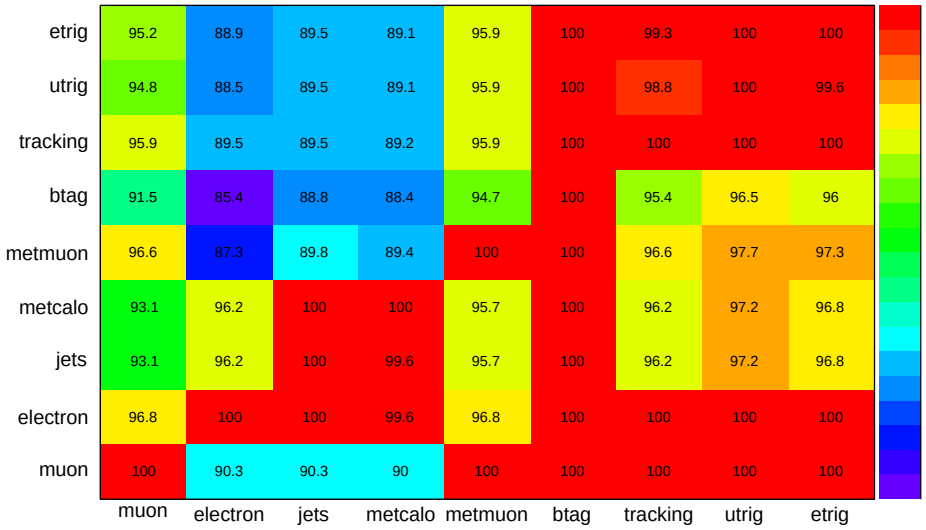

(a)

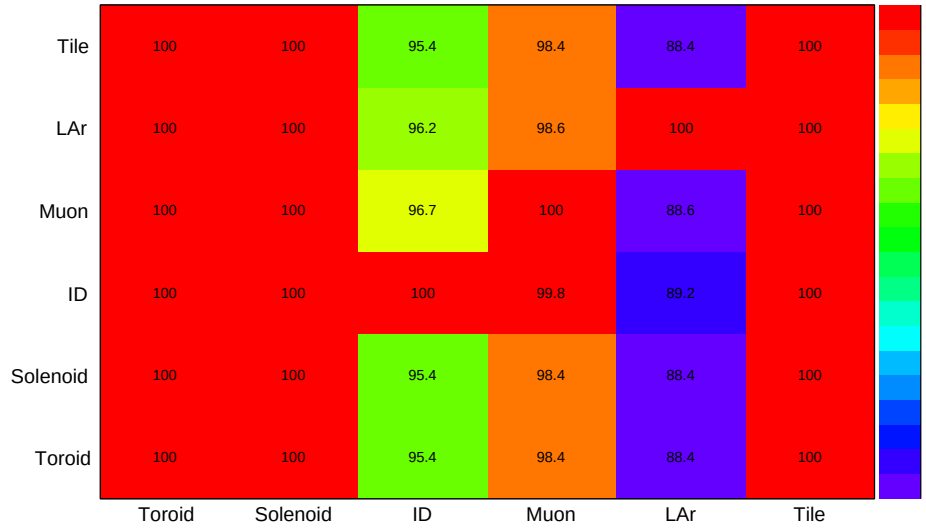

(b)

Figure 4.2: Overlap between (a) the virtual flags (b) the detector flags. The overlaps are defined as follows: integrated luminosity remaining after using the row flag and the column flag divided by the integrated luminosity remaining after using only the row flag. The values are in percent and are also on a colorscale. The closer the number is to 100%, the less impact the column flag has when the row flag is required.

Chapter 5

χ^2 Fitter Approach to Reconstruct $t\bar{t}$ Events

5.1 Statistical Framework

The top-antitop invariant mass spectrum $\frac{1}{\sigma_{t\bar{t}}}\frac{d\sigma_{t\bar{t}}}{dM_{t\bar{t}}}$ can be identified from the probability density function (pdf) of measuring $\mathbf{x}$ given $\mathbf{H_{t\bar{t}}}$, where $\mathbf{x}$ contains all the experimental observables of a $t\bar{t}$ event and $\mathbf{H_{t\bar{t}}}$ is a vector of parameters that specifies entirely the shape and normalization of the pdf. Defining $f(.|\mathbf{Y})$ to be the pdf with a functional form defined by the vector of parameters $\mathbf{Y}$, the function can be written as $f(\mathbf{x}|\mathbf{H_{t\bar{t}}})$. At the moment, this function is rather abstract. For example, $\mathbf{x}$ could be thought as a list of all the channels read by the ATLAS detector in an event; $\mathbf{H_{t\bar{t}}}$ could be the parameters of a well known distribution, for example $\mathbf{H_{t\bar{t}}} = (..., \mu_i, \sigma_i, ...)$ with μ_i, σ_i representing a Gaussian distribution $G(\mu_i, \sigma_i^2)$ for channel i, or it could be a list of points from which $f(\mathbf{x}|\mathbf{H_{t\bar{t}}})$ could be reconstructed using a linear interpolation. The pdf $f(\mathbf{x}|\mathbf{H_{t\bar{t}}})$ can be rewritten as:

$$f(\mathbf{x}|\mathbf{H_{t\bar{t}}}) = f(\mathbf{x}|M_{t\bar{t}})f(M_{t\bar{t}}|\mathbf{H_{t\bar{t}}}) \ , \tag{5.1}$$

where $f(.|y)f(y|.) \equiv \int f(.|y)f(y|.)dy$ is understood. Notice that the function $f(\mathbf{x}|\mathbf{H_{t\bar{t}}})$ has a different functional form than function $f(M_{t\bar{t}}|\mathbf{H_{t\bar{t}}})$ even though there are both specified by $\mathbf{H_{t\bar{t}}}$. In equation (5.1), $f(M_{t\bar{t}}|\mathbf{H_{t\bar{t}}})$ is equivalent to the $M_{t\bar{t}}$ spectrum, $\frac{1}{\sigma_{t\bar{t}}}\frac{d\sigma_{t\bar{t}}}{dM_{t\bar{t}}}$, which is the observable of interest. The goal is therefore to find an estimator for $\mathbf{H_{t\bar{t}}}$ which will be denoted $\hat{\mathbf{H}}_{\mathbf{t\bar{t}}}$.

It is useful to read the right-hand side of equation (5.1) from right to left as it

can be interpreted as what "nature does". The probability of observing $\mathbf{x}$ in our detector, is the probability that "nature generates" a $t\bar{t}$ with $M_{t\bar{t}}$ given the real $\mathbf{H_{t\bar{t}}}$ times the probability that this $t\bar{t}$ will produce $\mathbf{x}$, integrated over all the possible $M_{t\bar{t}}$. The experimentalist task can be read in the reverse order. From many observed $\mathbf{x}$, can $\mathbf{H_{t\bar{t}}}$ be estimated with $\hat{\mathbf{H}}_{\mathbf{t\bar{t}}}$?

The function $f(M_{t\bar{t}}|\mathbf{H_{t\bar{t}}})$ will be approximated using bins in $M_{t\bar{t}}$ of width w, such that

$$\int_{wk}^{w(k+1)} f(M_{t\bar{t}}|\mathbf{H_{t\bar{t}}})dM_{t\bar{t}} = P\left[wk < M_{t\bar{t}} < w(k+1)\right] \equiv P_k \ , \tag{5.2}$$

where P denotes the probability and k is the $\mathbf{H_{t\bar{t}}}$ bin index. A direct parametrization for $\hat{\mathbf{H}}_{\mathbf{t\bar{t}}}$ follows, $\hat{\mathbf{H}}_{\mathbf{t\bar{t}}} = (\hat{P}_0, \ldots, \hat{P}_k, \ldots, \hat{P}_\infty)$, where $\hat{P}_k$ is estimated by calculating the fraction of $t\bar{t}$ events for which their $M_{t\bar{t}}$ is found in bin k. In words, $\hat{P}_k$ estimates the probability that a $M_{t\bar{t}}$ lies between wk and $w(k+1)$. As the number of $t\bar{t}$ events observed $N \to \infty$ and $w \to 0$, $\hat{\mathbf{H}}_{\mathbf{t\bar{t}}} \to \mathbf{H_{t\bar{t}}}$. This estimator $\hat{\mathbf{H}}_{\mathbf{t\bar{t}}}$ is just a normalized histogram showing the distribution of $M_{t\bar{t}}$.

The challenge is then to find an estimator for $M_{t\bar{t}}$ event by event. This estimator will be denoted $\hat{M}_{t\bar{t}}$. The $\mathbf{x}$ can be simplified to be the reconstructed observables of interest: the four highest jets, the lepton and $E_{\mathrm{T}}^{\mathrm{miss}}$ measured 4-momenta in the event, $\mathbf{x} = (p_1^{\mathrm{jet}}, p_2^{\mathrm{jet}}, p_3^{\mathrm{jet}}, p_4^{\mathrm{jet}}, p_{\mathrm{exp}}^{\mathrm{lepton}}, \vec{E}_{\mathrm{T}}^{\mathrm{miss}})$. Then, $f(\mathbf{x}|M_{t\bar{t}})$ can be written as:

$$f(\mathbf{x}|M_{t\bar{t}}) = f(\mathbf{x}|\mathbf{q}) f(\mathbf{q}|p_{\mathrm{had}}^{\mathrm{top}}, p_{\mathrm{lep}}^{\mathrm{top}}) f(p_{\mathrm{had}}^{\mathrm{top}}, p_{\mathrm{lep}}^{\mathrm{top}}|M_{t\bar{t}}) \ , \tag{5.3}$$

where the vector $\mathbf{q}$ represents the 4-momemta of the final $t\bar{t}$ decay products at parton level, $\mathbf{q} = (p_{\mathrm{had1}}^{\mathrm{quark}}, p_{\mathrm{had2}}^{\mathrm{quark}}, p_{\mathrm{had}}^{\mathrm{b}}, p_{\mathrm{lep}}^{\mathrm{b}}, p_{\mathrm{the}}^{\mathrm{lepton}}, p^{\nu})$ and $p_{\mathrm{had}}^{\mathrm{top}}$, $p_{\mathrm{lep}}^{\mathrm{top}}$ are the 4-momenta of the top that decays hadronically and leptonically respectively. The following equations hold by definition:

$$\sqrt{(p_{\mathrm{had}}^{\mathrm{top}} + p_{\mathrm{lep}}^{\mathrm{top}})^2} = M_{t\bar{t}} \ , \tag{5.4}$$

$$p_{\mathrm{had}}^{\mathrm{top}} = p_{\mathrm{had1}}^{\mathrm{quark}} + p_{\mathrm{had2}}^{\mathrm{quark}} + p_{\mathrm{had}}^{\mathrm{b}} \ , \qquad p_{\mathrm{lep}}^{\mathrm{top}} = p_{\mathrm{the}}^{\mathrm{lepton}} + p^{\nu} + p_{\mathrm{lep}}^{\mathrm{b}} \ , \tag{5.5}$$

$$p_{\mathrm{had}}^{\mathrm{W}} = p_{\mathrm{had1}}^{\mathrm{quark}} + p_{\mathrm{had2}}^{\mathrm{quark}} \ , \qquad p_{\mathrm{lep}}^{\mathrm{W}} = p_{\mathrm{the}}^{\mathrm{lepton}} + p^{\nu} \ . \tag{5.6}$$

Equation (5.4) constrains the phase-space of the tops for a given $M_{t\bar{t}}$. Furthermore, from equations (5.5) and (5.6), the 4-momenta in $\mathbf{q}$ are restricted by the

tops' and W bosons' four-momenta[1]. With these constraints, the exact functions for $f(p^{\text{top}}_{\text{had}}, p^{\text{top}}_{\text{lep}}|\text{M}_{\text{t}\bar{\text{t}}})$ and $f(\mathbf{q}|p^{\text{top}}_{\text{had}}, p^{\text{top}}_{\text{lep}})$ are complex and cannot be written analytically. However, an approximation can be obtained by requiring that the invariant masses of the tops and Ws must be near their on-shell values (M_{W} and M_{top}). This will further constrain the 4-momenta in $\mathbf{q}$ by constraining ($p^{\text{top}}_{\text{had}}$,$p^{\text{top}}_{\text{lep}}$,$p^{\text{W}}_{\text{had}}$,$p^{\text{W}}_{\text{lep}}$):

$$\begin{aligned} f(\mathbf{q}|\text{M}_{\text{t}\bar{\text{t}}}) \approx f(p^{\text{W}}_{\text{had}}|\text{M}_{\text{W}}) f(p^{\text{W}}_{\text{lep}}|\text{M}_{\text{W}}) f(p^{\text{top}}_{\text{had}}|\text{M}_{\text{top}}) f(p^{\text{top}}_{\text{lep}}|\text{M}_{\text{top}}) = \\ G\left(\sqrt{(p^{\text{W}}_{\text{had}})^2}\,\middle|\,\text{M}_{\text{W}}, \Gamma^2_{\text{M}_{\text{W}}}\right) G\left(\sqrt{(p^{\text{W}}_{\text{lep}})^2}\,\middle|\,\text{M}_{\text{W}}, \Gamma^2_{\text{M}_{\text{W}}}\right) \\ G\left(\sqrt{(p^{\text{top}}_{\text{had}})^2}\,\middle|\,\text{M}_{\text{top}}, \Gamma^2_{\text{M}_{\text{top}}}\right) G\left(\sqrt{(p^{\text{top}}_{\text{lep}})^2}\,\middle|\,\text{M}_{\text{top}}, \Gamma^2_{\text{M}_{\text{top}}}\right) \quad , \end{aligned} \tag{5.7}$$

where $G\,(z\,|\,\mu, \sigma^2)$ stands for the probability density of z given that variable z follows a Gaussian distribution with mean μ and variance σ^2. Gaussian distributions with standard deviation equal to the natural mass widths of the particles ($\Gamma_{\text{M}_{\text{top}}}$ and $\Gamma_{\text{M}_{\text{W}}}$) were used to describe the pdf of the invariant masses instead of Breit-Wigner distributions, as this will provide a useful simplification without adverse effect on the top analysis. It should be noted that equations (5.4) to (5.6) enter equation (5.7) implicitly.

Similarly, $f(\mathbf{x}|\mathbf{q})$ can be quite complex. Assuming a correct pairing of the quarks with their respective jet, ($p^{\text{quark}}_{\text{a=1}} \to p^{\text{jet}}_{\text{a=1}}, \ldots, p^{\text{quark}}_{\text{a=4}} \to p^{\text{jet}}_{\text{a=4}}$), an approximation is that $p^{\text{quark}}_{\text{a}}$ equals $p^{\text{jet}}_{\text{a}}[\text{true}]$, where $p^{\text{jet}}_{\text{a}}[\text{true}]$ denotes a perfectly measured $p^{\text{jet}}_{\text{a}}$. That is, $f(p^{\text{jet}}_{\text{a}}|p^{\text{quark}}_{\text{a}}) \simeq f(p^{\text{jet}}_{\text{a}}|p^{\text{jet}}_{\text{a}}[\text{true}])$, where $f(p^{\text{jet}}_{\text{a}}|p^{\text{jet}}_{\text{a}}[\text{true}])$ can be interpreted as the experimental resolution of $p^{\text{jet}}_{\text{a}}[\text{true}]$. It will be assumed that there is no uncertainty in the direction of $p^{\text{jet}}_{\text{a}}$ and experimental uncertainty scales the whole 4 vector by a factor, say α_{a}. It will constrain $p^{\text{quark}}_{\text{a}} \simeq p^{\text{jet}}_{\text{a}}[\text{true}] \simeq \alpha_{\text{a}} p^{\text{jet}}_{\text{a}}$. With $\sigma_{\text{jet}}(E)$ denoting the energy resolution of a jet with energy E, the following approximation is taken,

$$f(p^{\text{jet}}_{\text{a}}|p^{\text{quark}}_{\text{a}}) \simeq f(\alpha_{\text{a}}|p^{\text{jet}}_{\text{a}}) \simeq G\left(\alpha_{\text{a}}\,\middle|\,1, \left[\frac{\sigma_{\text{jet}}(\alpha_{\text{a}} E_{\text{a}})}{E_{\text{a}}}\right]^2\right) \quad . \tag{5.8}$$

Compared to jets, the electrons and muons can be measured with great precision in ATLAS. Therefore, the lepton will be taken to be measured perfectly,

[1] The W bosons are an implicit intermediate step between $p^{\text{top}}_{\text{had}}$, $p^{\text{top}}_{\text{lep}}$ and $\mathbf{q}$.

$$p^{\text{lepton}}_{\text{exp}} = p^{\text{lepton}}_{\text{the}} \quad . \tag{5.9}$$

Lastly, since the main source of $E^{\text{miss}}_{\text{T}}$ is the undetected neutrino (ν), it is assumed that $p^{\nu} = (\sqrt{(\lambda E^{\text{miss}}_{\text{x}})^2 + (\lambda E^{\text{miss}}_{\text{y}})^2 + (p_{\nu z})^2}, \lambda E^{\text{miss}}_{\text{x}}, \lambda E^{\text{miss}}_{\text{y}}, p_{\nu z})$, where $\vec{E}^{\text{miss}}_{\text{T}} \equiv (E^{\text{miss}}_{\text{x}}, E^{\text{miss}}_{\text{y}})$, $p_{\nu z}$ is the unknown longitudinal momentum of the neutrino and λ accounts for the energy resolution of $E^{\text{miss}}_{\text{T}}$ in a similar manner that α_{a} does for the jets:

$$f(\vec{E}^{\text{miss}}_{\text{T}}|p^{\nu}) \simeq f(\lambda|\vec{E}^{\text{miss}}_{\text{T}}) \simeq G\left(\lambda \,\middle|\, 1, \left[\frac{\sigma_{E^{\text{miss}}_{\text{T}}}(\lambda E^{\text{miss}}_{\text{T}})}{E^{\text{miss}}_{\text{T}}}\right]^2\right) \quad . \tag{5.10}$$

Equation (5.12) is then obtained by claiming that the different objects in $\mathbf{x}$ have independent pdfs, such that

$$f(\mathbf{x}|\mathbf{q}) = \prod_{\text{a}=1}^{4} f(p^{\text{jet}}_{\text{a}}|p^{\text{quark}}_{\text{a}}) f(p^{\text{lepton}}_{\text{exp}}|p^{\text{lepton}}_{\text{the}}) f(\vec{E}^{\text{miss}}_{\text{T}}|p^{\nu}) \tag{5.11}$$

and by combining equations (5.7), (5.8), (5.9) and (5.10):

$$\begin{aligned} f(\mathbf{x}|\mathrm{M}_{\mathrm{t\bar{t}}}) \simeq & \prod_{\text{a}=1}^{4} G\left(\alpha_{\text{a}} \,\middle|\, 1, \left[\frac{\sigma_{\text{jet}}(\alpha_{\text{a}} E_{\text{a}})}{E_{\text{a}}}\right]^2\right) G\left(\lambda \,\middle|\, 1, \left[\frac{\sigma_{E^{\text{miss}}_{\text{T}}}(\lambda E^{\text{miss}}_{\text{T}})}{E^{\text{miss}}_{\text{T}}}\right]^2\right) \\ & \prod_{\text{type=had,lep}} \left[G\left(\sqrt{(p^{\text{W}}_{\text{type}})^2} \,\middle|\, \mathrm{M}_{\text{W}}, \Gamma^2_{\mathrm{M}_{\text{W}}}\right) G\left(\sqrt{(p^{\text{top}}_{\text{type}})^2} \,\middle|\, \mathrm{M}_{\text{top}}, \Gamma^2_{\mathrm{M}_{\text{top}}}\right)\right] \quad . \end{aligned} \tag{5.12}$$

Also, combining all the previously stated constraints:

$$\begin{aligned} \mathrm{M}_{\mathrm{t\bar{t}}} &= \sqrt{\left[p^{\text{quark}}_{\text{had1}} + p^{\text{quark}}_{\text{had2}} + p^{\text{b}}_{\text{had}} + p^{\text{b}}_{\text{lep}} + p^{\text{lepton}}_{\text{the}} + p^{\nu}\right]^2} \\ &= \sqrt{\left[\sum_{\text{a}=1}^{4} \alpha_{\text{a}} p^{\text{jet}}_{\text{a}} + p^{\text{lepton}}_{\text{exp}} + (\sqrt{(\lambda E^{\text{miss}}_{\text{T}})^2 + p^2_{\nu z}}, \lambda E^{\text{miss}}_{\text{x}}, \lambda E^{\text{miss}}_{\text{y}}, p_{\nu z})\right]^2} \quad . \end{aligned} \tag{5.13}$$

The pdf for the event, $f(\mathbf{x}|\mathrm{M}_{\mathrm{t\bar{t}}})$, is used to form a pseudo-likelihood,

$$L(\mathrm{M}_{\mathrm{t\bar{t}}}) = f(\mathbf{x}|\mathrm{M}_{\mathrm{t\bar{t}}}) \quad . \tag{5.14}$$

This contrasts with the traditional likelihood where the product of the same pdf

function evaluated at the different $\mathbf{x}$ is used. In this case, only one event is considered in the likelihood. The set of six parameters $(\alpha_1, \alpha_2, \alpha_3, \alpha_4, \lambda, p_{\nu z})$ that maximizes the pseudo-likelihood $L(\mathrm{M_{t\bar{t}}})$ is used to obtain $\hat{\mathrm{M}}_{\mathrm{t\bar{t}}}$ using (5.13).

5.2 χ^2 Fitter Implementation

Two packages were created to estimate $\mathrm{M_{t\bar{t}}}$ on a event-by-event basis using the procedure described in the previous section: TopChi2Fitter (χ^2 fitter) and TopTools. These two packages were developed within the ATLAS Top Event Data Model (EDM) framework which offers a standardized interface to store and present reconstructed $\mathrm{t\bar{t}}$ event [20]. The author developed the two packages and was a main collaborator in the design and development of the Top EDM framework. Both the packages and the framework are now part of the official Athena releases and can therefore be used by any ATLAS user.

In practice, the rescaling parameters $(\alpha_1, \alpha_2, \alpha_3, \alpha_4, \lambda)$ and the parameter for the longitudinal momentum of the neutrino $(p_{\nu z})$ are chosen to be the ones that minimize

$$\chi^2 = -2\ln[f(\mathbf{x}|\mathrm{M_{t\bar{t}}})] \ , \tag{5.15}$$

where $f(\mathbf{x}|\mathrm{M_{t\bar{t}}})$ is from equation 5.12. The minimization is achieved numerically using a computer program called Minuit [21] which is integrated within ROOT [22]. Both are standard packages used in high energy physics.

The TopChi2Fitter was implemented keeping in mind that users could use it to perform various analyses which have different objectives. For this reason, it was designed to be highly configurable. In particular, it is possible to add and remove terms in equation (5.12). For example, a user that wishes to use the TopChi2Fitter to measure the top quark mass could remove the terms that constrain the masses of the leptonically and hadronically decaying tops to their known values. In this situation, the top mass constraining terms could be replaced by a term that constraints both leptonic and hadronic top masses to be the same,

$$G\left(\sqrt{(p_{\mathrm{lep}}^{\mathrm{top}})^2} - \sqrt{(p_{\mathrm{had}}^{\mathrm{top}})^2}\,\middle|\, 0, \Delta^2\right) \ , \tag{5.16}$$

where Δ should be the error on the quantity $\sqrt{(p_{\mathrm{lep}}^{\mathrm{top}})^2} - \sqrt{(p_{\mathrm{had}}^{\mathrm{top}})^2}$, namely $\sqrt{2}\Gamma_{\mathrm{M_{top}}}$. In practice however, Δ will be an arbitrary fixed parameter of the χ^2 used to control

the "weight" of this constraint in the fit. More details on this will follow at the end of this section.

Even though the goal of the analysis described in this thesis is not to measure the top quark mass, it was chosen to use this substitution for the likelihood. The main motivation was to compare the measured top mass using the χ^2 fitter to the accepted value to provide a way to validate the χ^2 fitting approach. Another change to equation (5.12) used in the analysis is that the term relating to the rescaling of $E_{\mathrm{T}}^{\mathrm{miss}}$ (λ) was fixed to be exactly one. This choice was made because the experimental error on $E_{\mathrm{T}}^{\mathrm{miss}}$ is considerable. If λ is free, this results in too much freedom in the fit, and less stability in the fitting procedure. In this case, it was found that the χ^2 fit often rescales the $E_{\mathrm{T}}^{\mathrm{miss}}$ to zero which is not physical. The final equation used for the χ^2 is:

$$\chi^2 = \sum_{a=1}^{4} \left[\frac{E_a(1-\alpha_{\mathrm{a}})}{\sigma_{\mathrm{jet}}(\alpha_{\mathrm{a}} E_a)} \right]^2 + \sum_{\mathrm{type=had,lep}} \left[\frac{\sqrt{(p^{\mathrm{W}}_{\mathrm{type}})^2} - \mathrm{M_W}}{\Gamma_{\mathrm{M_W}}} \right]^2 + \left[\frac{\sqrt{(p^{\mathrm{top}}_{\mathrm{lep}})^2} - \sqrt{(p^{\mathrm{top}}_{\mathrm{had}})^2}}{\Delta} \right]^2 . \tag{5.17}$$

The quarks-to-jets association, $(p^{\mathrm{quark}}_{\mathrm{a=1}} \rightarrow p^{\mathrm{jet}}_{\mathrm{a=1}}, \ldots, p^{\mathrm{quark}}_{\mathrm{a=4}} \rightarrow p^{\mathrm{jet}}_{\mathrm{a=4}})$, has to be the right one to properly estimate $\sqrt{(p^{\mathrm{W}}_{\mathrm{type}})^2}$, $\sqrt{(p^{\mathrm{top}}_{\mathrm{lep}})^2}$ and $\sqrt{(p^{\mathrm{top}}_{\mathrm{had}})^2}$. Given that a permutation between the two light quarks coming for the hadronic W does not affect $\sqrt{(p^{\mathrm{W}}_{\mathrm{had}})^2}$ and therefore the χ^2, there are 12 associations possible. In order to select one, the 12 combinations are fitted and the one that returns the smallest χ^2 value is considered to be the right one. In some cases, the results of different associations will be discussed; each association will then be referred to as candidate one to twelve corresponding to the association with the smallest χ^2 to the one with the highest χ^2.

The χ^2 of equation (5.17) is such a central part of the analysis that it is worthwhile to discuss it further in more details. First, it should be noted that even though the symbol χ^2 was used, this variable cannot be expected to be a true χ^2 distribution with two degrees of freedom (seven terms and five fitted parameters). The reason is that the seven terms do not follow exactly a Gaussian distribution. The case of the Gaussian approximation for the Breit-Wigner was already mentioned. However, what can cause an even bigger discrepancy are the terms with the α of the jets because the resolution is determined by the random variable α itself. The cause of this is that the energy resolution of $p^{\mathrm{jet}}_{\mathrm{a}}$ is given by the $p^{\mathrm{jet}}_{\mathrm{a}}[\mathrm{true}]$ and not $p^{\mathrm{jet}}_{\mathrm{a}}$ itself. The consequence is

that the variable α is not symmetrically distributed around the central value $\alpha = 1$, and is therefore certainly not distributed according to a Gaussian distribution. In addition, choosing the wrong quarks-to-jets association for a fraction of the events should have a large effect on the χ^2 distribution of equation (5.17). This discussion is important because it emphasizes that the known property of a χ^2 distribution cannot be used for the χ^2 variable defined in equation (5.17).

Another important discussion regarding equation (5.17) is the value of $\Gamma_{\mathrm{M_W}}$ and Δ. A legitimate question is why should the natural mass width of the particles be taken instead of their experimental resolution. The answer comes from equation (5.7). In this equation, the $p^{\mathrm{W}}_{\mathrm{had}}$ of $f(p^{\mathrm{W}}_{\mathrm{had}}|\mathrm{M_W})$ is the true hadronic W four-momentum. There are no experimental considerations in this term. So, where should the experimental resolution on the masses go? The answer is that it is implicit in the resolution of the jets, the first sum term of equation (5.17). The $\sigma_{\mathrm{jet}}(\alpha_{\mathrm{a}}E_a)$ in GeV are significantly bigger than $\Gamma_{\mathrm{M_W}}$ and Δ. The effective result is that the constraints on the $(p^{\mathrm{W}}_{\mathrm{type}})^2$ and $\sqrt{(p^{\mathrm{top}}_{\mathrm{lep}})^2} - \sqrt{(p^{\mathrm{top}}_{\mathrm{had}})^2}$ are extremely strong, almost exact. Nevertheless, it cannot be set as exact since in some events there are no solutions that satisfy $(p^{\mathrm{W}}_{\mathrm{type}})^2 - (\mathrm{M_W})^2 = 0$ and $\sqrt{(p^{\mathrm{top}}_{\mathrm{lep}})^2} - \sqrt{(p^{\mathrm{top}}_{\mathrm{had}})^2} = 0$ at the same time. Finding an exact solution to these equalities is particularly problematic when the $E^{\mathrm{miss}}_{\mathrm{T}}$ is fixed[2]. Therefore, when there is no exact solution, $\Gamma_{\mathrm{M_W}}$ and Δ give a weight on which equality is more important to satisfy with more accuracy. In this sense, when $\Gamma_{\mathrm{M_W}}$ is kept fixed, the parameter Δ becomes a knob to control this relative weight. For this reason, Δ was not taken to be exactly equal to $\sqrt{2}\Gamma_{\mathrm{M_{top}}}$, but was rather left as a tuning parameter; Δ was fixed to 5 GeV to ensure that more emphasis was placed on the $\mathrm{M_W}$ constraints, since the mass of the W is better known and since there are less experimental objects entering its reconstruction. Moreover, both top masses could be above or below the central mass $\mathrm{M_{top}}$, in which case constraining exactly the top masses to be equal will most likely not improve the estimation of the free parameters in the χ^2.

[2]Even when the λ to rescale $E^{\mathrm{miss}}_{\mathrm{T}}$ is left free there is no exact solution for some events.

Chapter 6

Analysis and Results

6.1 Data and MC Selection

This section describes which data runs and MC samples were used to perform the analysis. It also describes the strategy used to select $t\bar{t}$ events from all the events collected. The analysis is performed using release 16 of the ATHENA software.

6.1.1 Data Samples

The data used for this analysis consist of the *all channels* Top GRL applied over most of the 2010 data collected by ATLAS, periods E4-I2. After offline adjustment[1], it corresponds to a total integrated luminosity of 35.3 pb^{-1}. More details can be found in section 4.3.

6.1.2 MC Samples

This analysis was designed to make minimal use of MC simulations. Nevertheless, it was not possible to completely avoid its usage entirely. In particular, the efficiency and $M_{t\bar{t}}$ distribution of an hypothetical resonance decaying to $t\bar{t}$ had to be obtained from MC. Two MC samples were used:

- A SM $t\bar{t}$ sample simulated using the MC@NLO generator [23], and showered using HERWIG [24](hadronization of the partons) and JIMMY [25] (underlying

[1] It is possible the pursue refined analyses to determine the integrated luminosity offline. ATLAS then provides a correction factor to apply to the luminosity recorded online. The factor used was 0.9626. Notice that the luminosities quoted in section 4.3 do not have this correction factor applied.

event). In this sample, at least one top was required to decay semileptonically.

- Z' samples with various invariant masses generated using PYTHIA [26].

These samples were also useful to verify the performances of the χ^2 fitter.

Other MC samples were used to compare data distributions with expectations. This has no effect on the final result. In addition to the SM $t\bar{t}$ sample, the following samples were needed to reconstruct the expected distributions:

- Single top samples were produced using the same generators used for the SM $t\bar{t}$ samples. These samples contain only events for which the W boson decays leptonically. Note that in the distribution histograms, the single top samples will be combined together with the SM $t\bar{t}$ under the name "top".

- W+Jets samples for which the W decays leptonically were generated using ALPGEN [27] in combination with HERWIG and JIMMY. The three possible leptonic decays, electron, muon and tau, were considered with zero to five extra jets. The cross section for each of these samples was obtained from a fit of the data [28].

- Events with multiple QCD jets were not simulated, as too many events would be required. Only a small fraction of the QCD jets events pass the analysis selection, but the cross section for these processes is large enough to have a non-negligible number of events remaining. A data-driven method was used to obtained this sample [28].

All the MC simulated samples were run through a GEANT4-based simulation [29] of the ATLAS detector. Other processes that occur at ATLAS either have a cross section too small to make a contribution or are completely removed by the event selection.

6.1.3 Trigger Selection

The trigger selection required for the data evolved with time since the instantaneous luminosity was continuously increasing at the LHC. When the instantaneous luminosity increases, stricter trigger requirements are needed to avoid prescaling the events (only taking a fraction of them). For the electron and muon channels, the events were required to pass the triggers specified in Table 6.1 for different periods.

Period	Electron Trigger	Muon Trigger
E4-E7	EF_e15_medium	EF_mu10_MSonly
F	EF_e15_medium	EF_mu10_MSonly
G	EF_e15_medium	EF_mu13
H	EF_e15_medium	EF_mu13_tight
I	EF_e15_medium	EF_mu13_tight

Table 6.1: Electron and muon triggers used for the data (see text).

The interpretation of the trigger tag goes as follow. EF stands for event filter level, eX (muX) for an electron (muon) with p_{T} greater than X GeV and the last suffix indicates the quality of the trigger object. Note that the label MSonly means that only information from the muon spectrometer was used for the muon trigger.

In the case of MC simulations, the simulated triggers required were always EF_e15_medium or EF_mu13_tight in the electron and muon channels respectively.

6.1.4 Event Selection

Once the objects are reconstructed[2], event selection requirements must be specified. These requirements, also referred as event selection cuts, increase the purity of $\mathrm{t\bar{t}}$ events in the analysis; a set of cuts must be defined that keeps as many $\mathrm{t\bar{t}}$ events as possible and removes as many background events as possible. Fortunately, $\mathrm{t\bar{t}}$ events with four quarks, one lepton and one neutrino leave a very specific signature in the detector: 4 jets (two of which should originate from a b-quark), one lepton and some $E_{\mathrm{T}}^{\mathrm{miss}}$. The following event selection requirements were used:

1. $E_{\mathrm{T}}^{\mathrm{miss}} > 20$ GeV.
2. Exactly one lepton (electron or muon) with a $p_{\mathrm{T}} > 20$ GeV. The selected lepton needs to match the trigger lepton.
3. At least 4 jets, each with $p_{\mathrm{T}} > 25$ GeV and $|\eta| < 2.5$.
4. At least one of the 4 highest p_{T} jets was required to be b-tagged.

More than 4 jets are allowed to be present in the event since some extra jets can come from initial or final state radiations as well as the underlying event, or pile-up.

[2]In section 3.3 the object reconstruction algorithms were described briefly. More technical details on the object definitions used in this analysis are described in the ATLAS restricted TopCommonObjects2010 Wiki, [30].

	Data	Top	W+Jets	QCD jets	Total Background
	3.10×10^7	4302	9.60×10^5	-	-
$E_{\mathrm{T}}^{\mathrm{miss}}$	8.77×10^6	3868	6.55×10^5	-	-
One lepton	3.17×10^5	1519	2.70×10^5	-	-
Four jets	1111	558	558	-	-
b-tag	390	352	33	46	431

Table 6.2: Number of events remaining after each event selection cut. The first row contains the number of events after applying the top GRL to the data, or the number of MC events corresponding to the integrated luminosity of the data.

Moreover, given that the b-tagging efficiency is 50%, only one jet is required to be b-tagged. Assuming there are two b-jets in the four highest p_{T} jets, this leads to an event efficiency of 75% from the b-tagging cut compared to 25% if two b-tagged jets were required.

Table 6.2 shows the number of events that remains after applying each of these cuts. The number of background events from MC is also shown in this table. These numbers are meant to illustrate the importance of events selection and its effect on the background; they are otherwise not used in the analysis. The QCD jets background is evaluated from the data after all the cuts are applied, therefore it is not possible to obtain the effect of each cut on this background. The cross section of the W+Jets samples is also obtained from data after all cuts are applied. The final number of data events is 390 while the combination of MC and data-driven background samples gives an expectation of 431. The main source of discrepancy between these numbers likely comes from the data-driven estimation of the QCD jets background. It was shown [28] that using different techniques to obtain this estimation lead to different results. Since this background estimation is used only for illustrative purpose and has no impact on the final result, it is normalized to the number of data events, 390.

6.2 Performance of the χ^2 Fitter

This section demonstrates how the χ^2 fitter performs in reconstructing $\mathrm{t\bar{t}}$ events. Of particular importance is its ability to evaluate $\mathrm{M_{t\bar{t}}}$ accurately on an event by event basis. Therefore, the resolution of $\hat{\mathrm{M}}_{\mathrm{t\bar{t}}}$ will be discussed in some details. Other aspects of the event reconstruction will be discussed, such as the efficiency of the signal and other reconstructed quantities such as the masses of the tops and Ws.

The results presented in this section rely mostly on MC simulations, since truth

information is often required. For example, the resolution of $\hat{M}_{t\bar{t}}$ is defined as the standard deviation of $\hat{M}_{t\bar{t}} - M_{t\bar{t}}$[true]. This information cannot be obtained from the data, so MC $t\bar{t}$ events are needed. There are MC samples of $t\bar{t}$ events generated from SM processes, and there are also exotic MC samples of $t\bar{t}$ events, such as Z′ decaying to $t\bar{t}$. One of the goals of this analysis is to remain as model independent as possible; a choice must be made to determine the mass resolution and signal efficiency. Therefore, when possible, results for SM and Z′ $t\bar{t}$ will be shown.

6.2.1 Resolution

The main objective of the χ^2 fitter is to improve the resolution of the estimated $M_{t\bar{t}}$, $\hat{M}_{t\bar{t}}$. This improvement can be assessed by comparing the resolution obtained with the χ^2 fitter to the one obtained when no fitting is used, that is, with a $\hat{M}_{t\bar{t}}$ where $\alpha_{1,\ldots,4} = 1, \lambda = 1$ and $p_{\nu z} = 0$. The term "before rescaling" or "initial" is used to refer to no fitting; "after rescaling" or "rescaled" means the χ^2 fitter was used.

The $\hat{M}_{t\bar{t}}$ resolution is a function of the $M_{t\bar{t}}$[true] itself. Clearly, $t\bar{t}$ events in a SM MC sample have different values of $M_{t\bar{t}}$[true]. In order to study the resolution as a function of $M_{t\bar{t}}$[true], the $t\bar{t}$ events were grouped together in ranges of $M_{t\bar{t}}$[true]. The central value of each $M_{t\bar{t}}$[true] range will be denoted with the symbol M_X. Figure 6.1 (a) shows the distribution of $\hat{M}_{t\bar{t}} - M_{t\bar{t}}$[true] for SM $t\bar{t}$ events with 700 GeV $< M_{t\bar{t}}$[true] $<$ 750 GeV, and Figure 6.1 (b) shows the resolution for events with 1000 GeV $< M_{t\bar{t}}$[true] $<$ 1100 GeV. In the case of Z′ $t\bar{t}$ events, the Z′ samples are themselves defined by the hypothetical mass of the Z′ ($M_{Z'}$) such that all the $t\bar{t}$ events have the same $M_{t\bar{t}}$[true] in a given Z′ sample[3]. Figure 6.2 shows the $M_{t\bar{t}}$ distribution for a Z′ mass of 700 GeV and 1000 GeV, before and after rescaling.

Tables 6.3 and 6.4 show the standard deviation (σ), defined as the square root of the second central moment, of $\hat{M}_{t\bar{t}} - M_{t\bar{t}}$[true] for SM and Z′ $t\bar{t}$ samples before rescaling (second column) and after rescaling (third column). Using the χ^2 fitter decreases the standard deviation by 10 to 15 GeV for most M_X. These tables also show the standard deviation estimated from fitting a Gaussian distribution as is often done in ATLAS analyses. In this case, the difference between the initial and rescaled standard deviations are not as pronounced. However, the $\hat{M}_{t\bar{t}} - M_{t\bar{t}}$[true] distributions after rescaling cannot be described adequately by a Gaussian distribution. This can

[3]This is not exactly true since $M_{t\bar{t}}$[true] follows a narrow Breit-Wigners distribution around $M_{Z'}$.

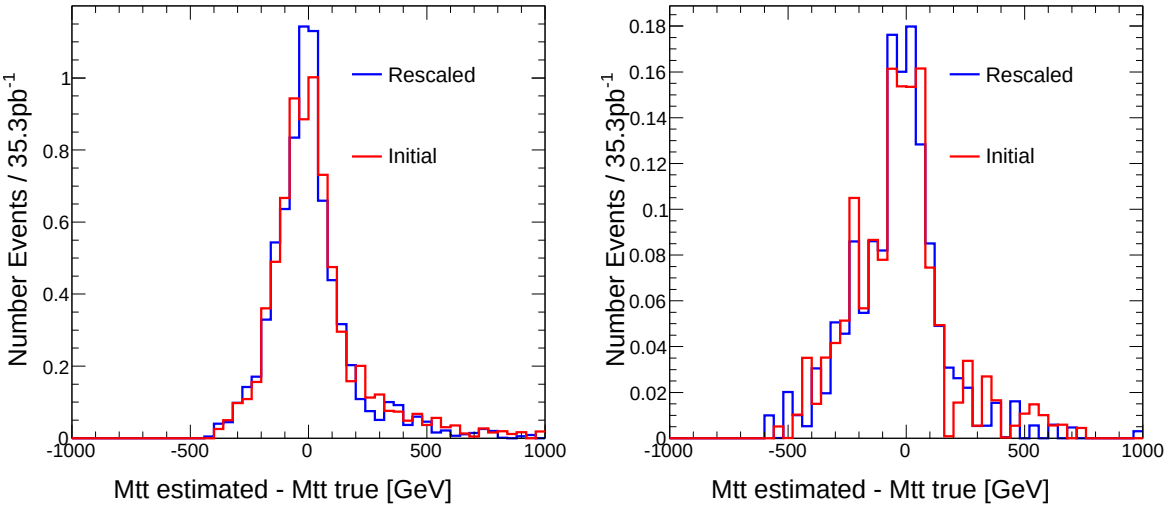

(a) 700 GeV $< M_{t\bar{t}}[\text{true}] <$ 750 GeV (b) 1000 GeV $< M_{t\bar{t}}[\text{true}] <$ 1100 GeV

Figure 6.1: The $\hat{M}_{t\bar{t}} - M_{t\bar{t}}[\text{true}]$ distribution before rescaling and after rescaling for SM $t\bar{t}$ events. Two different $M_{t\bar{t}}[\text{true}]$ ranges are shown.

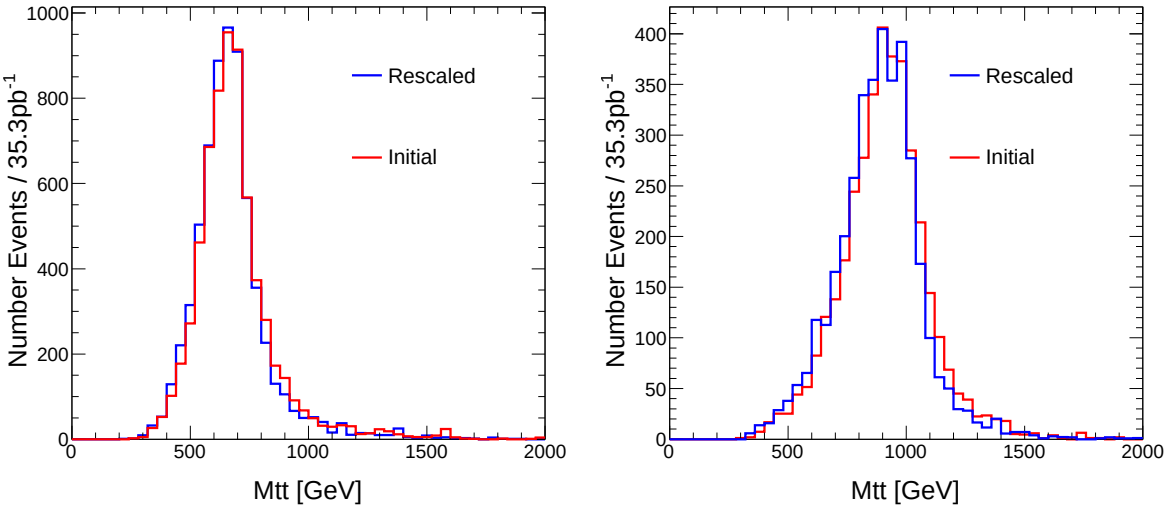

(a) Z′ with a mass of 700 GeV. (b) Z′ with a mass of 1000 GeV

Figure 6.2: The $M_{t\bar{t}}$ distribution of a Z′ with a $M_{Z'}$ of (a) 700 GeV and (b) 1000 GeV.

SM $t\bar{t}$	σ [GeV]		Gaussian σ [GeV]	
M_X [GeV]	Initial	Rescaled	Initial	Rescaled
425	164.5 ± 1.0	153.4 ± 1.0	63.6 ± 0.6	58.7 ± 0.6
475	168.9 ± 1.2	154.2 ± 1.0	71.7 ± 0.8	68.3 ± 0.8
525	169.1 ± 1.4	157.3 ± 1.3	81.9 ± 1.1	78.9 ± 1.1
575	185.3 ± 1.9	172.4 ± 1.7	91.7 ± 1.7	86.6 ± 1.7
625	176.4 ± 2.1	164.1 ± 1.9	98.4 ± 2.2	97.5 ± 2.2
675	190.7 ± 2.7	179.1 ± 2.6	107.1 ± 3.0	105.7 ± 3.0
725	202.5 ± 3.5	184.0 ± 3.2	115.2 ± 3.7	112.1 ± 3.5
775	190.7 ± 3.9	180.5 ± 3.7	121.0 ± 5.2	110.1 ± 4.9
850	226.7 ± 4.8	221.1 ± 4.7	131.4 ± 5.5	126.2 ± 5.6
950	234.0 ± 6.3	203.3 ± 5.5	128.0 ± 8.1	133.4 ± 8.4
1050	201.9 ± 7.5	184.7 ± 6.9	130.3 ± 13.4	137.3 ± 12.9

Table 6.3: Resolution before and after rescaling for different M_X. The standard deviation (σ) is presented as well as the one estimated from fitting a Gaussian distribution.

Z' $t\bar{t}$	σ [GeV]		Gaussian σ [GeV]	
$M_{Z'}$ [GeV]	Initial	Rescaled	Initial	Rescaled
500	150.1 ± 1.7	133.9 ± 1.5	80.9 ± 1.2	77.9 ± 1.1
600	160.5 ± 1.4	147.3 ± 1.3	101.7 ± 1.2	98.19 ± 1.2
700	176.5 ± 1.6	163.6 ± 1.5	115.0 ± 1.6	111.3 ± 1.5
800	180.3 ± 1.6	165.7 ± 1.5	124.6 ± 1.7	119.3 ± 1.7
1000	186.2 ± 2.1	182.9 ± 2.1	141.7 ± 3.4	133.7 ± 3.2

Table 6.4: Resolution before and after rescaling for different $M_{Z'}$. The standard deviation (σ) is presented as well as the one estimated from fitting a Gaussian distribution.

be seen in Figure 6.3 that shows the Gaussian fit[4] after rescaling for two different mass ranges. The histograms are smoothed using the smoothing algorithm 353QH, [31]. This removes some of the statistical fluctuations in the $M_{t\bar{t}}$ resolution spectrum due to limited MC statistic. Moreover, the $\hat{M}_{t\bar{t}} - M_{t\bar{t}}$[true] is shifted by the central mass M_X.

The smoothed distribution of $\hat{M}_{t\bar{t}} - M_{t\bar{t}}[\text{true}] + M_X$ is a good estimate of the $M_{t\bar{t}}$ spectrum of an hypothetical resonance X which has a mass M_X, a negligible natural width and the same production mechanism than the SM $t\bar{t}$. This model is useful to study the behavior of $\hat{M}_{t\bar{t}}$ as a function of M_X. Figure 6.4 (a) shows the most probable value of the resonance X $M_{t\bar{t}}$ distribution as a function of M_X. If $\hat{M}_{t\bar{t}}$ were unbiased estimators of M_X, this relation should be linear with a slope of one. The

[4]The fit includes only points contained within a windows of 560 GeV around the peak.

slope obtained is 0.97 ± 0.01 with a Y-intercept of 4.3 ± 2.2 GeV, which indicates that $\hat{M}_{t\bar{t}}$ systematically undervalues M_X by about 3%. Figure 6.4 shows the relative resolution, σ/M_X, as a function of M_X. As expected, the relative resolution decreases as a function of M_X. The resonances studied are in the range 700-1000 GeV, where the relative resolution varies between 18% and 27%.

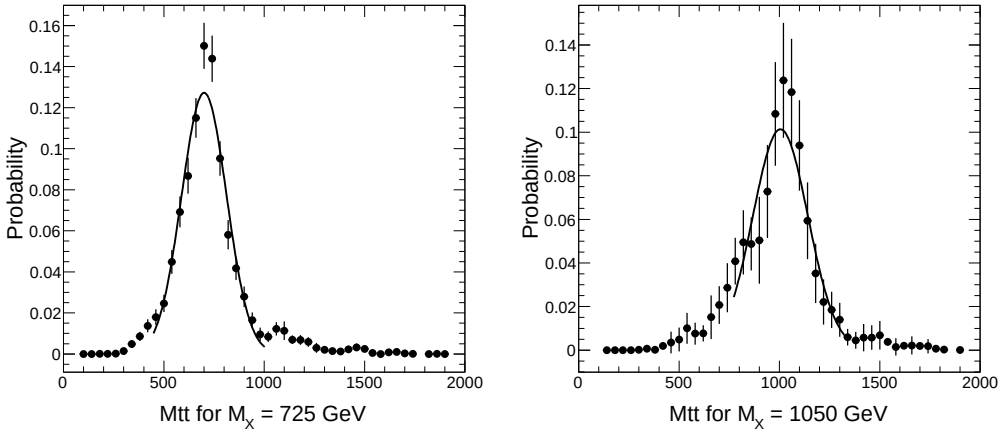

(a) 700 GeV $< M_{t\bar{t}}$[true] $<$ 750 GeV. (b) 1000 GeV $< M_{t\bar{t}}$[true] $<$ 1100 GeV.

Figure 6.3: Gaussian fits of $(\hat{M}_{t\bar{t}} - M_{t\bar{t}}[\text{true}] + M_X)$ distributions after rescaling.

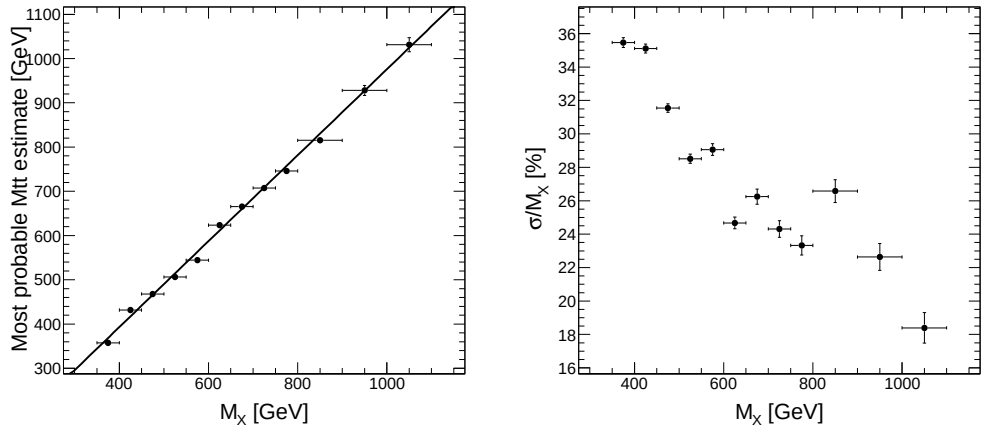

(a) Most probable $\hat{M}_{t\bar{t}}$ vs M_X (b) $\hat{M}_{t\bar{t}}$ standard deviation vs M_X

Figure 6.4: The most probable value (a) and standard deviation (b) of $(\hat{M}_{t\bar{t}} - M_{t\bar{t}}[\text{true}] + M_X)$ as a function of M_X.

6.2.2 Truth Matching

Truth matching is used to assess the accuracy of the $t\bar{t}$ reconstruction. It consists of taking the true parton level information for the MC, namely $\mathbf{q} = (p^{\text{quark}}_{\text{had1}}, p^{\text{quark}}_{\text{had2}}, p^{\text{b}}_{\text{had}}, p^{\text{b}}_{\text{lep}}, p^{\text{lepton}}_{\text{the}}, p^{\nu})$, and verifying if it matches the observables, $\mathbf{x} = (p^{\text{jet}}_{1}, p^{\text{jet}}_{2}, p^{\text{jet}}_{3}, p^{\text{jet}}_{4}, p^{\text{lepton}}_{\text{exp}}, \vec{E}^{\text{miss}}_{\text{T}})$. Since, neither the lepton nor $E^{\text{miss}}_{\text{T}}$ are rescaled, the focus is on truth matching for the four jets.

Before studying the effect of the combinatoric background from the quarks-to-jets association, it is important to identify how often it is actually possible to have a perfect quarks-to-jets association. For example, it is likely that two close by quarks will be reconstructed as one jet; this is more important when the tops have a large transverse momentum. There can also be a significant distance between the direction of a quark and the direction of the reconstructed jet. It this case, the quark and jet will not be identified as matched. The event selection also has an effect on truth matching. In particular, the jets used for the $t\bar{t}$ reconstruction are the four highest p_{T} jets within $|\eta| < 2.5$. Unfortunately, the quarks produced by the two tops do not always fall in this range. Although jets from top decays are expected to have large p_{T}, it is also possible for some jets produced in the underlying event to have a significant p_{T}. Due to this one or more jets that do not come from the $t\bar{t}$ production may enter the set of the four highest p_{T} jets.

To evaluate these effects, the fraction of time that each of the four highest p_{T} jets is matched with only one quark is shown in Figure 6.5 (a): for each jet, the number of $t\bar{t}$ quarks within a distance of $\Delta\text{R} = 0.3$ was counted, and the number of jets matched is the number of jets for which the count was exactly one. Notice that two jets can match the same quark and both have a count of exactly one. Similarly, the fraction of time that each quarks from the $t\bar{t}$ event is matched with only one of the four highest p_{T} jet is shown in Figure 6.5 (b). Since both distributions are essentially the same, it can be concluded that the fraction of time that two or more quarks merge into a single jet is negligible. This results would be different if Z' samples with high $\text{M}_{\text{Z}'}$ were used to study the truth matching. Those are known to have tops with high p_{T} leading to multiple quarks merging into a single jet [18, 32]. The SM $t\bar{t}$ sample was used to study the truth matching when the $\text{M}_{t\bar{t}}$ are relatively low. This is appropriate since this is the mass region covered in this analysis. Lastly, the fraction of time that each quark from a $t\bar{t}$ event is matched to only one of any of the jets in the event is shown in Figure 6.5 (c). It can be observed that a perfect quarks-to-jets

matching is possible about only a third of the time, when only the four highest p_{T} jets are considered. This probability goes up considerably, to 70%, when all the jets are considered. The number of possible quarks-to-jets associations grows rapidly with the number of jets considered. For five, six and seven jets considered in the event, the number of combinations is 60, 180 and 420 respectively. The energy resolution of the jets is not sufficient to allow the χ^2 fit to select the right association out of so many possibilities.

The χ^2 fitter has no control over whether or not the correct quarks-to-jets association exists for a given event. However, if it does exist, it is interesting to know how often it picks the right one. As a quick reminder, the χ^2 fitter keeps the quarks-to-jets association that returns the smallest χ^2 out of all possible associations. Requiring that the b-tagged jet is associated with one of the b-quark reduces the number of possible associations from 12 to six. Furthermore, when there are two b-tagged jets, the number of possible associations goes down to only two. Figure 6.6 shows with what probability each of the association candidates, ordered by increasing χ^2, was actually the right association when a correct association exists for the event. It is reassuring to see that the χ^2 fitter is right more than 60% of the time.

The fraction of events for which it is possible to match all the quarks coming from the $\mathrm{t\bar{t}}$ process to the four highest p_{T} jets is about 35%. However, when a match is possible, the χ^2 fitter finds the right quarks-to-jets association more than 60% of the time.

6.2.3 Efficiency

The efficiency of reconstructing $\mathrm{t\bar{t}}$ events also depends on $\mathrm{M_{t\bar{t}}}$[true]. This fact is very important when trying to establish an upper limit on a cross section since the efficiency enters linearly in the determination of the cross section, see equation (3.2). Figure 6.7 shows the efficiency of keeping a $\mathrm{t\bar{t}}$ event after all the selection cuts as a function of $\mathrm{M_{t\bar{t}}}$[true] of the event. It can be seen that the efficiency variation as a function of $\mathrm{M_{t\bar{t}}}$[true] is non-negligible. Fortunately however, for the mass range considered in the final analysis, 700 GeV to 1000 GeV, the efficiency varies only between 18 and 22% for the SM and 24% to 26% for the $\mathrm{Z'}$ model.

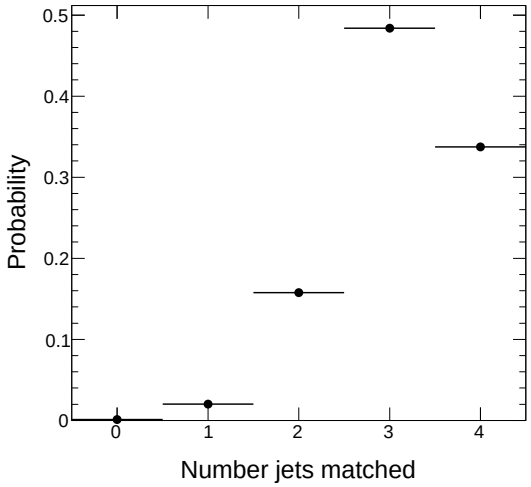

(a) Number of four highest p_{T} jets matching only one quark.

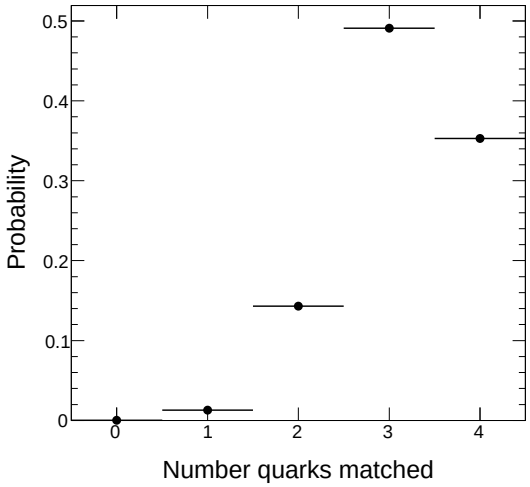

(b) Number of quarks from $\mathrm{t\bar{t}}$ matching only one of the four highest p_{T} jets.

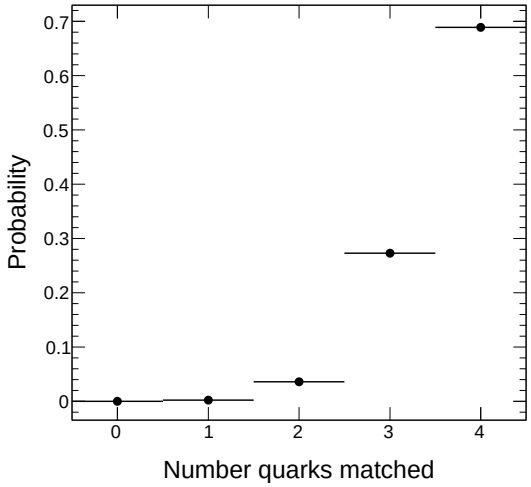

(c) Number of quarks from $\mathrm{t\bar{t}}$ matching only one of the jets in the event.

Figure 6.5: Quark-jet matching probability. The error bars are too small to be seen.

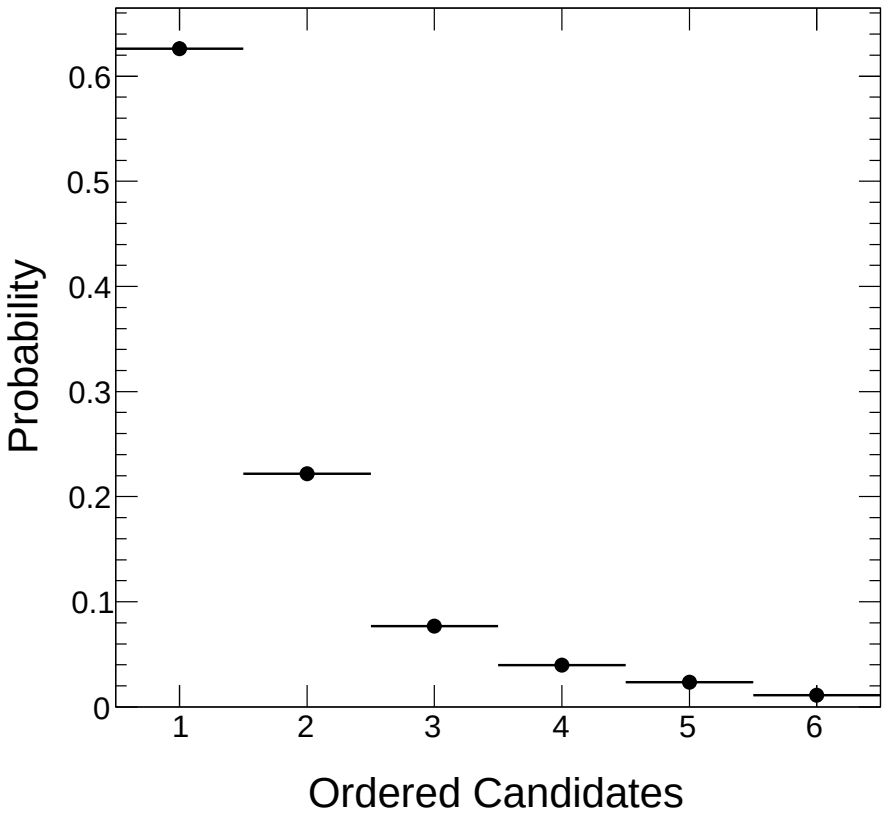

Figure 6.6: Fraction of time that each quarks-to-jets association candidate, ordered by increasing χ^2, is actually the right association when a correct association exists for the event. The error bars are too small to be seen.

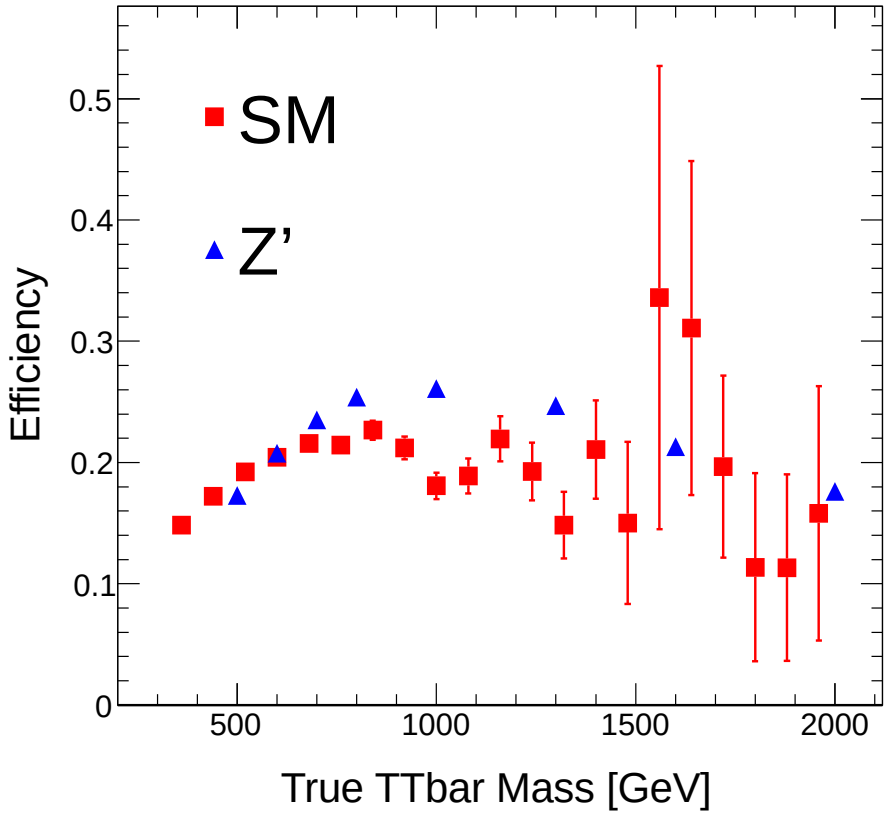

Figure 6.7: The efficiency of selecting a $t\bar{t}$ event in the lepton + jets channel as a function of $M_{t\bar{t}}$[true] of the event for SM and Z′ samples. The errors are evaluated using frequentist Clopper-Pearson interval [33].

6.2.4 Distributions

The performance of the χ^2 fitter can be evaluated through quantities other than $M_{t\bar{t}}$. The distributions presented in this subsection can be extracted from data as well as from MC, and therefore both will be shown in the figures. Data will be represented by a dot with error bars, while the various backgrounds will be represented by stacked histograms. The stack of background histograms is normalized to the same number of events as the data, 390 events.

A first set of control plots is the distributions of the rescaling factors obtained by the χ^2 fitter. Figure 6.8 shows the four-momentum rescaling factor (α) of the jet that was identified as the hadronic b-jet, leptonic b-jet, light jet one and light jet two. The light jets are the two jets coming from the hadronically decaying W; the one and two refer to the highest and second highest p_T jet of the pair. The distributions are centered around one. The second light jet seems to be often rescaled to a lower energy; the distribution of Figure 6.8 (d) has a large tail to the left. This can be understood as follows. The χ^2 fitter tries to satisfy $(M_W)^2 \simeq E_1 E_2[1 - \cos\theta]$, the mass constraint of the hadronically decaying W. Rescaling E_2 does not increase the value of the χ^2 as much as E_1 since $\sigma_{jet}(E)/E$ decreases as a function of the energy E, and $E_1 > E_2$ most of the time. Therefore, the χ^2 fitter will tend to rescale the second light jet more than the first light jet to satisfy the M_W constraint.

In the χ^2 fitter, the W mass is tightly constrained to its known value, so it is no surprise if this quantity is reconstructed almost exactly after rescaling. This is what can be seen in Figure 6.9. Note that since the lepton and E_T^{miss} are not rescaled, the change in the reconstructed mass of the leptonically decaying W after rescaling comes uniquely from the evaluation of $p_{\nu z}$. It is nevertheless interesting to note that even before the rescaling, the distributions' peak is around the mass of the W.

The top mass distributions are interesting to analyze since the known top mass was not used in the χ^2 fitter. A clear peak around the top mass can be observed in all the plots of Figure 6.10. Moreover, after the rescaling is done, this peak is enhanced.

Following satisfactory control plots, the $M_{t\bar{t}}$ spectrum can now be studied, Figure 6.11. This distribution is at the heart of the analysis and the remaining of the thesis focuses entirely on it. The goal is to search for resonances in this spectrum and, if none are found, to determine to which level they can be excluded.

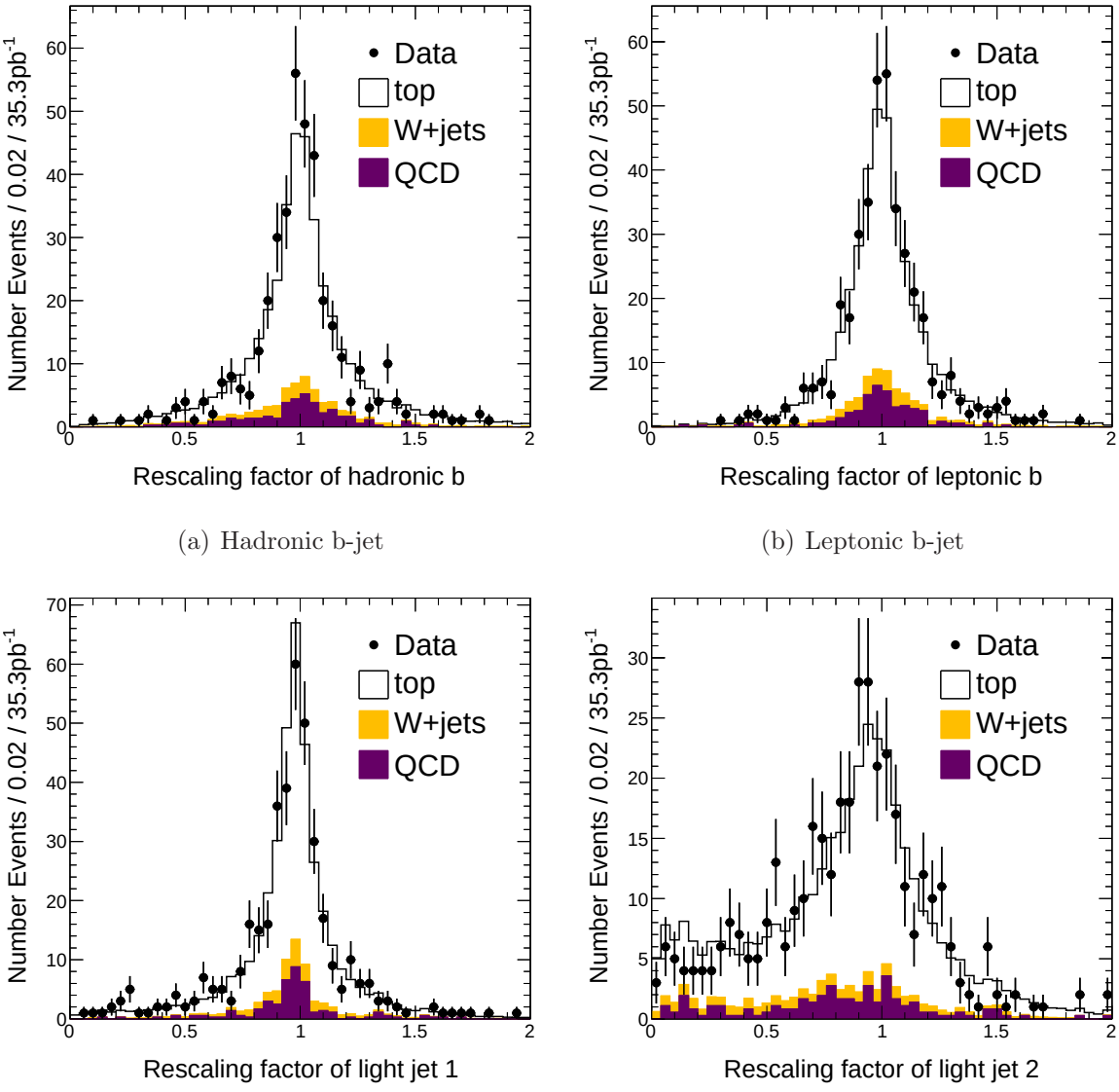

(a) Hadronic b-jet

(b) Leptonic b-jet

(c) Light jet one

(d) Light jet two

Figure 6.8: The distribution of the rescaling factors obtained by the χ^2 fitter for the different jets in the event.

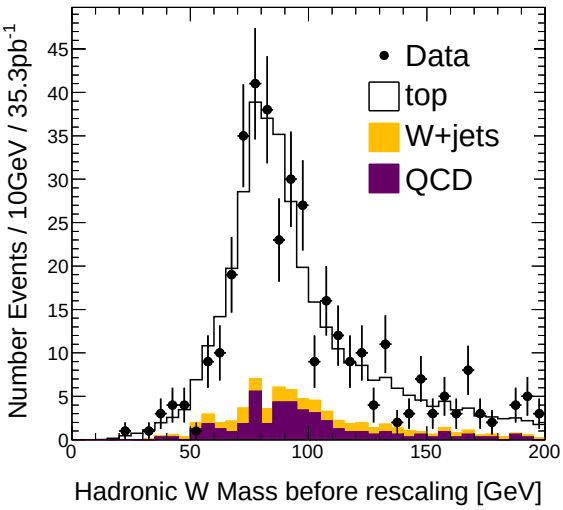

(a) Mass of the hadronically decaying W before rescaling

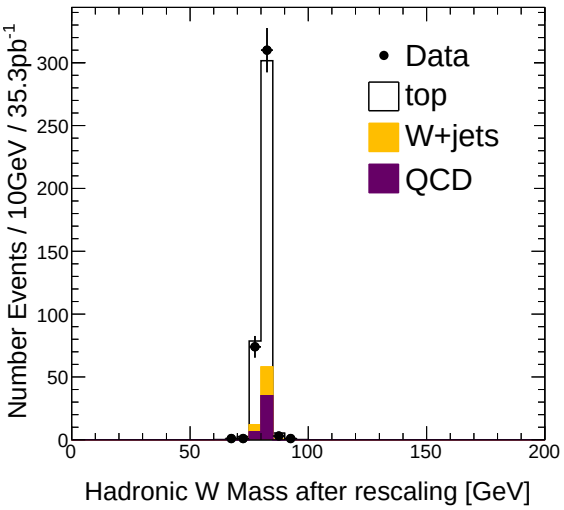

(b) Mass of the hadronically decaying W after rescaling

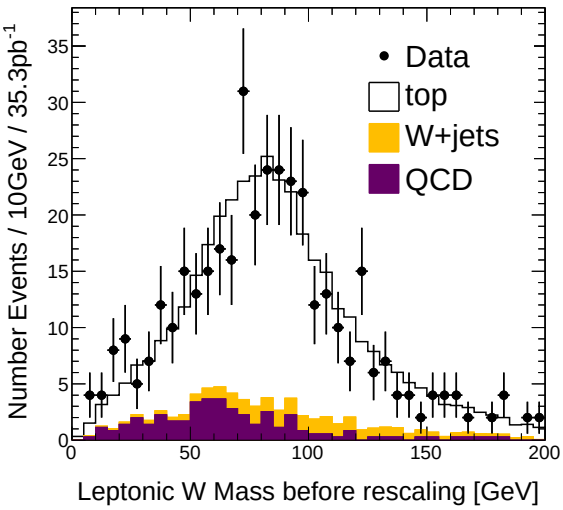

(c) Mass of the leptonically decaying W before rescaling

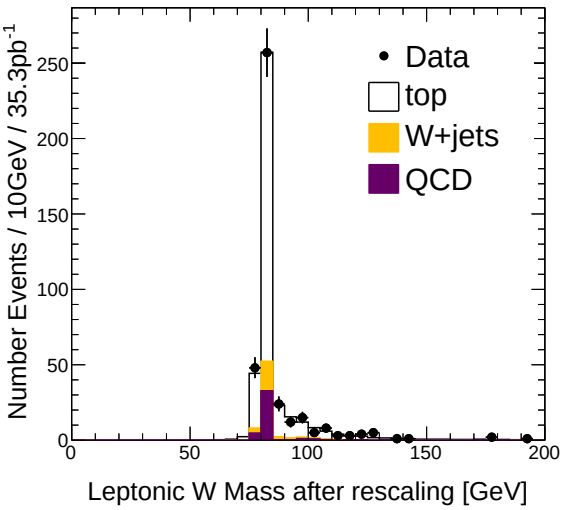

(d) Mass of the leptonically decaying W after rescaling

Figure 6.9: The reconstructed masses of the hadronically and leptonically decaying W, before and after rescaling.

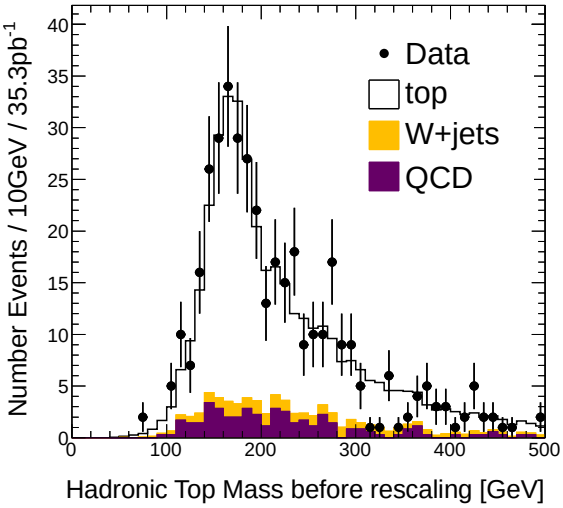

(a) Mass of the hadronically decaying top before rescaling

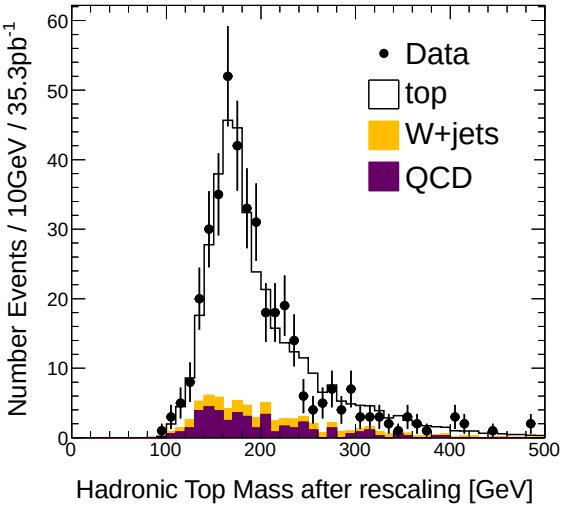

(b) Mass of the hadronically decaying top after rescaling

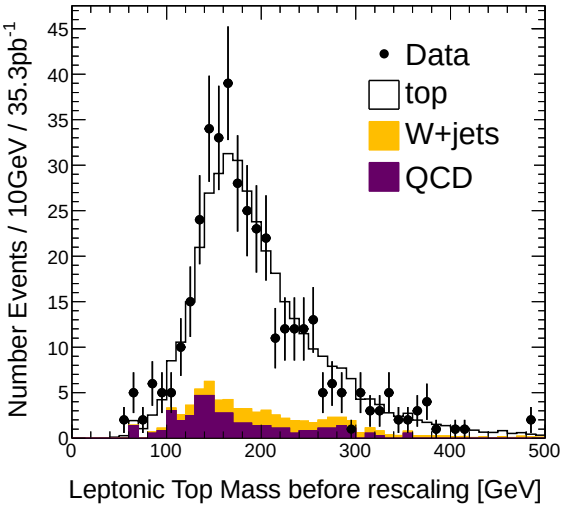

(c) Mass of the leptonically decaying top before rescaling

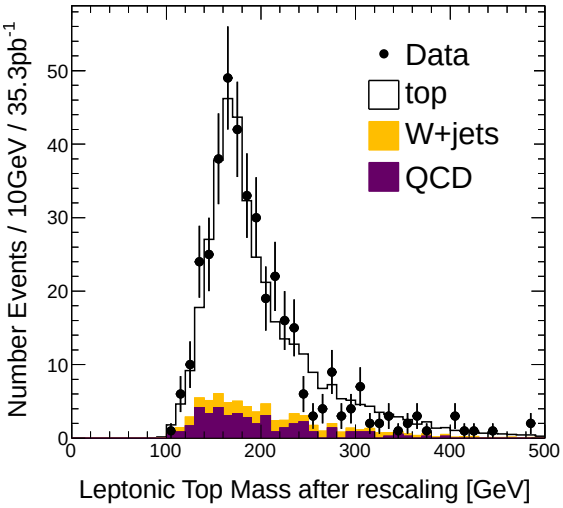

(d) Mass of the leptonically decaying top after rescaling

Figure 6.10: The reconstructed masses of the hadronically and leptonically decaying top, before and after rescaling.

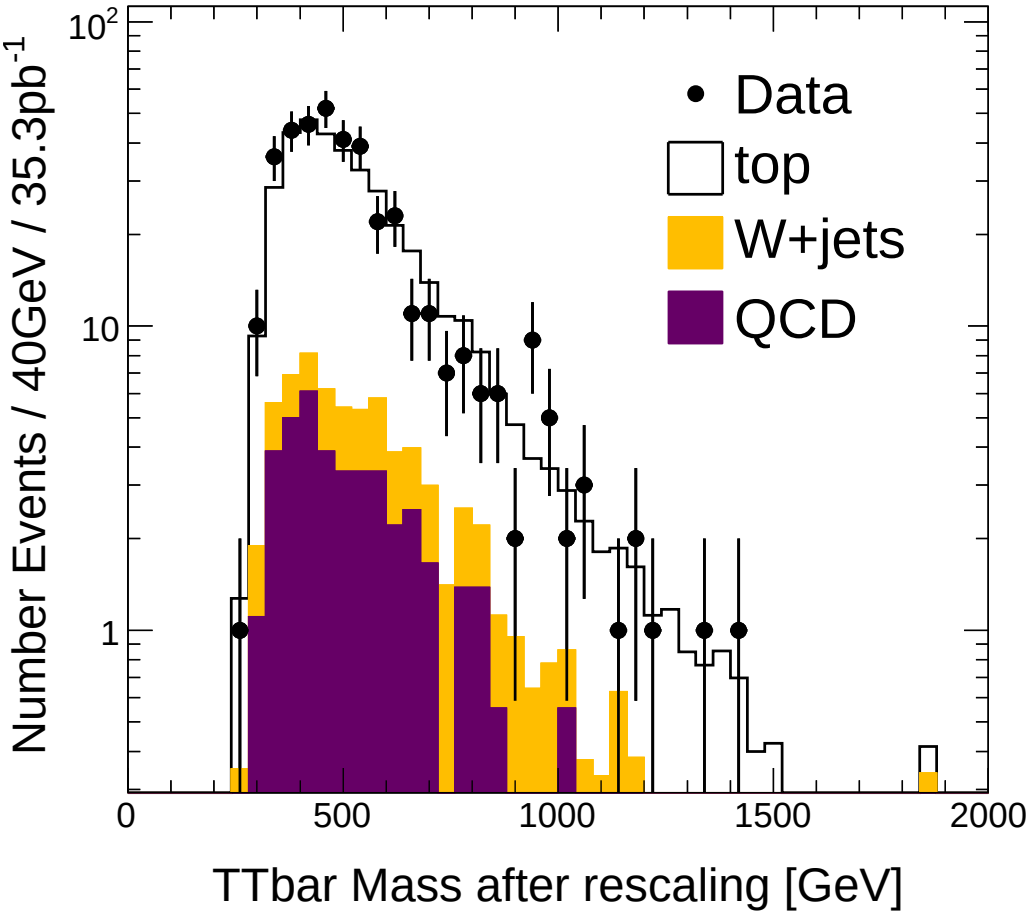

Figure 6.11: The $M_{t\bar{t}}$ spectrum reconstructed using the χ^2 fitter. As for the other figures, the background is normalized to the data.

6.3 Search for Resonances

This section establishes if a resonance coming from an hypothetical particle X or Z′ decaying into $t\bar{t}$ can be identified. That is, is there a signal such as the one in Figure 2.6 in the reconstructed $M_{t\bar{t}}$ spectrum of Figure 6.11? A statistical analysis will be performed to establish the significance of any such resonances. In the absence of statistically significant resonances, a 95% confidence level upper limit on the production cross section of the resonance particle times its branching ratio for decays into a $t\bar{t}$ ($Br[X \to t\bar{t}]$) will be established. This result will be quoted as a function of the mass of the resonance. When referring to the mass of a particle that is assumed to have the same couplings as a SM $t\bar{t}$, the symbol M_X will be used. For MC simulations of Z′, the symbol $M_{Z'}$ will be used. Moreover, the $M_{t\bar{t}}$ spectrum shown on Figure 6.11 is for display only; it will not be used directly to extract the final result since the statistical test will be based on an *unbinned* likelihood ratio method.

6.3.1 Strategy

This analysis is complementary to another study performed within the ATLAS collaboration [28]; each analysis being sensitive to different sources of error. Since this was one of the main consideration in designing the analysis, this subsection highlights the differences between the two analyses.

The analysis presented in [28] does not use the χ^2 fitter, which rescales the energy of the jets. It also makes no attempt to reconstruct the individual top quarks' four-momenta. The four highest p_T jets are assumed to come from the $t\bar{t}$ pair decay, and the neutrino's longitudinal momentum ($p_{\nu z}$) is determined by imposing an exact constraint on the W boson mass. More importantly, the background is evaluated differently. In [28], the background distribution, including shape and overall normalization, is entirely estimated from MC simulations or independent data driven techniques. The background distribution is assumed to be known before reconstructing the $M_{t\bar{t}}$ spectrum from the data. A statistical test is then developed to compare the $M_{t\bar{t}}$ spectrum in data to the expected one. This test uses a Baysian approach and compares the obtained and expected $M_{t\bar{t}}$ histogram bin by bin:

- Pros of analysis [28]:

- The "exact" shape and normalization of the background are assumed to be

known. This reduces the number of unknown parameters in the statistical test and therefore in principle leads to a more stringent upper limit on the cross section.

- Cons of analysis [28]:

- The exact distribution and cross section for each background of the $M_{t\bar{t}}$ spectrum must be estimated. It can be difficult to estimate the systematic error on a MC simulation or data driven background estimation technique.

- Only an excess of events with respect to the expected background normalization can be detected. The test is insensitive to an excess in a $M_{t\bar{t}}$ bin compared to the surrounding bins since it only compares the number of events observed and expected by bin of $M_{t\bar{t}}$. That is, if the overall expected normalization of the background is larger than the data, the analysis would be less sensitive to resonances.

In the analysis presented in this thesis, the shape and normalization of the background distribution are obtained from fitting a parametrized function to the data. A second parametrized function for the signal is fitted simultaneously. The signal is extracted from studying the shape of the reconstructed $M_{t\bar{t}}$ distribution. Furthermore, an unbinned likelihood is used to perform the combined fit. The upper limits are obtained using a frequentist approach:

- Pros of this analysis:

- The dependence on the MC simulation can be kept to a minimum. There is no need to know the cross section of each background entering the $M_{t\bar{t}}$ spectrum.

- The overall background normalization cannot hide resonances.

- There are no systematic errors from the histogram binning since an unbinned likelihood is used.

- Cons of this analysis:

- The number of unknown parameters in the statistical test is increased by having free parameters describing the shape and normalization of the background and signal. This reduces the power of the statistical test to detect or exclude the presence of resonances.

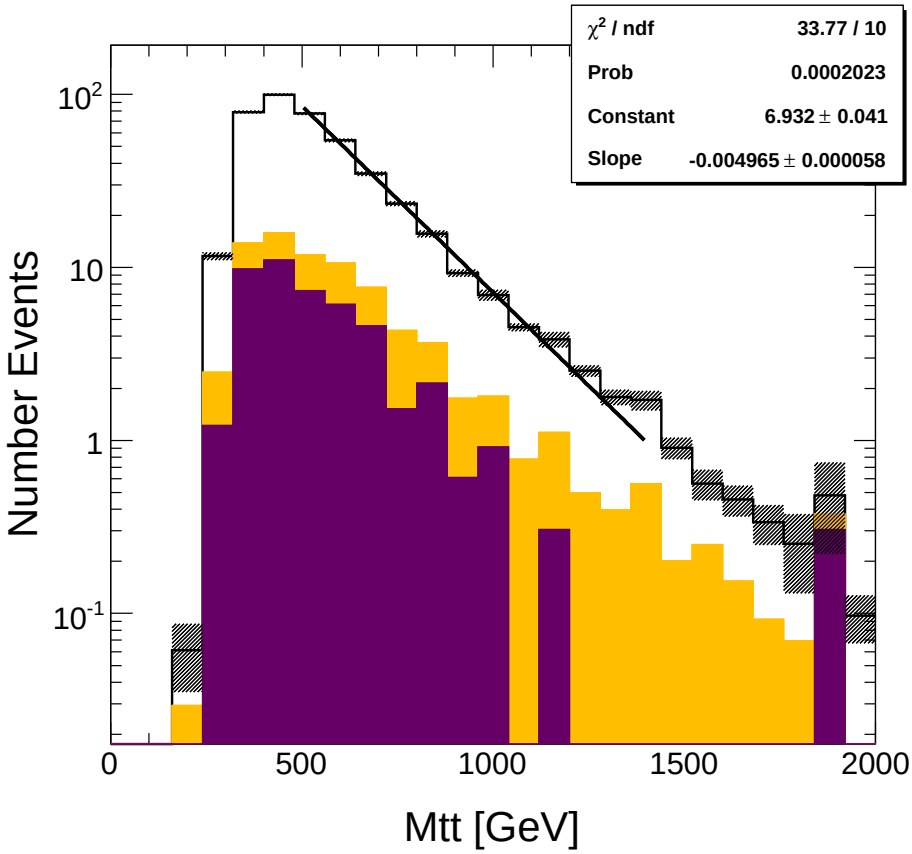

Figure 6.12: Exponential fit of the expected background. The expected background for top (white) and W+Jets (orange) comes from MC simulations while the QCD contribution (purple) was estimated from a data driven method. The dashed area represents the statistical error on the expected background.

6.3.2 Background Shape

The analysis relies critically on finding an adequate parametrized function for the shape of the background. From Figure 6.11, an exponential function seems to be a good candidate. To quantitatively test whether this is an appropriate choice or not, the expected $M_{t\bar{t}}$ background distribution is fitted between 500 and 1400 GeV using an exponential function, Figure 6.12. The χ^2 obtained from the fit is 33.77 for ten degrees of freedom (12 for the bins minus 2 for the exponential parameters). This leads to a p-value of 0.0002, which suggest that the $M_{t\bar{t}}$ background does not exactly follow an exponential function. More parameters would be needed to better describe the shape of the background.

The events from the MC simulations and data driven QCD background estima-

tion add up to more than half a million events in total; the statistical error on the number of expected events in each bin (dashed area) is extremely small. This leads to a high sensitivity to the spectrum shape and hence a small p-value when comparing to a simple exponential shape. A more suitable approach is to consider samples with a number of events comparable to the measured number. Thus, 10000 pseudo-experiments with 390 events drawn from the expected background distribution were generated. For each pseudo-experiment, an exponential is fitted and a p-value obtained. The distribution of the p-values obtained is shown in Figure 6.13. If the expected background $M_{t\bar{t}}$ distribution exactly followed an exponential, the distribution would be uniform; 1% of the pseudo-experiments should be in the first percentile, 1% in the second percentile and so on. There is a small excess of pseudo-experiments with a p-value smaller than 0.04 seen in the first two bins of the distribution. This confirms that the background distribution is not exactly an exponential distribution, but this excess is of the order of $[(300-200)+(250-200)]/10000 = 1.5\%$ and is considered negligible. An exponential function fits the background adequately given the level of sensitivity of the experiment[5].

Using a fitted function based on the expected background does not procure much more advantage than simply using the expected background distribution. However, if it can be shown that the parametrized function still works even though the background expectation was not correct, than it represents a major gain. In particular, if the cross section of the multiple backgrounds composing the $M_{t\bar{t}}$ spectrum were significantly different, could an exponential function still fit the resulting $M_{t\bar{t}}$ distribution? To answer this question, the same procedure described before was used to obtained the distribution of the p-values when the cross section of the QCD and W+Jets backgrounds were renormalized (rescaled) by -50% to 50%. Figure 6.14 shows the median p-value of the 10000 pseudo-experiments for each renormalization. If the background $M_{t\bar{t}}$ distribution were exactly exponential, the median p-value should be 0.5. This is the case, within the statistical fluctuations, independently of the relative cross section of the backgrounds. An exponential function can therefore always be used to describe the $M_{t\bar{t}}$ background.

An exponential function only has two parameters, one to specify the normalization and another one to describe the shape. It is fortunate that the background distribution can be fitted with so few parameters, since fewer free parameters in the statistical test implies a better sensitivity to resonances.

[5]This statement would change if the integrated luminosity was significantly higher.

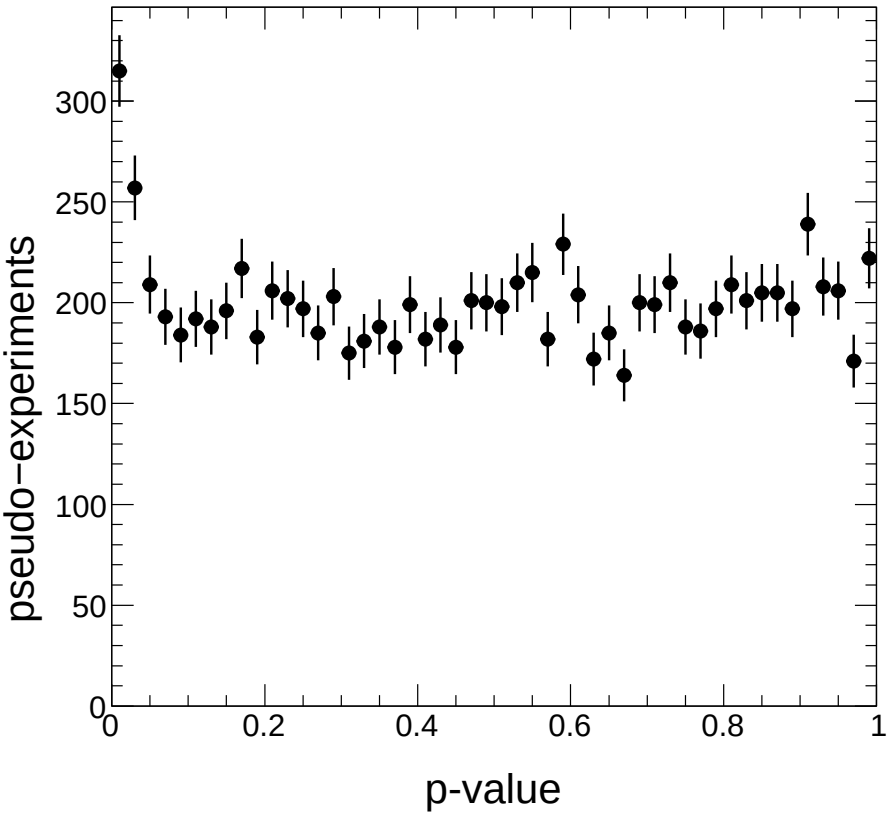

Figure 6.13: The p-values obtained when fitting 10000 pseudo-experiments with an exponential function. Each pseudo-experiment consisted of 390 events drawn from the expected background distribution.

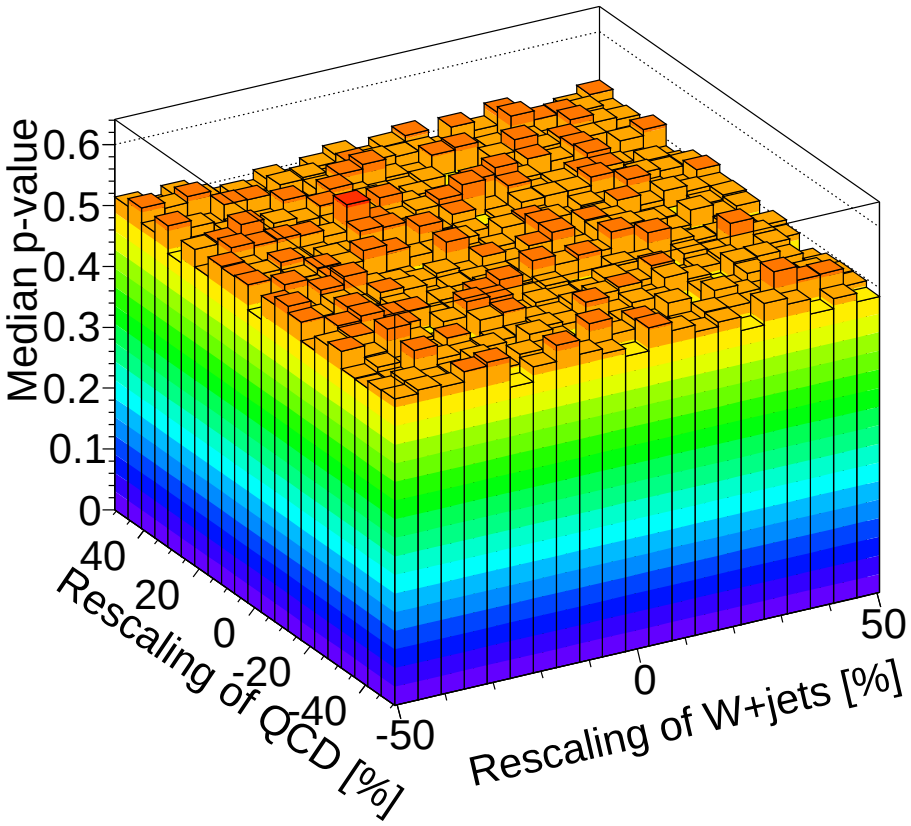

Figure 6.14: The median p-value of 10000 pseudo-experiments for different renormalization (rescaling) of the QCD and W+Jets backgrounds.

6.3.3 Signal Shape

The shape of the $M_{t\bar{t}}$ distribution for a hypothetical resonance for different given masses also needs to be assumed. This shape can be obtained from MC simulations and depends on the assumptions of the model. Two models are considered: a particle X with no natural width and the same $M_{t\bar{t}}$ resolution as for SM $t\bar{t}$, and a Z′ particle. Both were presented in section 6.2.1. It was demonstrated that the $M_{t\bar{t}}$ distribution for these signals does not follow a Gaussian. In fact, no analytical function with a low number of parameters was found to adequately fit these distributions. It was therefore chosen to use the shape predicted from the smoothed MC histogram. Points in between the bins are interpolated linearly. Only one parameter is then needed to fit the overall normalization of the signal.

6.3.4 Testing for Resonances

There are a total of three parameters needed to describe the $M_{t\bar{t}}$ spectrum based on the previous assumptions: the number of background events (n_b), the exponential parameter describing the background (λ) and the number of signal (n_s). The parameters n_b and n_s are the number of events in the range of the fit, 500-1400 GeV. The n_s parameter can be written as

$$n_s = \mathcal{L}\epsilon\sigma \mathrm{Br}[t\bar{t} \to (\mathrm{e\ or\ }\mu)] \ , \tag{6.1}$$

where $\mathcal{L}$ is the total integrated luminosity, ϵ is the efficiency in the lepton + jets channel, σ is the production cross section for the hypothetical particle times its branching fraction into $t\bar{t}$[6] and $\mathrm{Br}[t\bar{t} \to (\mathrm{e\ or\ }\mu)]$ is the branching ratio of $t\bar{t}$ decaying into the lepton + jets channel. The luminosity is measured experimentally, the efficiency is estimated from MC simulations and the $\mathrm{Br}[t\bar{t} \to (\mathrm{e\ or\ }\mu)]$ is known theoretically to be 30%. The physical parameter of interest is σ. To estimate simultaneously n_b, λ and σ the following likelihood is maximized:

$$L(\sigma, n_b, \lambda) = \mathrm{P}(N|n_b + n_s) \prod_j^N \left[\frac{n_b f_b(M^j_{t\bar{t}}|\lambda)}{n_b + n_s} + \frac{n_s f_s(M^j_{t\bar{t}})}{n_b + n_s} \right] \ , \tag{6.2}$$

where $f_b(M^j_{t\bar{t}}|\lambda)$ and $f_s(M^j_{t\bar{t}})$ are the pdf for the background and signal respectively, $n_s \equiv n_s(\sigma)$, and the product is over all the events. As explained before, $f_b(M_{t\bar{t}}|\lambda)$ is

[6] The σ term will be referred simply as the cross section in the text.

the exponential function $Ae^{-\lambda M_{t\bar{t}}}$, where $A^{-1} = e^{-\lambda M_{t\bar{t}}(\min)} - e^{-\lambda M_{t\bar{t}}(\max)}$ is a normalization factor, and $f_s(M_{t\bar{t}})$ is obtained through linear interpolation in the normalized MC $M_{t\bar{t}}$ signal histogram. $P(N|n_b + n_s)$ is the Poisson probability of observing N events given an expectation of $n_b + n_s$ events. N is the number of data events in the range of the fit 500-1400 GeV, 179 events. To investigate the probability of having an hypothetical particle with a cross section (σ), a test statistic ($\tilde{t}_\sigma$) is formed by taking the ratio of this maximized likelihood when the cross section is fixed (σ) and free ($\hat{\sigma}$), [34]

$$\tilde{t}_\sigma = \begin{cases} -2\ln\dfrac{L(\sigma,\hat{\hat{n}}_b,\hat{\hat{\lambda}})}{L(0,\hat{n}_b,\hat{\lambda})} & \text{if } \hat{\sigma} < 0 \\ -2\ln\dfrac{L(\sigma,\hat{\hat{n}}_b,\hat{\hat{\lambda}})}{L(\hat{\sigma},\hat{n}_b,\hat{\lambda})} & \text{if } \hat{\sigma} \geq 0 \end{cases} . \tag{6.3}$$

The conditional statement is required to properly treat the case of an unphysical value of $\hat{\sigma}$, namely $\hat{\sigma} < 0$. The single hat ($\hat{}$) and double hat ($\hat{\hat{}}$) are used to denote the estimation of the parameters when the cross section is free and fixed respectively. Notice that each likelihood in the ratio is maximized individually before taking their ratio.

The p-value is defined as the probability of observing a $M_{t\bar{t}}$ distribution as or more *anomalous* than the one observed given the σ hypothesis. The test statistic $\tilde{t}_\sigma$ is designed such that more anomalous data lead to higher $\tilde{t}_\sigma$. Taking $\hat{\sigma} = \sigma$ in equation (6.3) yields zero; as the "distance" between $\hat{\sigma}$ and σ increases, $\tilde{t}_\sigma$ increases.

To identify if a resonance is present in the spectrum, the null hypothesis of having no signal is tested. That is, the result of $\tilde{t}_0$ and the corresponding p-value must be established for different hypothetical masses. To accomplish this, 10000 pseudo-experiments following the null distribution were simulated. The null distribution was determined using $\hat{\hat{n}}_b$ and $\hat{\hat{\lambda}}$ of the data when $\sigma = 0$. As an example, the $\tilde{t}_0$ distribution of the pseudo-experiments when testing for $M_X = 920$ GeV is shown in Figure 6.15. The blue arrow shows where the $\tilde{t}_0$ of the data lies. The p-value is obtained by integrating the distribution to the right of the arrow. The resulting p-value is 0.0074 corresponding to a resonance significance of 2.43 standard deviations, where the significance Z is defined as

$$Z = \Phi^{-1}(1-p) \ , \tag{6.4}$$

where $\Phi^{-1}(x)$ is the quantile of the standard Gaussian (inverse of the cumulative

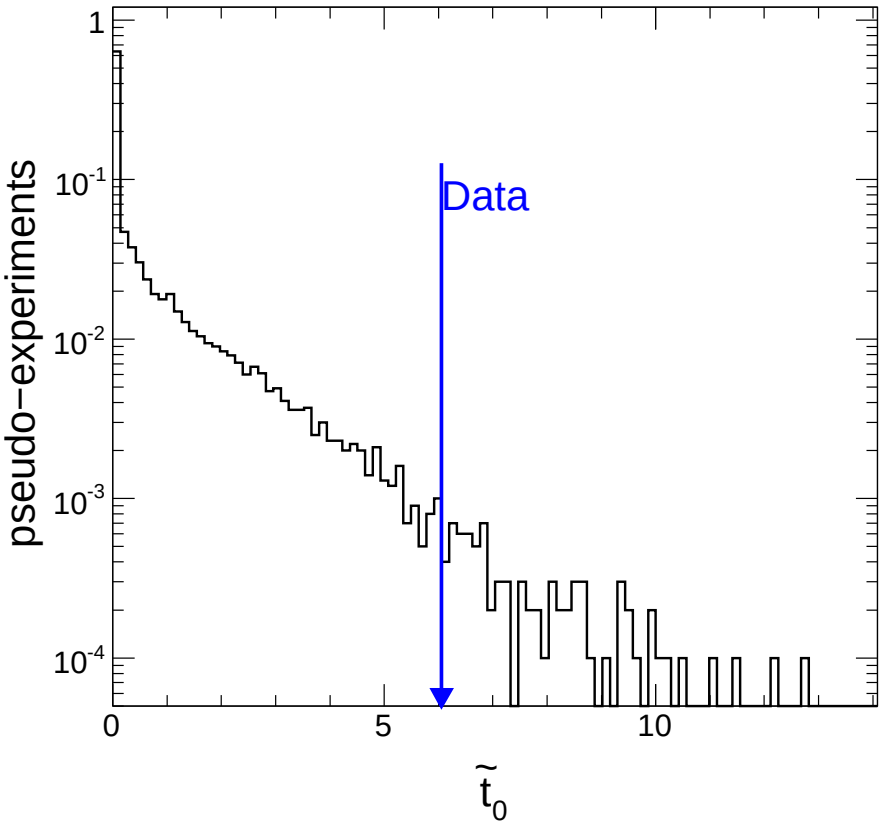

Figure 6.15: The distribution of $\tilde{t}_0$ for 10000 pseudo-experiments drawn from the null hypothesis. The test is performed with M_X = 920 GeV. The blue arrow shows the value of $\tilde{t}_0$ obtained for the data.

distribution), [34]. This confirms the excess of data that can be seen in Figure 6.11 around 920 GeV. However, it is too small to claim evidence of resonances. Table 6.5 shows the p-value and significance for other masses M_X and $M_{Z'}$.

No "evidence" of resonances (significance greater than 3 standard deviations) could be identified in the spectrum.

M_X tested [GeV]	p-value	significance
760	1	-
840	1	-
920	0.0074	2.42
1000	0.0168	2.1248
$M_{Z'}$ tested [GeV]	p-value	significance
700	1	-
800	1	-
1000	0.0084	2.39

Table 6.5: The p-value and significance when testing the null hypothesis for different M_X and $M_{Z'}$.

6.3.5 Excluding Resonances

Since no evidence of resonances in the $M_{t\bar{t}}$ spectrum has been found, an upper limit on the production cross section of particles with different M_X and $M_{Z'}$ can be obtained (σ_{up}). To achieve this goal, the test statistic $\tilde{t}_\sigma$ has to be modified slightly. "Anomalous" needs to be redefined as estimating a cross section ($\hat{\sigma}$) smaller than the cross section of the hypothesis tested (σ). This is consistent with the need to answer the following question: what is the probability of observing a signal as small or smaller than what is observed, given that a signal exists with a cross section σ? The new statistical test is [34],

$$\tilde{q}_\sigma = \begin{cases} \tilde{t}_\sigma & \hat{\sigma} \leq \sigma \\ 0 & \hat{\sigma} > \sigma \end{cases} . \tag{6.5}$$

Integrating the $\tilde{q}_\sigma$ distribution of the pseudo-experiments from $\tilde{q}_\sigma|_{data}$ to infinity is equivalent to integrating the $\hat{\sigma}$ distribution from minus infinity to $\hat{\sigma}|_{data}$. This corresponds to a single sided limit test. If $\tilde{t}_\sigma$ were used instead, integrating the $\tilde{t}_\sigma$ distribution from $\tilde{t}_\sigma|_{data}$ to infinity would result in performing a double sided limit; two different $\hat{\sigma}$ give the same $\tilde{t}_\sigma|_{data}$, one below the σ of the hypothesis (σ_{below}) and one above (σ_{above}). Integrating the $\tilde{t}_\sigma$ distribution from $\tilde{t}_\sigma|_{data}$ to infinity is equivalent to integrating the $\hat{\sigma}$ distribution below σ_{below} and above σ_{above}.

To exclude cross sections equal or larger than σ_{up} at 95% Confidence Level (CL) for a given M_X or $M_{Z'}$[7], the p-value using the test statistic $\tilde{q}_\sigma$ is obtained for different σ hypotheses. The p-value is obtained as described in section 6.3.4 but with $\tilde{q}_\sigma$ replacing $\tilde{t}_\sigma$. For each hypothesis, the 10000 pseudo-experiments are drawn from the $M_{t\bar{t}}$ distribution described by the σ, $\hat{\hat{n}}_b$ and $\hat{\hat{\lambda}}$ obtained from fitting the data. The number of events per pseudo-experiment (N) is drawn from a Poisson distribution with expectation value equals to $\hat{\hat{n}}_b + n_s(\sigma)$. Figure 6.16 shows the fit to the data for different σ hypotheses.

As the σ hypothesis increases, the p-value of the data is expected to decrease. The σ hypothesis corresponding to a p-value equal to 0.05 is taken as the upper limit at 95% CL on the cross section of particle X or Z′, σ_{up} at 95% CL. In practice, σ_{up} is obtained through linear interpolation in the p-values obtained for the different σ hypotheses tested. Keeping the same example with $M_X = 920$ GeV, Figure 6.17 shows

[7] It will not be always mentioned explicitely in the text, but a 95% CL upper limit on the cross section is always obtained as a function of the mass tested for a given model, M_X or $M_{Z'}$.

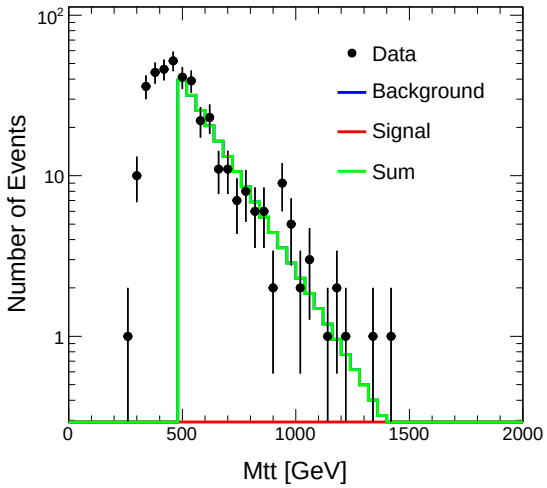

(a) Cross section $\sigma = 0$ pb

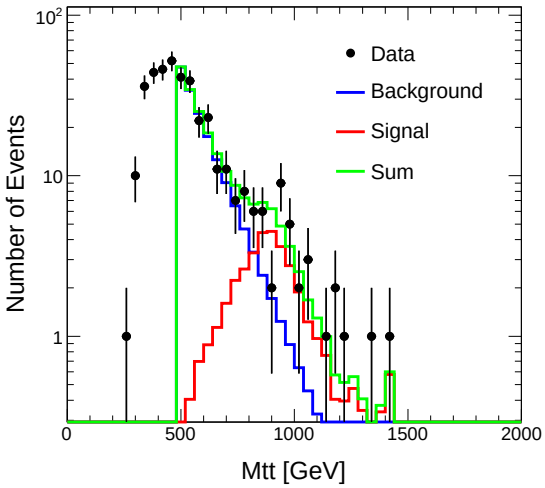

(b) Cross section $\sigma = 16.6$ pb

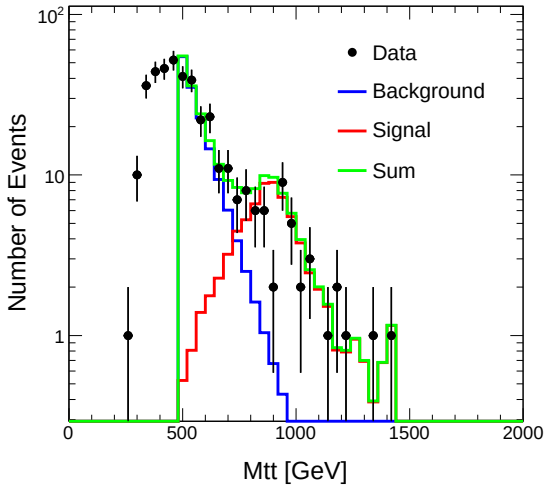

(c) Cross section $\sigma = 33.3$ pb

Figure 6.16: The likelihood fit of the data for the following hypotheses, $\sigma = 0$ pb, $\sigma = 16.6$ pb, $\sigma = 33.3$ pb and $M_X = 920$ GeV. The blue, red and green histograms correspond to the fitted background, signal and to sum of both respectively. The background function is converted into an histogram for display purpose only.

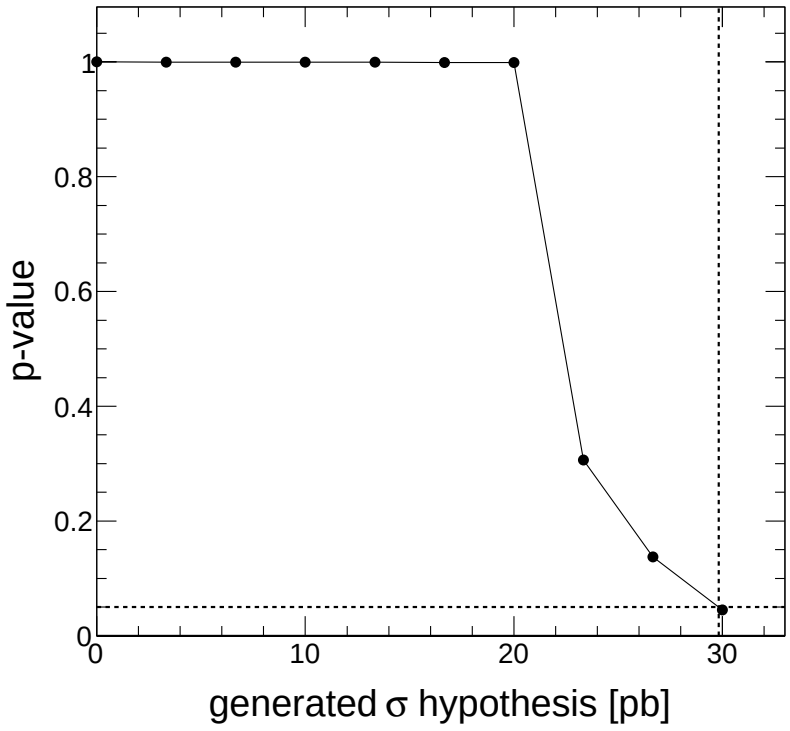

Figure 6.17: The p-value of the data as a function of the generated σ hypothesis for $M_X = 920$ GeV. The horizontal dashed line shows the 0.05 mark, and the vertical dashed line show where the p-value cross this mark.

the data p-value as a function of the σ hypothesis. The σ hypothesis corresponding to a p-value of 0.05 is 29.8 pb. This corresponds to σ_{up} at 95% CL for $M_X = 920$ GeV.

From Figure 6.17 and equation (6.5), it can also be deduced that the most likely cross section, $\hat{\sigma}$ for $M_X = 920$ GeV is near 20 pb, where the p-value starts to move away from one. The distributions of the estimators $\hat{\sigma}$, $\hat{n}_b$ and $\hat{\lambda}$ for some of the cross sections tested, $\sigma = 0$ pb, $\sigma = 16.6$ pb, $\sigma = 33.3$ pb with $M_X = 920$ GeV are shown in Figures 6.18, 6.19 and 6.20 respectively. In particular, the distribution of the $\hat{\sigma}$ estimator, Figure 6.18 shows the most likely signal cross section for the data (blue arrow), and it is indeed 20 pb. It also helps to visually understand how σ_{up} is established. The distribution of $\hat{\sigma}$ for the pseudo-experiments is centered around the σ hypothesis. As the σ hypothesis increases, the distribution shifts to the right. However, the $\hat{\sigma}$ of the data ($\hat{\sigma}|_{data}$) does not change. For a given σ hypothesis, the probability of obtaining $\hat{\sigma} \leq \hat{\sigma}|_{data}$ is equal to 5%; this σ hypothesis is σ_{up} at 95% CL.

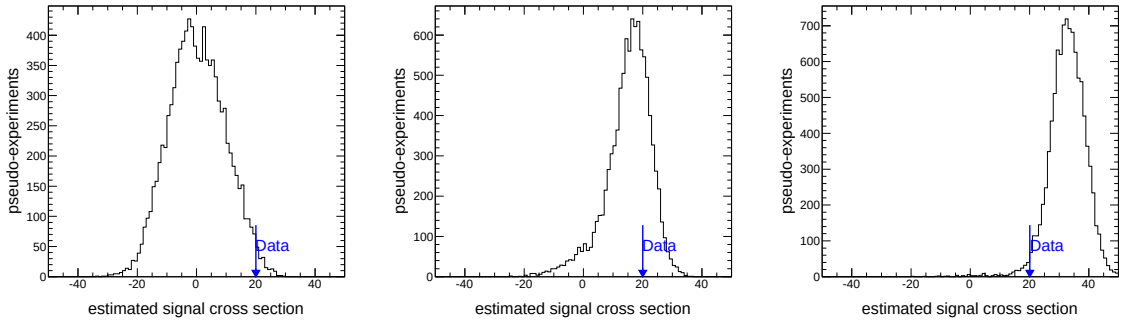

(a) Hypothesis $\sigma = 0$ pb. (b) Hypothesis $\sigma = 16.6$ pb. (c) Hypothesis $\sigma = 33.3$ pb.

Figure 6.18: Distribution of the estimators $\hat{\sigma}$ for three different signal cross section hypotheses.

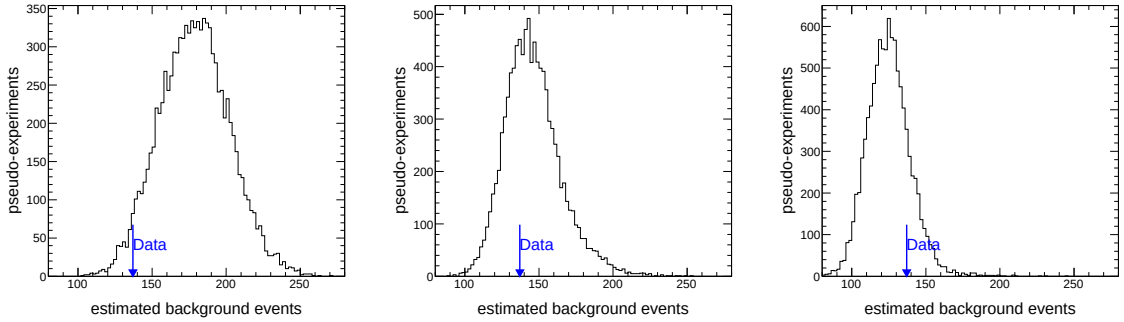

(a) Hypothesis $\sigma = 0$ pb. (b) Hypothesis $\sigma = 16.6$ pb. (c) Hypothesis $\sigma = 33.3$ pb.

Figure 6.19: Distribution of the estimators $\hat{n}_{\mathrm{b}}$ for three different signal cross section hypotheses.

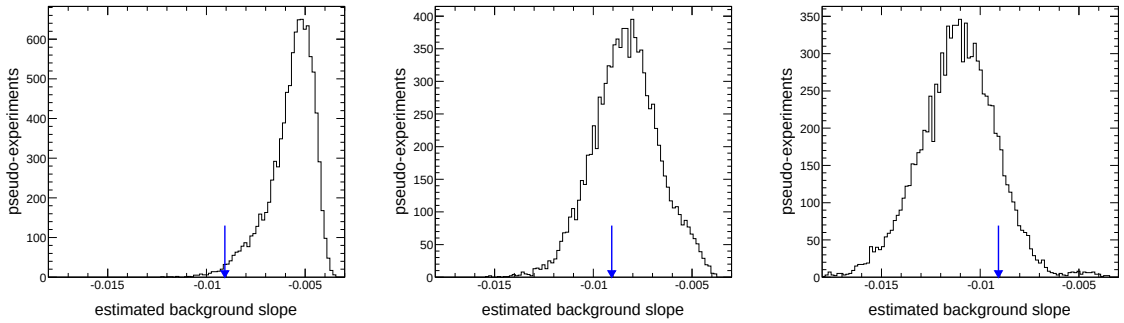

(a) Hypothesis $\sigma = 0$ pb. (b) Hypothesis $\sigma = 16.6$ pb. (c) Hypothesis $\sigma = 33.3$ pb.

Figure 6.20: Distribution of the estimators $\hat{\lambda}$ for three different signal cross section hypotheses.

To evaluate the expected statistical variation on the σ_{up} measurement, an extra 10000 pseudo-experiments were generated under the null hypothesis ($\sigma = 0$). Each of these pseudo-experiments underwent the same treatment as the data to estimate σ_{up}. Figure 6.21 and 6.22 show σ_{up} as a function of the M_X and $M_{Z'}$ tested. The value of σ_{up} between the tested masses is interpolated linearly. The dashed line represents σ_{up} obtained for the data. The plain line represents the expected result under the null hypothesis, the σ_{up} median of the 10000 pseudo-experiments. The green and blue bands represent the 68% and 95% confidence bands around the expected σ_{up}. They are such that there is 68% (95%) of the pseudo-experiments that yield a σ_{up} within the green (blue) band, with equal probability about the median. Table 6.6 shows the σ_{up} obtained and expected for the masses tested.

The lower edge of the 95% confidence band should extend to zero. This follows from the definition of σ_{up} at 95% CL which indicates the lowest σ hypothesis that has a p-value smaller than 0.05. Combining this with the definition of the p-value, 5% of the pseudo-experiments generated under the null ($\sigma = 0$) hypothesis to estimate the coverage band should have a p-value smaller than 0.05 when the hypothesis tested is the null hypothesis. That is, 5% of these pseudo-experiments should have σ_{up} at 95% CL equal to zero such that the lower band of the 95% coverage extends to zero. The test statistic of equation (6.5) can lead to thinking that this should not be the case since for the $\sigma = 0$ hypothesis, the test always returns zero. The p-value is therefore one, or rather not defined, for a tested σ hypothesis of exactly zero. However, the degeneracy is completely lifted for all the pseudo-experiments that have $\hat{\sigma} < \sigma$ for any $\sigma > 0$, independently of how close σ is from zero. In Figures 6.21 and 6.22, the 95% confidence band does not go as low as zero. This is because the σ hypotheses are not tested continuously. For the X and Z′ models respectively, the σ hypothesis is tested in increasing steps of $1/0.30 = 3.33$ pb and 3 pb. Since a linear interpolation is done between the p-value of 1 at $\sigma = 0$ and the first non-zero σ hypothesis, the smallest σ_{up} at 95% CL that can be found is 3.16 pb and 2.85 pb respectively for the X and Z′ models. This is not a significant issue as long as these numbers, 3.16 pb and 2.85 pb, are small compared to the 95% coverage band width which is around 40 pb.

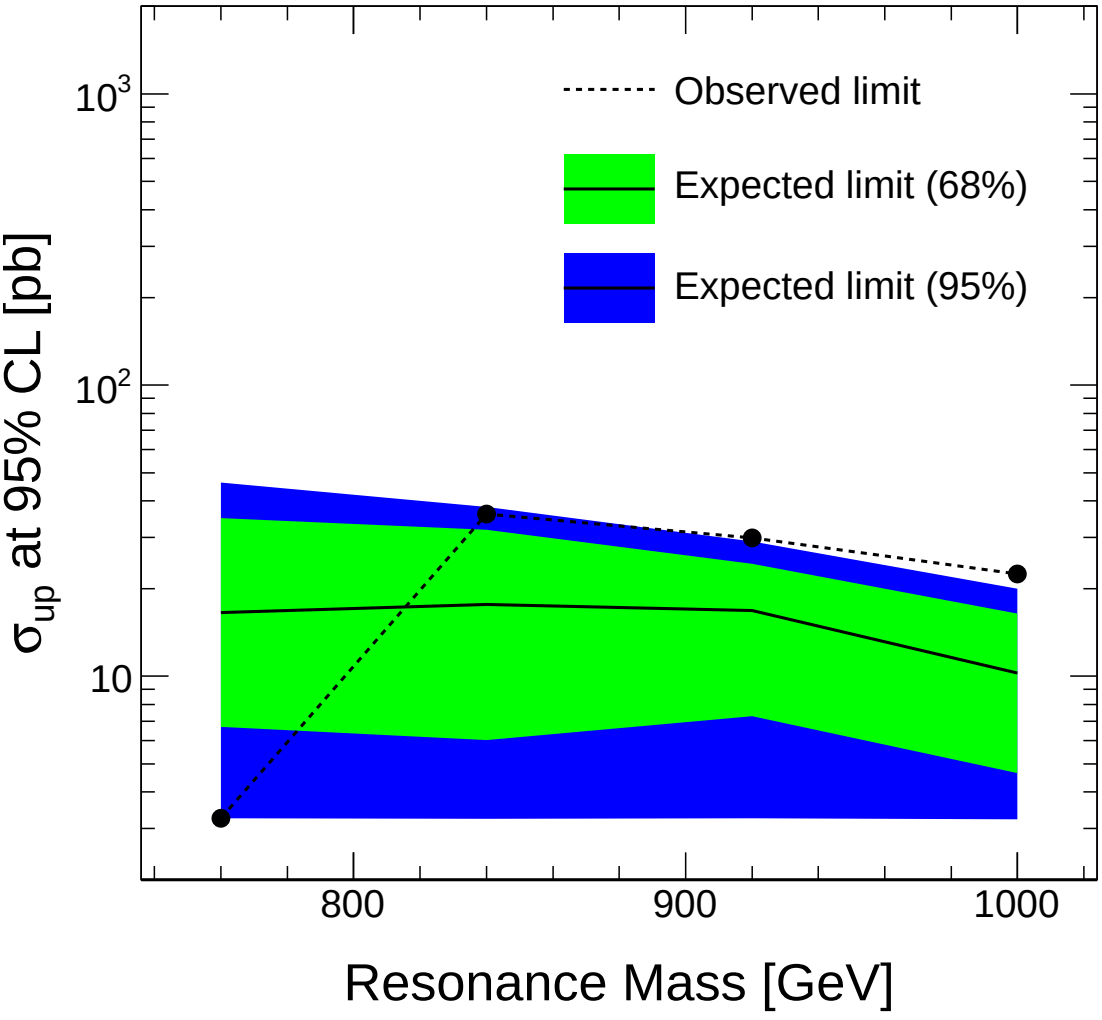

Figure 6.21: The upper limit on the cross section times Br[X $\rightarrow t\bar{t}$] (σ_{up}) of a particle X at 95% CL as a function of the mass of the particle M_X on a logarithmic scale. The dashed line represents the value obtained from data, while the plain line represents the expected value. The green and blue bands represent respectively the 68% and 95% confidence bands. This result does not take into account systematic errors.

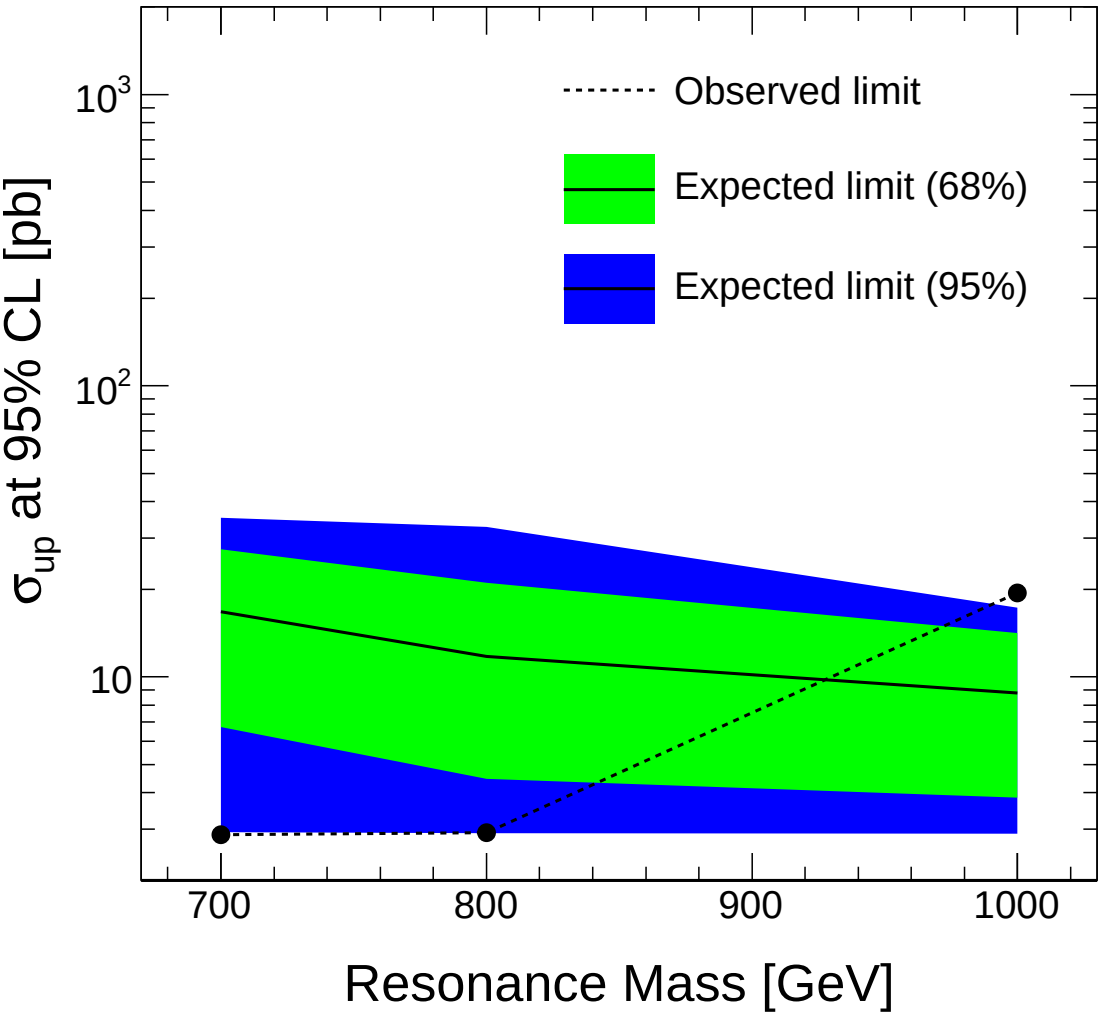

Figure 6.22: The upper limit on the cross section times Br[$Z' \to t\bar{t}$] (σ_{up}) of a Z' particle at 95% CL as a function of the mass of the particle $M_{Z'}$ on a logarithmic scale. The dashed line represents the value obtained from data, while the plain line represents the expected value. The green and blue bands represent respectively the 68% and 95% confidence bands. This result does not take into account systematic errors.

M_X [GeV]	Observed	Expected (68% coverage)	Expected (95% coverage)
760	3.2	$16.5^{+18.4}_{-9.8}$	$16.5^{+29.7}_{-13.3}$
840	36.0	$17.6^{+14.1}_{-11.6}$	$17.6^{+20.5}_{-14.4}$
920	29.8	$16.8^{+7.5}_{-9.5}$	$16.8^{+12.2}_{-13.6}$
1000	22.5	$10.2^{+6.2}_{-5.6}$	$10.2^{+9.7}_{-7.0}$
$M_{Z'}$ [GeV]	Observed	Expected (68% coverage)	Expected (95% coverage)
700	2.9	$16.7^{+10.7}_{-10.0}$	$16.7^{+18.4}_{-13.8}$
800	2.9	$11.7^{+9.3}_{-7.3}$	$11.7^{+21.0}_{-8.8}$
1000	19.4	$8.8^{+5.3}_{-5.0}$	$8.8^{+8.5}_{-5.9}$

Table 6.6: The upper limit on the cross section times Br[$X \to t\bar{t}$] (σ_{up}) of a particle X or Z′ at 95% CL with different masses. The observed limit is given as well as the expected median and the error extracted from the 68% and 95% coverage bands. No systematic errors are considered.

6.3.6 Systematic Errors

Up to this point, only statistical errors were considered. Errors that bias measured values, independently of the number of data collected, are called systematic errors. Since the background is estimated directly from the data, systematic errors do not affect its evaluation as long as the exponential shape of its distribution is not affected. Nevertheless, systematic errors will affect the signal evaluation in two ways.

First, $\hat{\sigma}$ is estimated using $n_s = \mathcal{L}\epsilon\sigma \mathrm{Br}[t\bar{t} \to (\mathrm{e\ or\ } \mu)]$. If there is an error in the measurement of $\mathcal{L}$ or ϵ, this will affect $\hat{\sigma}$. The error on $\mathcal{L}$ is known to be 3.2%, [35]. The error on the efficiency ϵ is complex to evaluate since many systematic errors can affect its value. The two main systematic errors on which ϵ depends are the Jet Energy Scale (JES) (ν_{JES}), section 3.3.3, and the b-tag Scale Factor (SF) (ν_{SF}), section 3.3.4, [28]. In general, ν will be used to refer to the systematic errors in units of their standard deviation. For example, $\nu_{\mathrm{JES}} = -1$ refers to a real value for the JES of one standard deviation lower than what was used in the analysis. Figure 6.23 shows the effect of ν_{JES} and ν_{SF} on the efficiency. The b-tag SF has a drastic effect on the efficiency. Going from ν_{SF} = -2 to ν_{SF} = 2 changes the efficiency from 10% to 35%. Since the efficiency affects n_s linearly, it is clear that considering this systematic error in the analysis will significantly reduce the ability to exclude resonances.

The second way in which the systematic errors can affect the analysis is in the evaluation of the signal shape. The b-tag SF has a negligible impact; however, JES and JER significantly affect the shape of the signal. For example, Figure 6.24 shows the different $\mathrm{M}_{t\bar{t}}$ distributions of $\mathrm{M_X}$ = 920 GeV for ν_{JES} = -2, 0 and 2. The shift in the peak position is about 200 GeV.

To obtain $\epsilon(\vec{\nu})$ and $f_s(\mathrm{M}_{t\bar{t}}|\vec{\nu})$, where $\vec{\nu} = (\nu_{\mathrm{SF}}, \nu_{\mathrm{JES}}, \nu_{\mathrm{JER}})$, MC simulations are performed with $\vec{\nu}$, the new value of the b-tag SF, JES and JER. A three-dimensional grid with points at $\nu_{\mathrm{SF}} \in \{-2, -1, 0, 1, 2\}$, $\nu_{\mathrm{JES}} \in \{-2, -1, 0, 1, 2\}$, and $\nu_{\mathrm{JER}} \in \{0, 1\}$, for a total of 50 points, is formed. The efficiency $\epsilon(\vec{\nu})$ is then obtained through linear interpolation in this three-dimensional grid. In the case of $f_s(\mathrm{M}_{t\bar{t}}|\vec{\nu})$, a fourth dimension is added to the grid to allow an interpolation in $\mathrm{M}_{t\bar{t}}$. The grid points are $\mathrm{M}_{t\bar{t}} \in \{500, 501, 502, \ldots, 1400\ \mathrm{GeV}\}$. This fourth dimension does not require extra MC simulations since it simply corresponds to different $\mathrm{M}_{t\bar{t}}$ points in the reconstructed $\mathrm{M}_{t\bar{t}}$ distribution.

The likelihood of equation (6.2) must be modified to include the systematic errors, $L(\sigma, n_b, \lambda) \to L(\sigma, n_b, \lambda, \mathcal{L}, \vec{\nu})$. Adding more parameters will reduce the fit's

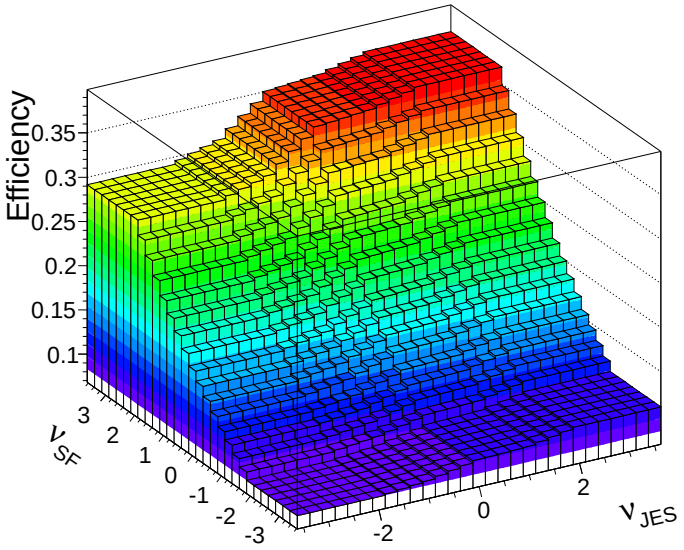

Figure 6.23: The effect of ν_{JES} and ν_{SF} on the efficiency in the lepton + jets channel. The efficiency plotted is the efficiency times the ratio of the event that falls under the range of the fit 500-1400 GeV. This plotted efficiency is the efficiency that is used in the likelihood function.

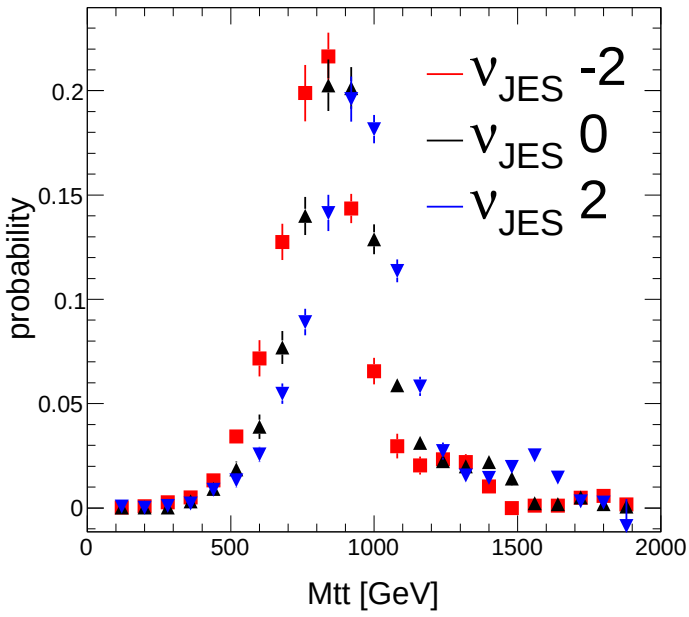

Figure 6.24: $M_{t\bar{t}}$ distribution of M_X = 920 GeV for variations of the jet energy scale, ν_{JES} = -2, 0 and 2.

ability to accurately estimate any of the parameters. This includes the parameter of interest, σ. The parameters from the systematic errors are often referred as nuisance parameters. The obvious generalization for $L(\sigma, n_{\rm b}, \lambda) \rightarrow L(\sigma, n_{\rm b}, \lambda, \mathcal{L}, \vec{\nu})$ is to change $n_{\rm s}(\sigma) = \mathcal{L}\epsilon\sigma{\rm Br}[{\rm t\bar{t}} \rightarrow ({\rm e\ or\ }\mu)]$ to $n_{\rm s}(\sigma, \mathcal{L}, \vec{\nu}) = \mathcal{L}\epsilon(\vec{\nu})\sigma{\rm Br}[{\rm t\bar{t}} \rightarrow ({\rm e\ or\ }\mu)]$ and $f_{\rm s}({\rm M_{t\bar{t}}})$ to $f_{\rm s}({\rm M_{t\bar{t}}}|\vec{\nu})$. Nevertheless, not all the $\vec{\nu}$ should have the same weight when maximizing the likelihood. The probability of measuring $\vec{\nu} = (0, 0, 0)$ given the real $\vec{\nu}$ needs to be profiled. Therefore, the likelihood needs to be modified by multiplying it by the pdf of the systematic error measurements. This is consistent with the frequentist approach, for each systematic i, this pdf is interpreted as the probability of measuring $\nu_{\rm i} = 0$ given the real $\nu_{\rm i}$. This contrasts with the Baysian approach which would consider the probability of parameter $\nu_{\rm i}$ given a prior degree of belief. The pdfs are assumed to be Gaussian distributions with a probability of having $\vec{\nu}$ outside the grid set to zero ($G_{\rm trunc}$)[8]. The modified (profiled) likelihood that includes systematic errors is,

$$\begin{aligned} L(\sigma, n_{\rm b}, \lambda, \mathcal{L}, \vec{\nu}) &= {\rm P(N}|n_{\rm b} + n_{\rm s}) \prod_{\rm j}^{\rm N} \left[\frac{n_{\rm b} f_{\rm b}({\rm M^j_{t\bar{t}}}|\lambda)}{n_{\rm b} + n_{\rm s}} + \frac{n_{\rm s} f_{\rm s}({\rm M^j_{t\bar{t}}}|\vec{\nu})}{n_{\rm b} + n_{\rm s}} \right] \\ &\times G_{\rm trunc}(\mathcal{L}_{\rm m}|\mathcal{L}, \Delta\mathcal{L}^2) \prod_{\rm i} G_{\rm trunc}(0|\nu_{\rm i}, 1) \ , \end{aligned} \tag{6.6}$$

where $\mathcal{L}_{\rm m}$ is the measured integrated luminosity and $n_{\rm s} \equiv n_{\rm s}(\sigma, \mathcal{L}, \vec{\nu})$. Figures 6.25, 6.26 and 6.27 show the equivalent of Figures 6.18, 6.19 and 6.20 when the likelihood of equation (6.6) is used instead of the one of equation (6.2). The focus of the comparison will be around Figure 6.25 versus 6.18 since $\hat{\sigma}$ is the parameter of interest. It can be observed that profiling the likelihood did not significantly change the estimation of $\hat{\sigma}|_{\rm data}$ (the blue arrow remains roughly at the same value of $\hat{\sigma}$). Using the profiled likelihood widens the distributions slightly. The major change between 6.25 and 6.18 is the shift of the distribution mean as a function of the σ hypothesis. The center of the distribution does not increase as fast when the profiled likelihood is used. In particular, for Figure 6.18 (c), the distribution is centered around the hypothesis $\sigma =$ 33.3 pb as expected. However, this is not the case for Figure 6.25 (c). It is centered around a lower $\hat{\sigma}$, 25 pb. This indicates, as expected, that it is harder to exclude

[8]This is not an unreasonable assumption. The probability of having the b-tag SF or JES uncertainty miss-estimated by more than 2 standard deviations in ATLAS is extremely low, definitively less than the 5% that a Gaussian predicts. Mathematically, the distribution is assumed to have an excess kurtosis smaller than 0. A truncated Gaussian distribution has this property.

resonances when systematic errors are considered. It can be further understood from Figures 6.28 and 6.29 which show the $\hat{\hat{\nu}}_{\mathrm{SF}}$ and $\hat{\hat{\nu}}_{\mathrm{JES}}$ estimators when σ is *fixed* to 0 pb, 16.6 pb and 33.3 pb. The word fixed is emphasized here to mark a major difference with the previous Figures 6.18-6.20 and 6.25-6.27 where the $\hat{\sigma}$ is free. That is, Figures 6.18-6.20 and 6.25-6.27 show single hat estimators, while Figures 6.28 and 6.29 show double hat estimators. It can be observed that as the σ hypothesis is increased, $\hat{\hat{\nu}}_{\mathrm{SF}}$ and $\hat{\hat{\nu}}_{\mathrm{JES}}$ are more likely to be estimated with negative values. From Figure 6.23, it is known that this will reduce the efficiency ϵ. This is confirmed in Figure 6.30 which shows ϵ evaluated at the value of the estimated $\hat{\hat{\vec{\nu}}}$ for the pseudo-experiments and data. As the σ hypothesis is increased, the likelihood fit chooses values of $\hat{\hat{\vec{\nu}}}$ such that the efficiency is reduced. This way, $n_{\mathrm{s}}(\sigma, \mathcal{L}, \vec{\nu})$ increases slower than linearly with σ. The pseudo-experiments are generated with these shifted estimated nuisance parameters from the data; the pseudo-experiments are generated with a smaller n_{s} than $n_{\mathrm{s}}(\sigma, \mathcal{L} = \mathcal{L}_{\mathrm{m}}, \vec{\nu} = (0,0,0))$. This is why the $\hat{\sigma}$ distribution of the pseudo-experiments with $\sigma = 33.3$ pb hypothesis is centered at 25 pb instead of 33.3 pb. The value of $n_{\mathrm{s}}(\sigma = 25 \text{ pb}, \mathcal{L} = \mathcal{L}_{\mathrm{m}}, \vec{\nu} = (0,0,0))$ must be equal to $n_{\mathrm{s}}(\sigma = 33.3 \text{ pb}, \hat{\hat{\mathcal{L}}}, \hat{\hat{\vec{\nu}}})$. When $\hat{\sigma}$ is free, $n_{\mathrm{s}}(\hat{\sigma}, \hat{\mathcal{L}}, \hat{\vec{\nu}})$ can be directly adjusted using $\hat{\sigma}$. The likelihood fit hence avoids the "cost" of evaluating the $\hat{\vec{\nu}}$ away from $\vec{\nu} = (0,0,0)$ and $\hat{\mathcal{L}}$ away from $\mathcal{L}_{\mathrm{m}}$.

In summary, $\hat{\sigma}|_{\mathrm{data}}$ does not change appreciably when systematic errors are considered. However, the center of the $\hat{\sigma}$ distribution of the pseudo-experiments is shifted to a lower value than the σ hypothesis. It therefore takes a larger σ hypothesis to obtain a p-value that equals 0.05. Figure 6.31 shows an example when $\mathrm{M_X} = 920$ GeV. This figure should be compared with Figure 6.17 for which the same $\mathrm{M_X}$ was considered, but without systematic error. The p-value of 0.05 is reached for a lower value of σ in Figure 6.17 than in Figure 6.31.

The final result on the σ_{up} at 95% CL as a function of $\mathrm{M_X}$ and $\mathrm{M_{Z'}}$ when the systematic errors are included can be seen in Figures 6.32 and 6.33 respectively. Table 6.7 shows the σ_{up} obtained and expected for various $\mathrm{M_X}$ and $\mathrm{M_{Z'}}$ tested when the systematic errors are considered.

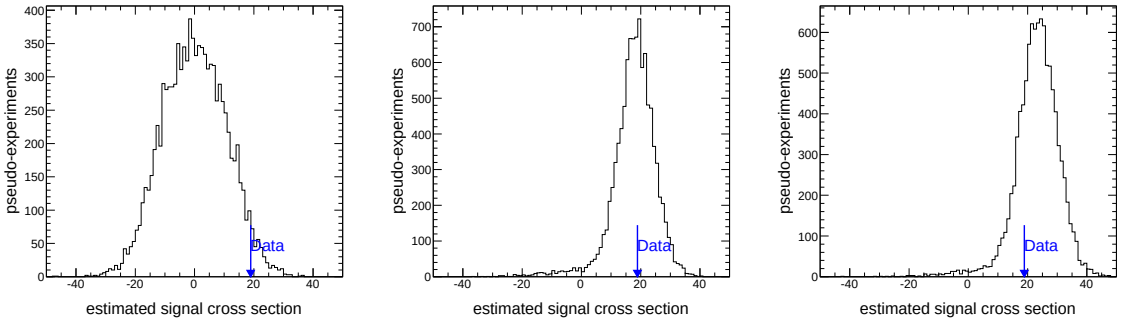

(a) Hypothesis $\sigma = 0$ pb. (b) Hypothesis $\sigma = 16.6$ pb. (c) Hypothesis $\sigma = 33.3$ pb.

Figure 6.25: Distribution of the estimators $\hat{\sigma}$ for the profiled likelihood for three different signal cross section hypotheses.

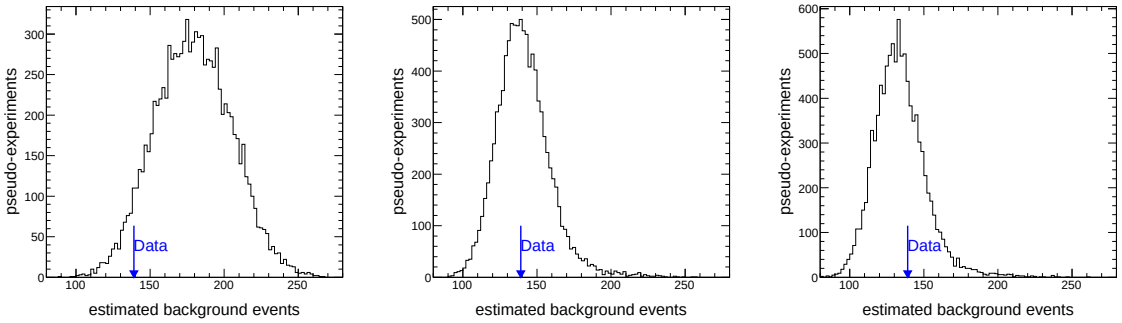

(a) Hypothesis $\sigma = 0$ pb. (b) Hypothesis $\sigma = 16.6$ pb. (c) Hypothesis $\sigma = 33.3$ pb.

Figure 6.26: Distribution of the estimators $\hat{n}_{\mathrm{b}}$ for the profiled likelihood for three different signal cross section hypotheses.

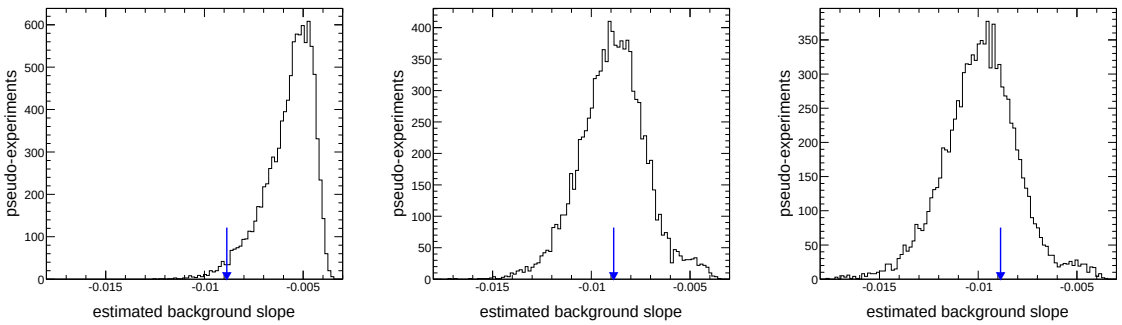

(a) Hypothesis $\sigma = 0$ pb. (b) Hypothesis $\sigma = 16.6$ pb. (c) Hypothesis $\sigma = 33.3$ pb.

Figure 6.27: Distribution of the estimators $\hat{\lambda}$ for the profiled likelihood for three different signal cross section hypotheses.

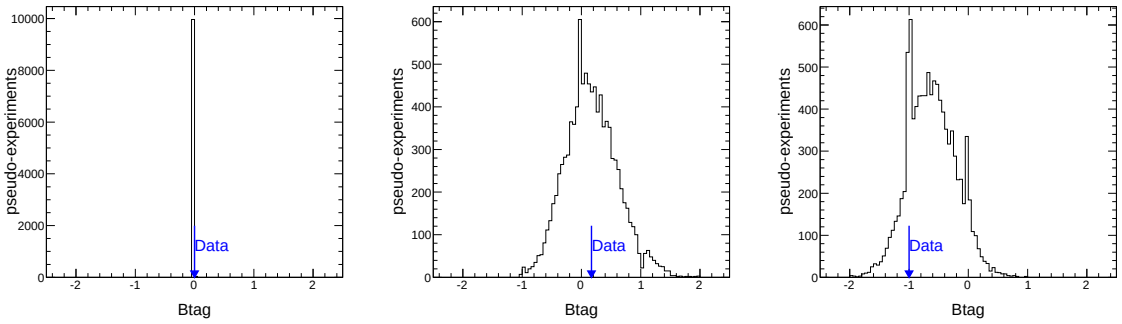

(a) Hypothesis $\sigma = 0$ pb. (b) Hypothesis $\sigma = 16.6$ pb. (c) Hypothesis $\sigma = 33.3$ pb.

Figure 6.28: Distribution of the estimators $\hat{\hat{\nu}}_{\mathrm{SF}}$ for the profiled likelihood for three different signal cross section hypotheses.

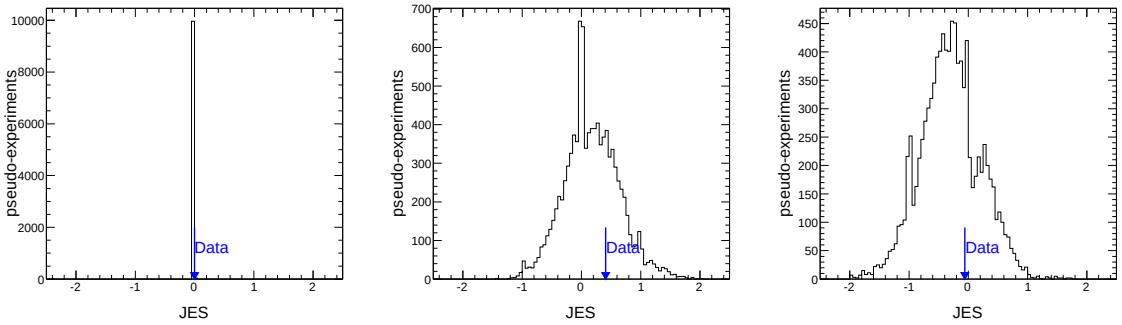

(a) Hypothesis $\sigma = 0$ pb. (b) Hypothesis $\sigma = 16.6$ pb. (c) Hypothesis $\sigma = 33.3$ pb.

Figure 6.29: Distribution of the estimators $\hat{\hat{\nu}}_{\mathrm{JES}}$ for the profiled likelihood for three different signal cross section hypotheses.

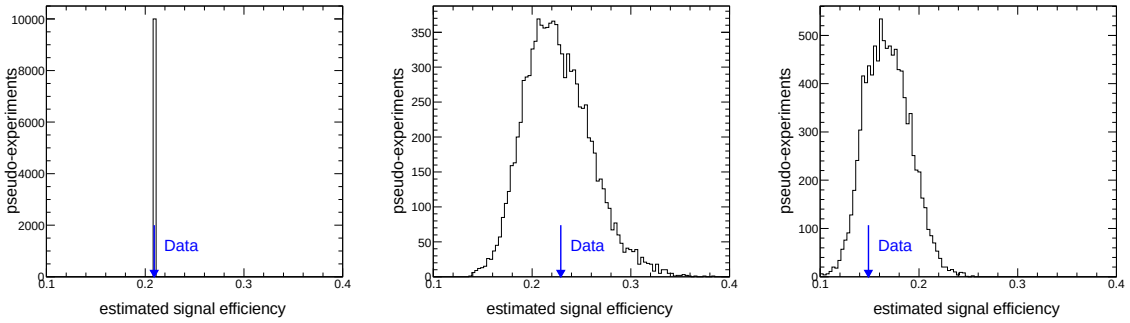

(a) Hypothesis $\sigma = 0$ pb. (b) Hypothesis $\sigma = 16.6$ pb. (c) Hypothesis $\sigma = 33.3$ pb.

Figure 6.30: Distribution of $\epsilon(\hat{\hat{\vec{\nu}}})$ for three different signal cross section hypotheses, where $\hat{\hat{\vec{\nu}}}$ is obtained using the profiled likelihood.

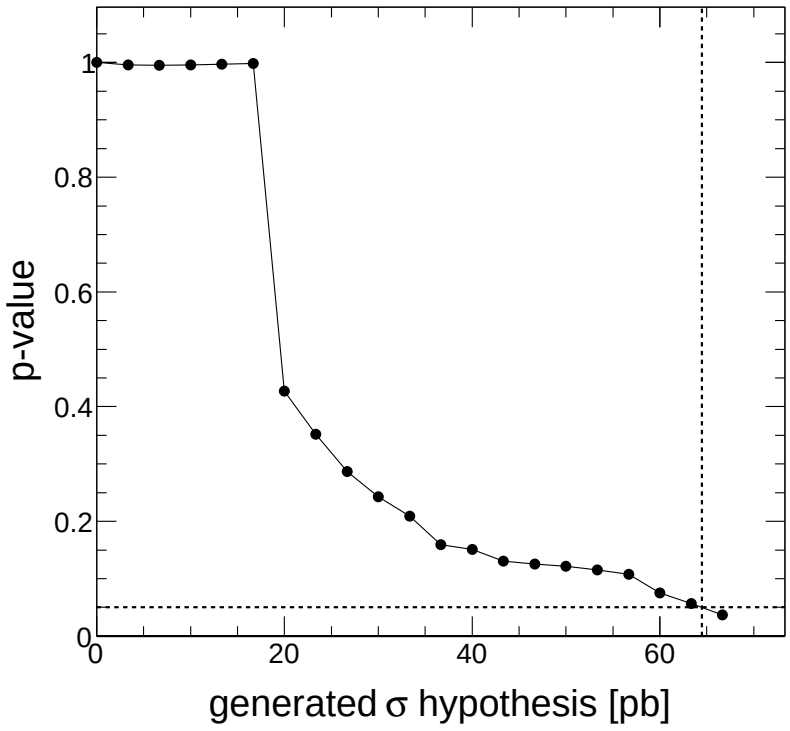

Figure 6.31: The p-value of the data as a function of the generated σ hypothesis for M_X = 920 GeV. The horizontal dashed line shows the 0.05 mark, and the vertical dashed line show where the p-value crosses this mark.

M_X [GeV]	Observed	Expected (68% coverage)	Expected (95% coverage)
760	3.2	$27.9^{+11.3}_{-19.9}$	$27.9^{+118.8}_{-24.6}$
840	75.1	$13.9^{+23.3}_{-8.0}$	$13.9^{+95.7}_{-10.7}$
920	64.5	$12.6^{+47.1}_{-7.1}$	$12.6^{+79.6}_{-9.4}$
1000	77.7	$9.8^{+10.7}_{-5.6}$	$9.8^{+56.1}_{-6.6}$
$M_{Z'}$ [GeV]	Observed	Expected (68% coverage)	Expected (95% coverage)
700	2.9	$55.9^{+56.9}_{-47.0}$	$55.9^{+91.1}_{-53.0}$
800	2.9	$20.1^{+8.8}_{-14.7}$	$20.1^{+44.6}_{-17.1}$
1000	43.4	$7.8^{+8.9}_{-4.7}$	$7.8^{+33.7}_{-4.9}$

Table 6.7: The upper limit on the cross section times Br[$X \to t\bar{t}$] (σ_{up}) of a particle X or Z′ at 95% CL with different masses. The observed limit is given as well as the expected median and the error extracted from the 68% and 95% coverage bands. Systematic errors are considered in this table.

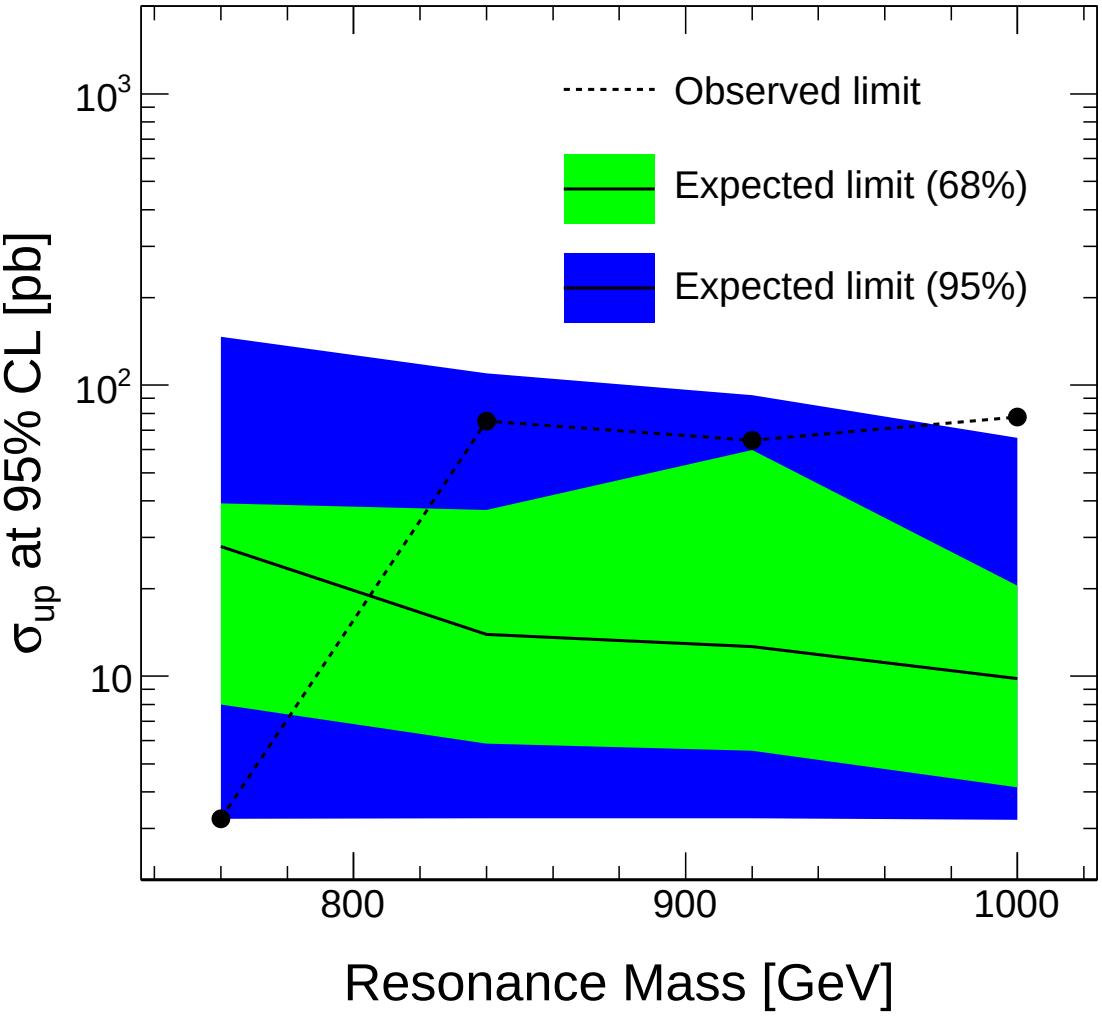

Figure 6.32: The upper limit on the cross section times Br[X $\rightarrow t\bar{t}$] of a particle X at 95% CL as a function of the mass of the particle M_X on a logarithmic scale. The profiled likelihood is used to include systematic errors. The dashed line represent the value obtained from data, while the plain line represent the expected value. The green and blue bands represent respectively the 68% and 95% confidence bands.

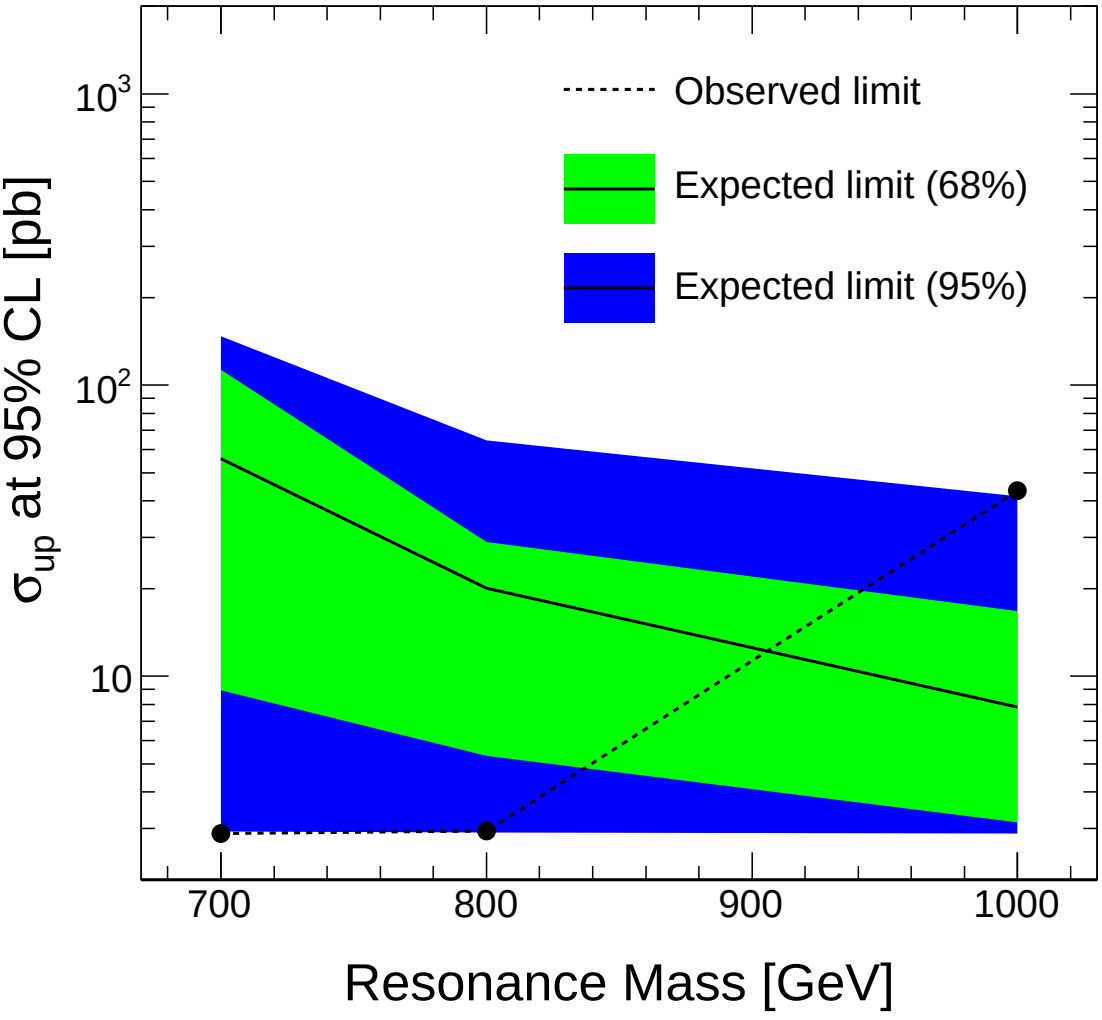

Figure 6.33: The upper limit on the cross section times Br[$Z' \to t\bar{t}$] of a particle Z' at 95% CL as a function of the mass of the particle $M_{Z'}$ on a logarithmic scale. The profiled likelihood is used to include systematic errors. The dashed line represent the value obtained from data, while the plain line represent the expected value. The green and blue bands represent respectively the 68% and 95% confidence bands.

Chapter 7

Discussion

7.1 Interpretation of the Limits Obtained

The analysis was performed using the first data collected at ATLAS at $\sqrt{s} = 7$ TeV. In this data set, the statistics are limited; many improvements are expected in the future concerning the understanding of the detector, the reconstruction algorithms and the organization of the analysis working groups.

The analysis was designed to be model independent. Figures 6.21, 6.22, 6.32 and 6.33 can be viewed as references to compare with various resonance model predictions. In general, the σ_{up} obtained from the data ($\sigma_{\text{up}}|_{\text{data}}$) strongly excludes a resonance with mass between 700 and 800 GeV while $\sigma_{\text{up}}|_{\text{data}}$ for masses higher than 800 GeV are not very restrictive. This is consistent with results obtained in section 6.3.4 where an excess of events was found around $M_X = 920$ GeV and 1000 GeV, and $M_{Z'} = 1000$ GeV, but not for the lower masses. Nevertheless, one of the main conclusion of the σ_{up} analysis is that the error on $\sigma_{\text{up}}|_{\text{data}}$ is large based on the coverage band.

It is possible to get an appreciation of the σ_{up} obtained by converting σ_{up} to the corresponding upper limit at 95% CL on the number of signal event expected ($n_s|_{\text{up}}$). Using equation (6.1) with $\mathcal{L} = 35.3$ pb^{-1}, $\epsilon = 21\%$ and $\text{Br}[t\bar{t} \to (\text{e or } \mu)] = 30\%$, the following relation can be established,

$$n_s|_{\text{up}} = 2.2 \text{ pb}^{-1} \times \sigma_{\text{up}} \ . \tag{7.1}$$

For example, if a σ_{up} of 10 pb is obtained, it can be excluded at 95% CL that a signal leaving on average 22 events or more exists. When there are no systematic errors considered, the expected $n_s|_{\text{up}}$ varies around 30 events, the 68% upper band

varies between 55-75 events and the 95% upper band varies between 65-110 events approximatively. These numbers have to be compared to the total number of events in the fitted range, 179 events. It means that a large fraction of the data could be signal events at 95% CL. Those are therefore very conservative estimates of the σ_{up}. The equation (7.1) can be used only when there are no systematic errors. When there are systematic errors, the $\mathcal{L}$ and ϵ can be reduced significantly, lowering the multiplicative factor in equation (7.1).

7.2 Comparison with Alternative ATLAS Analysis

The obtained σ_{up} at 95% CL are comparable to what was obtained in a similar ATLAS analysis that studied $t\bar{t}$ resonances [28], Figure 7.1. The expected σ_{up} are slightly higher than those of [28], as expected from the strategy chosen for this analysis, namely having more free parameters to describe the $M_{t\bar{t}}$ background spectrum. The width of the coverage bands for the expected σ_{up} is of the same order of magnitude for both analyses, and both results are consistent with each other.

Moreover, analysis [28] does not identify an excess of events in the region between 920 and 1000 GeV contrary to this analysis. For analysis [28], $\sigma_{\text{up}}|_{\text{data}}$ for $M_{Z'} =$ 1000 GeV is actually below the expect σ_{up}. This could be partially explained by this analysis having a slightly different $M_{t\bar{t}}$ spectrum since a different algorithm to estimate $M_{t\bar{t}}$ is used, Figure 7.2. It could also be explained by the fact that the number of data events around this $M_{t\bar{t}}$ region are all below the expected background histogram, Figure 7.2. If the analysis were sensitive to the shape instead of focusing only on a comparison between the number of obtained and expected events by bin of $M_{t\bar{t}}$, this observation could be different, see section 6.3.1.

Another major difference between the analyses is that in analysis [28] σ_{up} decreases significantly as a function of the resonance invariant mass. This is expected since the number of background events decreases as a function of $M_{t\bar{t}}$. It is therefore easier to exclude resonances with high $M_{Z'}$. The reason why this feature is not as pronounced in this analysis is that the expected number of background event is not fixed. When performing the shape analysis, the number of background events at high $M_{t\bar{t}}$ can be decreased as the number of signal events is increased to explained the number of observed events. This is one of the main limitations of the current analysis and will be discussed in detail in the next section.

This analysis makes minimal use of MC simulations and therefore offers more

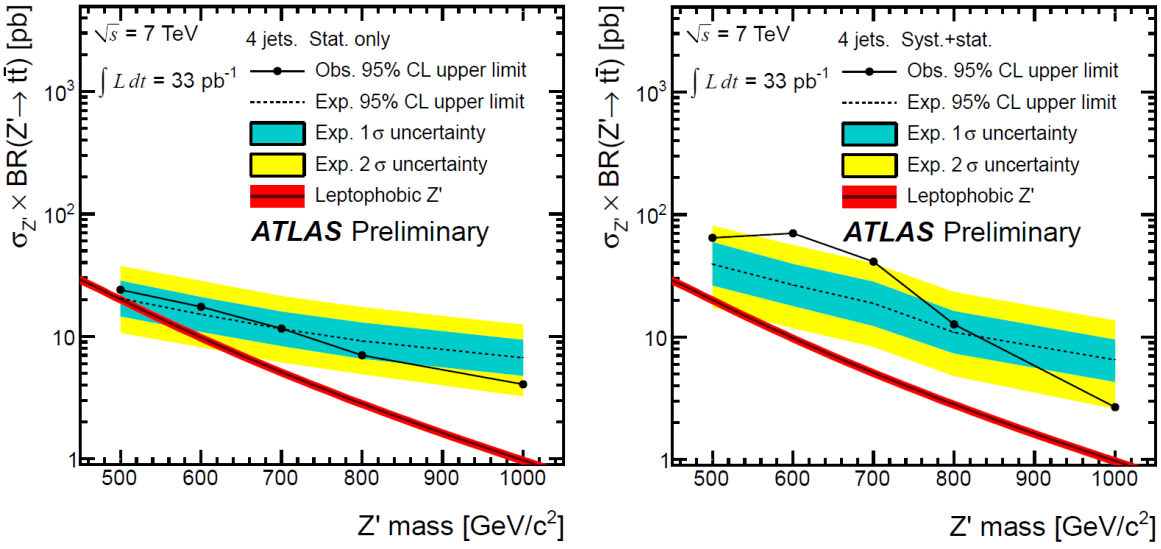

(a) Without systematic error (b) With systematic errors

Figure 7.1: Expected (dashed line) and observed (black points connected by a line) upper limit on the cross section of Z′ ($\sigma_{Z'}$) times Br[Z′ → t$\bar{t}$]. The blue and yellow bands show the range in which the limit is expected to lie in 68% and 95% of the experiments, respectively, and the red points correspond to the predicted crosssections in the topcolor model. The error bars on the topcolor cross-section curve represent the effect of the PDF uncertainty on the prediction [28].

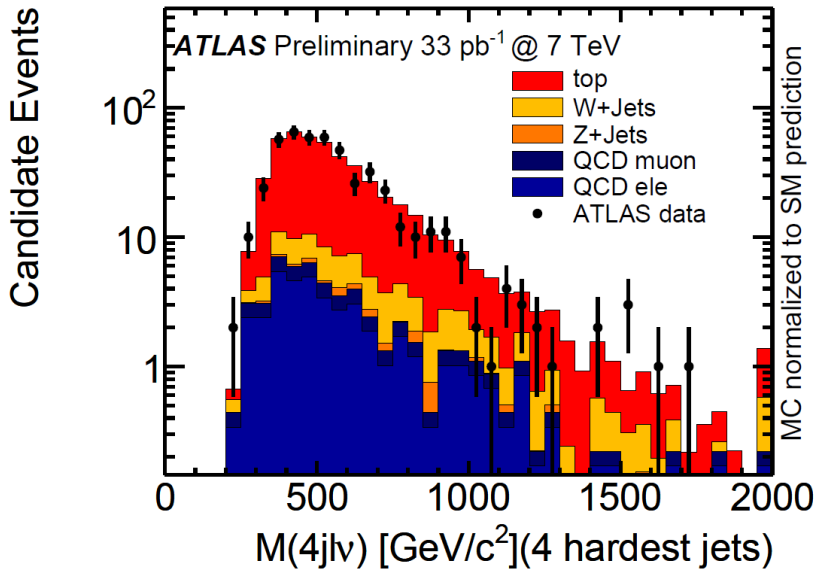

Figure 7.2: Reconstructed t$\bar{t}$ mass using the "four hardest jets" algorithm after all cuts [28].

conservative σ_{up} limits. It is interesting to note that both analyses yield similar expected limits and limit bands despite fundamentally different approaches.

7.3 Limitation of the Analysis

The main limitation of the analysis is the $M_{t\bar{t}}$ resolution. The reconstructed $M_{t\bar{t}}$ for signal events are not contained around the resonance mass; they leak into the entire region of the fit, 500-1400 GeV. Moreover, the resonance spectrum for $M_{t\bar{t}}$ higher than the resonance mass follows an exponential distribution (straight line on a logarithmic plot). Figures 6.16 (b) and (c) offer a good example of these two observations. Having a signal that follows the same distribution than the background when $M_{t\bar{t}}$ is larger than the resonance mass leads to a serious problem; all the events in this region can be uniquely explained by the presence of a signal. Put otherwise, the background events are "pushed away" ($\hat{\lambda}$ is reduced) as the signal size is increased. The relative weight for high $M_{t\bar{t}}$ events in the background fit is suppressed when the cross section of the signal is large. In such circumstances, it is harder to exclude the presence of a resonance.

The issue discussed above also explains why only resonances with masses above 700 GeV were considered. For lower masses, the background fit would lose its handle on events with low $M_{t\bar{t}}$ as well as events with high $M_{t\bar{t}}$ such that the background could not be fitted reliably. That is, for a large enough σ of the signal, the entire $M_{t\bar{t}}$ distribution could be explained by the signal for such masses.

The other major limitation of the analysis is the impact of the systematic errors. The b-tag SF alone can change the reconstruction efficiency from 10% to 35% when ν_{SF} changes from -2 to 2. The efficiency ϵ when no systematic error is considered ($\nu_{SF} = 0$) is 21%. Given that σ_{up} is inversely proportional to ϵ, the error on σ_{up} from this b-tag SF systematic error is a major obstacle. The JES uncertainty is also problematic since a deviation of ± 2 standard deviations from the central value can change the most likely value of the $M_{t\bar{t}}$ spectrum of the resonance by ± 100 GeV. This means that if a resonance were to be observed, there would be a large uncertainty on its mass. This is also problematic when estimating σ_{up} since not only must one exclude an excess around the tested resonance mass, but also around resonance masses centered within ± 100 GeV of this tested mass.

7.4 Other Considerations

This section discusses other aspects of the analysis that were investigated, but did not have a major impact on the analysis.

Note the presence of spikes at the grid point values used in Figures 6.28 and 6.29. For example, Figure 6.28 (c) exhibits a clear excess at $\hat{\hat{\nu}}_{\mathrm{SF}} = 0$ and -1 on top of a smooth distribution, which affects 5% or less of the pseudo-experiments[1]. This could be due to an issue with the minimization which relies on the function's first derivative. A linear interpolation between the grid points ensures that the function is continuous everywhere. However, there is a discontinuity of the first derivative at the grid points which could impact the minimization. It is also possible that the maximum of the likelihood is actually more likely to be at the grid points as an artifact of the linear interpolation. The impact of these spikes on the analysis was studied by performing the same analysis using a grid with less points, $\nu_{\mathrm{SF}} \in \{-2, 0, 2\}$ and $\nu_{\mathrm{JES}} \in \{-2, 0, 2\}$. As expected, the spikes at ν_{SF} = -1, 1 and ν_{JES} = -1, 1 disappeared. The final results for σ_{up} were not significantly changed.

Another consideration of the analysis concerns the generation of the pseudo-experiments. For an assumed model (hypothesis), the frequentist prescription is to simulate experiments under the same conditions as the ones used to collect data. The goal is to recreate the different possible statistical outcome of the "same experiment". However, the notion of "same experiment" is ill defined. For example, the time of data collection or the number of events collected (N) could be fixed for all the pseudo-experiments. It was decided to draw N from a Poisson distribution with expectation value of $n_{\mathrm{b}} + n_{\mathrm{s}}$. This corresponds to pseudo-experiments with the same collection time used. It samples a broader set of "same experiments" than simply considering experiments with a fixed N. Under this choice, the expected σ_{up} is the expected σ_{up} for all the outcomes that could have been observed in the 2010 ATLAS data. It contrasts with fixing N and having the σ_{up} correspond to all the possible outcomes that yield the same amount of data as was observed. The analysis was also performed using this alternative choice and the result did not change significantly. Note that the assumed systematic errors were the same for all the pseudo-experiments: the systematic errors are not associated with statistical fluctuations. They are auxiliary measurements that do not depend on this analysis.

[1] The problem described here has nothing the do with the single peak at 0 for Figures 6.28 (a) and 6.29 (a). The $\hat{\hat{\nu}}_{\mathrm{SF}}$ and $\hat{\hat{\nu}}_{\mathrm{JES}}$ are always zero when $\sigma = 0$ because these systematic errors only affect the signal. When $\sigma = 0$, there is no signal, so the systematic errors have no effect on the fit.

7.5 $M_{t\bar{t}}$ Resonance Models

The difference for the σ_{up} obtained when the M_X and $M_{Z'}$ models are used is small, with the σ_{up} from the M_X model being slightly higher than the one from the $M_{Z'}$ model in general. This is a good indication that the σ_{up} obtained can be interpreted as being approximately model independent. This should hold as long as the resolution of the $M_{t\bar{t}}$ spectrum is larger than the natural width of the resonance. Such case are often referred to as narrow resonances.

The upper limits obtained from the $M_{Z'}$ model are better (smaller) because of the better reconstruction efficiency in the lepton + jets channel, as shown in Figure 6.7. Moreover, the $M_{Z'}$ distributions are reconstructed with more events than the M_X distributions and are therefore less prone to statistical fluctuations. This is especially true for large masses resonances, since there are more events with low $M_{t\bar{t}}$ than high $M_{t\bar{t}}$ in the SM $t\bar{t}$ sample. For example, for the largest resonance mass tested, after all selection cuts, there are 3826 events simulated in the $M_{Z'}$ distribution compared to 367 in the M_X distribution. This is a consequence of the existence of a dedicated MC simulation for a Z′ with $M_{Z'} = 1000$ GeV, while the $M_X = 1000$ GeV distribution is extracted from a sample of $t\bar{t}$ where the $M_{t\bar{t}}$ are drawn following the theoretical $M_{t\bar{t}}$ distribution of the SM. Other differences between the two models is the MC simulation itself. For the M_X model, the simulation is next to leading order and uses a combination of MC@NLO, Herwig and Jimmy. This contrast with the $M_{Z'}$ model which uses Pythia. It is not clear *a priori* how this can affect the result.

7.6 Potential Improvements

Potential analysis improvements are discussed in the following two subsections. The first one considers what can be done with more integrated luminosity, while the second discusses alternative ways the analysis could be done with the same amount of integrated luminosity.

7.6.1 Larger Integrated Luminosity

As the integrated luminosity increases at ATLAS, it will be possible to improve the current analysis in many ways. Requiring that exactly 2 jets in the event are b-tagged would reduce the W+Jets and QCD background and reduce the number of possible

quarks-to-jets associations to two when considering only four jets in the event. In addition, considering more than just the four highest p_{T} jets would now be possible, with 10, 30 and 70 possible combinations when considering the five, six and seven highest p_{T} jets.

Another way the analysis could be improved is by removing events for which the best quarks-to-jets association has a χ^2 larger than a certain value. This option was studied intensively using MC simulations, and it was shown to significantly improve the purity of $\mathrm{t\bar{t}}$ events and the $\mathrm{M_{t\bar{t}}}$ resolution [36] by removing events for which the jets considered do not come from the $\mathrm{t\bar{t}}$ process; such events usually have no combinations with a good χ^2. However, this technique reduces the efficiency and, since the number of $\mathrm{t\bar{t}}$ events collected in 2010 was rather low, it could not be used.

With more integrated luminosity, an exponential function might not adequately represent the background anymore. In this case, more parameters would be needed to describe the background shape which could reduce the ability of the likelihood fit to accurately estimate $\hat{\sigma}$. However, this could be balanced by having more data to fit, and through the two potential improvements described above.

7.6.2 Same Integrated Luminosity

Using 2010 ATLAS data, the present analysis could potentially be improved by abandoning the b-tagging requirement. This would increase the amount of W+Jets and QCD background events, but it would also completely remove the most important systematic error, the b-tag SF. It is not clear *a priori* whether this would improve the analysis results or not. This would require further study.

Smarter ways of selecting the four jets from the $\mathrm{t\bar{t}}$ process, other than simply considering the four highest p_{T} jets of the events, could be investigated. For example, [28] considers an algorithm that relies on the distance between the jets to select the four jets coming from the $\mathrm{t\bar{t}}$ process. The improvements were negligible, but there might be an alternative algorithm that performs better.

7.7 Most Recent Results

Before the publication of this thesis, other $\mathrm{t\bar{t}}$ resonances analyses were performed with more integrated luminosity. ATLAS published results with an integrated luminosity of 200 $\mathrm{pb^{-1}}$, [37] and still no evidences of resonances were found. The σ_{up} obtained

(expected) for a Z′ particle at 95% CL ranges from 38 (20) pb at $M_{Z'} = 500$ GeV to 3.2 (2.2) pb at $M_{Z'} = 1300$ GeV. The CMS experiment published results using an integrated luminosity of 1.14 fb^{-1}, [38]. The σ_{up} obtained (expected) for a Z′ particle at 95% CL ranges from 2.7 (2.7) pb at $M_{Z'} = 1000$ GeV to 0.11 (0.10) pb at $M_{Z'} = 3000$ GeV. The LHC has delivered an integrated luminosity of 5.61 fb^{-1} in 2011. Therefore, if no significant excess of events is found, better limits are expected in the near future.

Chapter 8

Conclusion

In 2010, top-antitop ($t\bar{t}$) pairs were produced in proton-proton collisions at the LHC and collected with the ATLAS detector. The center of mass energy of the collisions was $\sqrt{s} = 7$ TeV, the highest ever achieved in the laboratory. Reconstructing the $t\bar{t}$ invariant mass ($M_{t\bar{t}}$) spectrum therefore provides a new unique opportunity to explore BSM theories in which new particles could be revealed as $t\bar{t}$ resonances.

A χ^2 fitter algorithm was developed to reconstruct $t\bar{t}$ events and was shown to improve the resolution of $M_{t\bar{t}}$. Using this algorithm, the $M_{t\bar{t}}$ spectrum was reconstructed and statistical tests were performed to identify potential resonances. The test statistic was based on an unbinned likelihood ratio, including a nuisance parameter for each source of systematic error considered. A parametrized exponential was used for the shape of the background, while two models of narrow resonances were considered for the shape of the resonances. The first model is a particle with negligible natural width and the same $M_{t\bar{t}}$ resolution and couplings as for the SM $t\bar{t}$. The second model is a Z′ particle. In both cases, no evidence of resonances with a significance of three standard deviations or more was found. The $M_{t\bar{t}}$ spectrum was then analysed to establish an upper limit on the resonance cross section times branching ratio for decaying into $t\bar{t}$ (σ_{up}) at 95% CL as a function of the resonance mass. Both models yielded very similar σ_{up} at 95% CL. The measured (expected) σ_{up} at 95% CL for an integrated luminosity of 35.3 pb^{-1} varies from 3.2 pb ($16.5^{+18.4}_{-9.8}$ pb) at $M_X = 760$ GeV to 22.5 pb ($10.2^{+6.2}_{-5.6}$ pb) at $M_X = 1000$ GeV when no systematic errors are considered and from 3.2 pb ($27.9^{+11.3}_{-19.9}$ pb) to 77.7 pb ($9.8^{+10.7}_{-5.6}$ pb) for the same mass range including systematic errors. Similarly, σ_{up} at 95% CL varies from 2.9 pb ($16.7^{+10.7}_{-10.0}$ pb) at $M_{Z'} = 700$ GeV to 19.4 pb ($8.8^{+5.3}_{-5.0}$ pb) at $M_{Z'} = 1000$ GeV without systematic errors and from 2.9 pb ($55.9^{+56.9}_{-47.0}$ pb) to 43.4 pb ($7.8^{+8.9}_{-4.7}$ pb) for

the same mass range including systematic errors. The difference between the measured and expected σ_{up} is large, but the measured σ_{up} falls within the expected σ_{up} 95% coverage band in general. The similar results for the different models suggest that the σ_{up} result may be valid for other models of narrow resonances. The results obtained were compared to those obtained in another ATLAS analysis on the same data set. Despite using different approaches in extracting σ_{up}, both analyses agree within their error coverage band.

Bibliography

[1] MissMJ, "Standard model of elementary particles: the 12 fundamental fermions and 4 fundamental bosons." http://en.wikipedia.org/wiki/File:Standard_Model_of_Elementary_Particles.svg.

[2] F. Buisseret and C. Semay, "Effective potential between two gluons from lattice QCD," *Eur.Phys.J.*, vol. A33, pp. 87–93, 2007.

[3] W.-M. Yao *et al*, "Review of Particle Physics," *Journal of Physics G*, vol. 33, pp. 1+, 2006.

[4] E. Eichten, I. Hinchliffe, K. Lane, and C. Quigg, "Supercollider physics," *Rev. Mod. Phys.*, vol. 56, pp. 579–707, Oct 1984.

[5] A. Heinson, "Useful diagrams of top signals and backgrounds." http://www-d0.fnal.gov/Run2Physics/top/top_public_web_pages/top_feynman_diagrams.html.

[6] "Measurement of the t-channel single top-quark production cross section in 0.70 fb^{-1} of pp collisions at sqrt(s) = 7 tev with the atlas detector," Tech. Rep. ATLAS-CONF-2011-101, CERN, Geneva, Jul 2011.

[7] "Measurement of the top quark pair production cross section in pp collisions at $\sqrt{s} = 7$ tev in dilepton final states with atlas," Tech. Rep. arXiv:1108.3699. CERN-PH-EP-2011-103, CERN, Geneva, Aug 2011.

[8] A. Quadt, "Top quark physics at hadron colliders," *European Physical Journal C*, vol. 48, pp. 835–1000, Dec. 2006.

[9] "Measurement of $t\bar{t}$ production in the all-hadronic channel in 1.02 fb^{-1} of pp collisions at $\sqrt{s} = 7$ tev with the atlas detector," Tech. Rep. ATLAS-CONF-2011-140, CERN, Geneva, Sep 2011.

[10] R. Frederix and F. Maltoni, "Top pair invariant mass distribution: a window on new physics," *JHEP*, vol. 01, p. 047, 2009.

[11] R. M. Harris, C. T. Hill, and S. J. Parke, "Cross Section for Topcolor Z' decaying to top-antitop," *ArXiv High Energy Physics - Phenomenology e-prints*, Nov. 1999.

[12] B. Lillie, L. Randall, and L. Wang, "The Bulk RS KK-gluon at the LHC," *Journal of High Energy Physics*, vol. 9, pp. 74–+, Sept. 2007.

[13] L. Fitzpatrick, J. Kaplan, L. Randall, and L. Wang, "Searching for the Kaluza-Klein graviton in bulk RS models," *Journal of High Energy Physics*, vol. 9, pp. 13–+, Sept. 2007.

[14] H.-L. Lai *et al.*, "New parton distributions for collider physics," *Phys. Rev.*, vol. D82, p. 074024, 2010.

[15] ATLAS Collaboration, "The ATLAS Experiment at the CERN Large Hadron Collider," *J. Instrum.*, vol. 3, p. S08003, 2008.

[16] G. Aad *et al.*, "Expected Performance of the ATLAS Experiment - Detector, Trigger and Physics," 2009.

[17] M. Cacciari, G. P. Salam, and G. Soyez, "The Anti-k(t) jet clustering algorithm," *JHEP*, vol. 0804, p. 063, 2008.

[18] "Prospects for top anti-top resonance searches using early atlas data.," Tech. Rep. ATL-PHYS-PUB-2010-008, CERN, Geneva, Jul 2010.

[19] G. Aad *et al.*, "Performance of Missing Transverse Momentum Reconstruction in Proton-Proton Collisions at 7 TeV with ATLAS," 2011.

[20] G. Brooijmans, A. Gaponenko, N. Ghodbane, G. Salamanna, and I. Van Vulpen, "Design considerations for the top reconstruction output edm classes," Tech. Rep. ATL-COM-SOFT-2009-006, CERN, Geneva, May 2009. Private communication.

[21] F. James, "Minuit, function minimization and error analysis." http://wwwasdoc.web.cern.ch/wwwasdoc/minuit/minmain.html.

[22] R. Brun, "Root — a data analysis framework." http://root.cern.ch/drupal/.

[23] S. Frixione and B. R. Webber, "The MC@NLO 3.4 Event Generator," 2008.

[24] S. Gieseke *et al.*, "Herwig++ 2.5 Release Note," 2011.

[25] J. M. Butterworth, J. R. Forshaw, and M. H. Seymour, "Multiparton interactions in photoproduction at HERA," *Z. Phys.*, vol. C72, pp. 637–646, 1996.

[26] T. Sjostrand, S. Mrenna, and P. Z. Skands, "PYTHIA 6.4 Physics and Manual," *JHEP*, vol. 05, p. 026, 2006.

[27] M. L. Mangano, M. Moretti, F. Piccinini, R. Pittau, and A. D. Polosa, "ALPGEN, a generator for hard multiparton processes in hadronic collisions," *JHEP*, vol. 07, p. 001, 2003.

[28] "A search for new high-mass phenomena producing top quarks with the atlas experiment," Tech. Rep. ATLAS-CONF-2011-070, CERN, Geneva, May 2011.

[29] S. Agostinelli *et al.*, "GEANT4: A simulation toolkit," *Nucl. Instrum. Meth.*, vol. A506, pp. 250–303, 2003.

[30] https://twiki.cern.ch/twiki/bin/view/AtlasProtected/TopCommonObjects2010. ATLAS restricted.

[31] J. Friedman, "353QH twice smoothing algorithm," Aug 1974. Presented in Proc. of the 1974 CERN School of Computing, Norway.

[32] B. Chapleau, J.-R. Lessard, and M. Vos, "Identify the topology of semileptonic top-antitop events," Tech. Rep. ATL-COM-PHYS-2010-066, CERN, Geneva, Feb 2010. Private communication.

[33] C. J. Clopper and E. S. Pearson, "The use of confidence or fiducial limits illustrated in the case of the binomial," *Biometrika*, vol. 26, p. 404, 1934.

[34] G. Cowan, K. Cranmer, E. Gross, and O. Vitells, "Asymptotic formulae for likelihood-based tests of new physics," *European Physical Journal C*, vol. 71, p. 1554, Feb. 2011.

[35] "Updated luminosity determination in pp collisions at root(s)=7 tev using the atlas detector," Tech. Rep. ATLAS-CONF-2011-011, CERN, Geneva, Mar 2011.

[36] J.-R. Lessard and M. Lefebvre, "Search for narrow resonances (pp $\rightarrow$ x $\rightarrow$ ttbar) in the context of early atlas data," Tech. Rep. ATL-COM-PHYS-2008-099, CERN, Geneva, Jul 2008. Private communication.

[37] "A search for $t\bar{t}$ resonances in the lepton plus jets channel in 200 pb^{-1} of pp collisions at $\sqrt{s} = 7$ tev," Tech. Rep. ATLAS-CONF-2011-087, CERN, Geneva, Jun 2011.

[38] "Search for heavy narrow resonances decaying to ttbar in the muon+jets channel," Tech. Rep. CMS-PAS-EXO-11-055, CERN, Geneva, 2011.

Acronyms

AOD Analysis Object Data. 26, 27

ATLAS A Toroidal LHC ApparatuS. 17, 19, 21, 23, 25–28, 30, 32, 33, 37, 39, 43, 45, 47, 50–52, 54, 68, 88, 95, 96, 99–101, 103, 104

BSM Beyond the Standard Model. 1, 9, 13, 19, 32, 103

CERN European Organization for Nuclear Research. 27

CL Confidence Level. 78, 80, 82–85, 89, 92–96, 102, 103

COOL LCG conditions database product. 27, 35

CP Combined Performance. 27, 35, 36, 112

DQ Data Quality. 35–37, 39, 40, 112, 131, 134, 135

EDM Event Data Model. 47

EM ElectroMagnetic. 4–8, 19–21, 23, 24, 28, 31, 131, 132, 137

ESD Event Summary Data. 26, 27

EW ElectroWeak. 1, 8, 9, 19

GRL Good Run List. 35, 39, 40, 50, 53, 134

ID Inner Detector. 19–21, 29, 31, 40, 41

JER Jet Energy Resolution. 30, 86

JES Jet Energy Scale. 31, 86, 88, 98

LAr Liquid Argon. 19, 21, 23, 40, 131

LHC Large Hadron Collider. 1, 16, 17, 19, 39, 51, 102, 103

MC Monte Carlo. 27, 31, 32, 50–54, 56, 58, 63, 68–70, 74, 75, 86, 96, 100, 101

MIP Minimum Ionization Particle. 29

pdf probability density function. 43, 45, 46, 74, 88

QCD Quantum ChromoDynamics. 6, 7, 11, 12, 17, 51, 53, 70, 71, 73, 100, 101

QED Quantum ElectroDynamics. 4–7

RDO Raw Data Object. 26, 27

SF Scale Factor. 32, 86, 88, 98, 101

SM Standard Model. 1, 3, 6, 8, 9, 13, 32, 50, 51, 54–56, 58, 59, 62, 68, 74, 100, 103

Appendix A

Jet Data Quality

This appendix describes the structure of the jet monitoring software, and the histograms and algorithms used to identify defects. There is also a section on the jet cleaning cuts.

A.1 Overview of the Jet Monitoring Software

There are four main jet directories used in the jet monitoring. Each of them contains the same histograms, but for different type of jets:

- **AntiKt4TopoJets**: This directory has the highest statistics but is sensitive to changes in trigger pre-scales and low-level noise. Automatic checks cannot be relied upon.
- **AntiKt4TopoJets_pt20**: This directory contains only jets with $p_T > 20$ GeV. It is still sensitive to changes in pre-scales, but is useful to isolate trigger effects, as the dependency on low level noise bursts is reduced due to the p_{T} cut.
- **AntiKt4TopoJets_EF_j30**: This directory contains all jets in events passing the EF_j30 trigger[1] are monitored. Automatic checks are more reliable, but they can still be biased by noisy calorimeter cells.
- **AntiKt4TopoJets_EF_j30_pt20**: This directory contains only jets with $p_T > 20$ GeV in events passing the EF_j30 trigger are monitored. This is the

[1]The label EF_j30 refers to a jet at the event filter, *trigger jet*, with p_{T} greater than 30 GeV. The exact trigger may change with time depending on the express stream trigger menu.

most robust group to changes in conditions and run-to-run variations. It is used as the *default* to check problems. Automatic checks in this directory can generally be trusted.

These top level jet directories are sub-divided by themes under a directory called *Details*. For each of these themes, one or two histograms are duplicated and put in a *Summary* directory. There is an extra directory, *NotClean*, which has the same structure outlined below which contains all the jets, whereas the jets in the *Details* directory have passed the standard jet CP loose cleaning cuts. See section A.4 for details about jets cleaning cuts. The histograms after cleaning cuts are used to set the flags and defects for the run. The one before cleaning cuts are used to spot specific calorimeter problems in order to report back to the sub-detectors. An overview of the directory structure can be seen in Figure A.1.

Figure A.1: Data Quality jet directories structure, as seen on the DQ web display.

The aim of the *Summary* directory is to provide an initial overview. However, the DQ assessment should be based on the histograms within the *Details* directory. In the AntiKt4TopoJets_EFj30_pt20 directory, there are also three additional sub-directories, JetB, JetEA and JetEC, with identical *Details* and *Summary* sections. The jet histograms are split into the barrel and the two end-cap regions for each of these sub-directories. They further help localize problem areas in specific calorimeter

sub-detectors. It is sufficient to start with the distributions of all the detector regions and then look at the different regions if needed. There is also the FailDQQual summary page within AntiKt4TopoJets_EF_j30_pt20. This is simply a small set of summary histograms for events that did not pass jet cleaning cuts. The current *Details* directories are the following:

- *Calibration* - contains histograms relating to jet calibration,
- *EnergyByLayers* - contains histograms relating to the subdivision of the jet energy via calorimeter layers,
- *EtaPhi* - contains histograms of jet related quantities binned by $\eta - \phi$ of the jet,
- *JetShapes* - contains histograms related to the sub-structure of the jet,
- *Kinematics* - contains histograms of jet kinematics, inclusive and also averaged by η and ϕ,
- *LB* - contains histograms tracking jet quantities vs luminosity block number and vs number of vertices in the event,
- *LeadingJet* - contains histograms limited to the leading and sub-leading jets.

A.2 Jet Data Quality Histograms

Below is the list of the plots in the Summary directory. The arrow indicate in which of the Details sub-directory the plot is duplicated.

- Jet E_T in $\eta - \phi \rightarrow$ EtaPhi.
- Ave Fraction of jet E per calorimeter layer $\rightarrow$ EnergyByLayers.
- Fraction p_T vs fraction constituents (N) (average over all jets) $\rightarrow$ JetShapes.
- Jet Fraction energy from the EM calorimeter $\rightarrow$ EnergyByLayers.
- JetEtaAsymmetry $\rightarrow$ Kinematics.
- Jet η and $\phi \rightarrow$ EtaPhi.

- Number of constituents/jet $\rightarrow$ JetShapes.
- Jet p_T $\rightarrow$ Kinematics.
- Jet Quality in $\eta - \phi$ $\rightarrow$ EnergyByLayers.
- Number of Jets $\rightarrow$ Kinematics.

A.2.1 Calibration

Figure A.2 shows the calibration plots. The calibration monitors the difference between the three possible scales of the jet energy: EM scale (Raw), constituent state (CS) and calibrated (Cal or Final). A jet at the EM scale corresponds to the jet energy when no calibration is applied. A jet at constituent state has its energy calculated using the calibrated constituents (ex. topoclusters). The calibrated state corresponds to the jet after an extra calibration is applied, H1 for example. **The jets are by default in the EM state unless stated.** This may be changed when the hadronic calibration of jets is judged sufficiently robust.

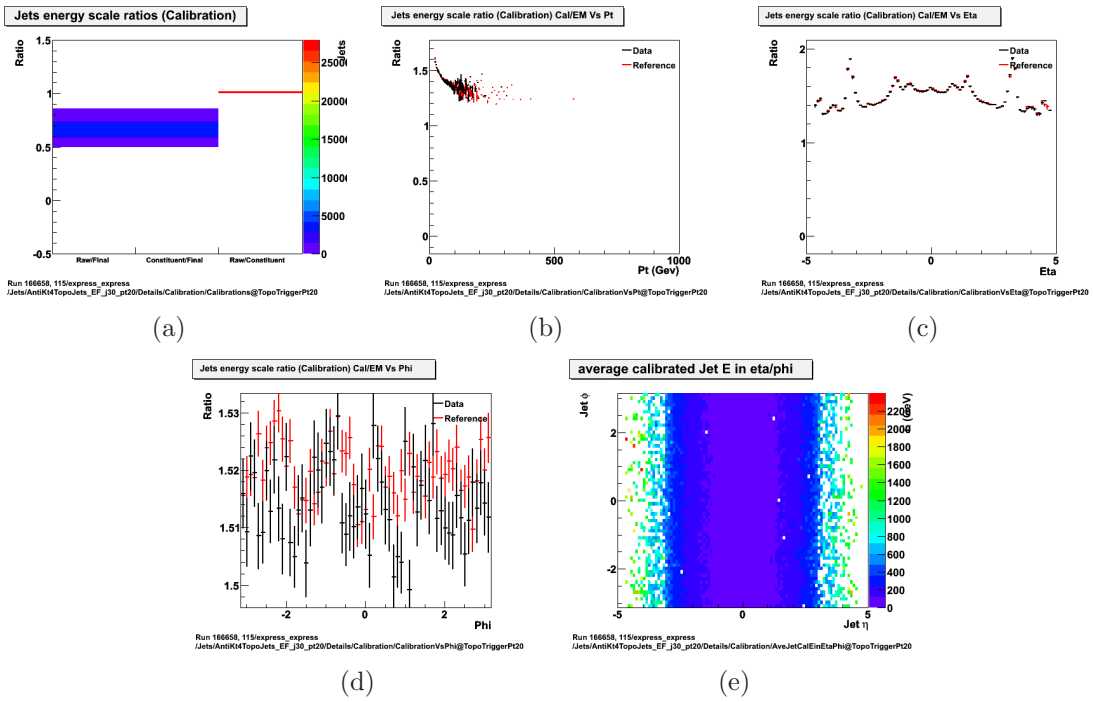

(a) (b) (c)

(d) (e)

Figure A.2: Calibration plots. See text.

The plots in this directory are the following:

A.2a). Jets energy scale ratios plot shows the jet energy ratio between all the different jet energy states. The topocluster are not yet calibrated, so Raw/Constituent should read 1 while Raw/Final and Constituent/Final should be equal to each other and smaller than 1.

A.2b)-d). Jet energy scale ratio Cal/EM vs Pt, Eta and Phi. It should be flat in phi. Low p_{T} jets should have a larger value for Cal/EM.

A.2e). Average calibrated Jet E in eta/phi. Since by default we monitor EM scale jets, this plots highlights differences calibration for specific $\eta - \phi$ regions.

A.2.2 EnergyByLayers

This sub-directory contains plots of the fraction of energy deposited by each jet in the different calorimeter layers. There are three summary plots, Figures A.3b), A.6b) and A.4, in which the mean and spread per individual layer is displayed.

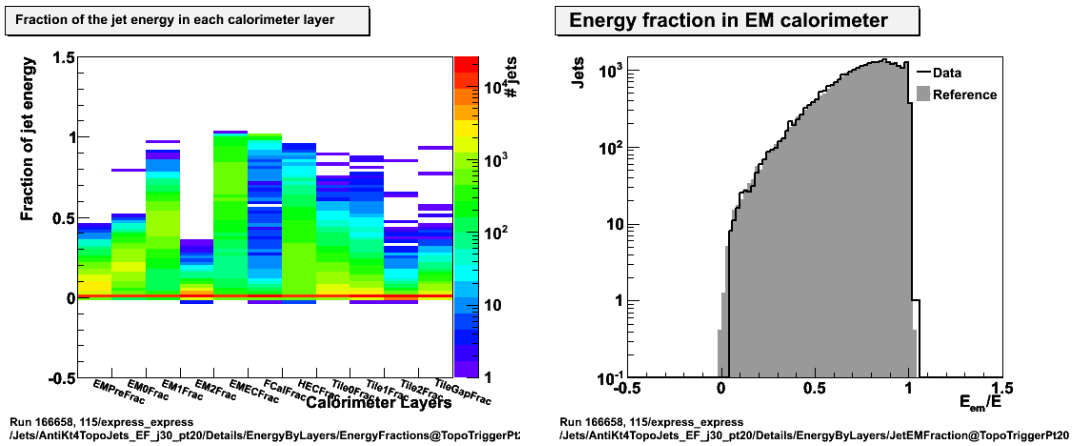

(a) (b)

Figure A.3: Energy by layers summary plots. See text.

The plots are the following:

A.3a). Fraction of the jet energy in each calorimeter layer plot summarizes the energy fraction in all the calorimeter layers. Unfortunately, it can be sometimes hard to compare from run to run.

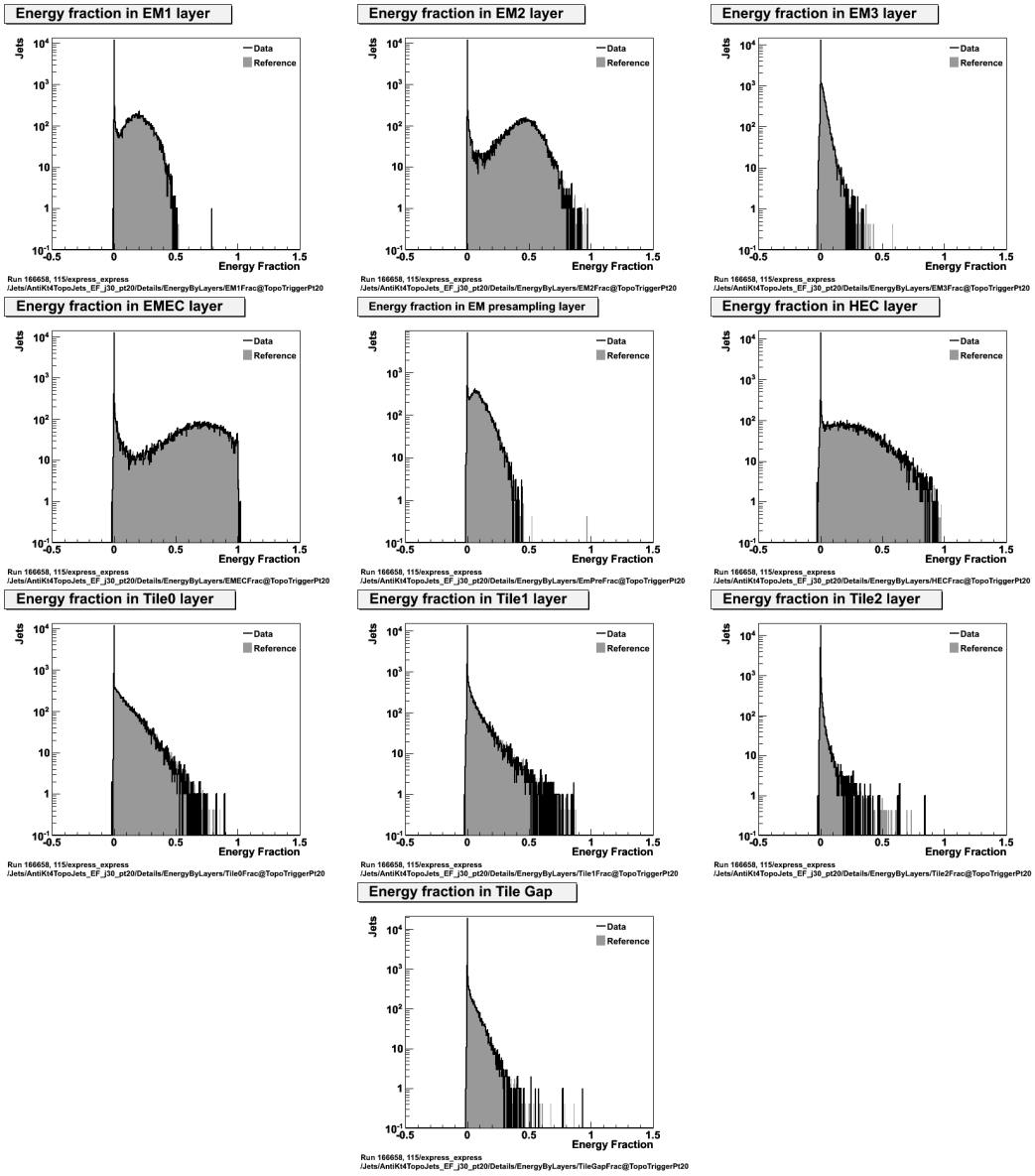

Figure A.4: Energy by layers plots. See text.

A.3b). Energy fraction in EM calorimeter. Fraction of the jet energy deposited in the EM calorimeter (jet EM energy / jet Total energy). It can often give a quick indication of whether a problem comes from LAr or Tile detector. A continuous distribution for EM Fraction is expected.

A.4. Energy fraction in layer X with X running over all the layers of the calorimeter. These plots can be used to track differences from run to run for a

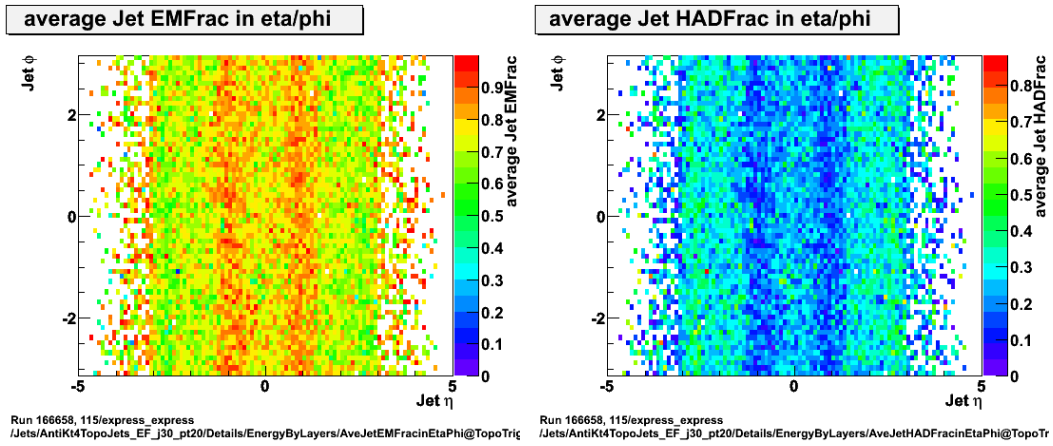

Figure A.5: Mean fraction of energy in EM and HAD calorimeters vs $\eta - \phi$. See text.

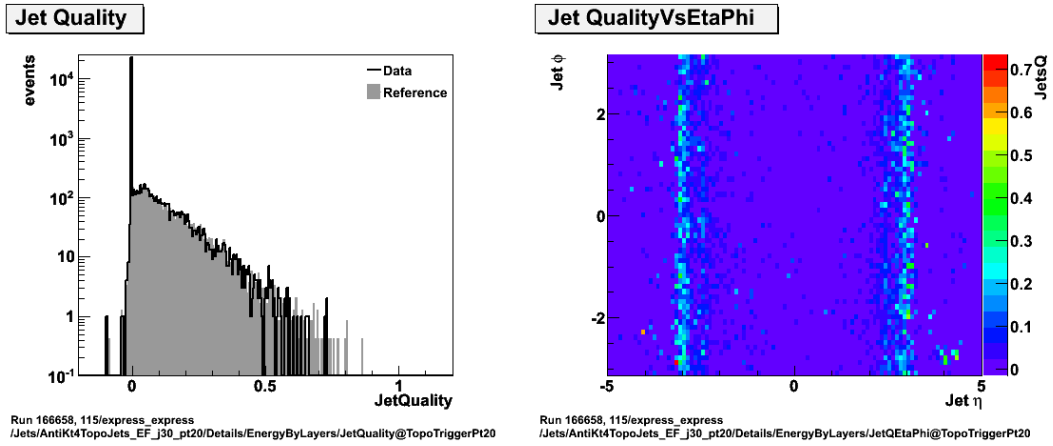

(a) (b)

Figure A.6: a) Jet Quality over all jets and b) average Jet Quality in $\eta - \phi$.

given layer. The shape will vary for each layer, so the only way to know what to expect is to compare to a "good" run.

A.5. Mean of EM and HAD fractions in $\eta - \phi$ bins. Plots display average EM and Hadronic energy over the calorimeter. These plots are useful to see if any excess in layer fractions is related to a particular cell in $\eta - \phi$ or if the discrepancy is spread over the whole calorimeter.

A.6. Jet Quality. Plots showing the jet quality quantity. For a description of the jet quality variable, please refer to section A.4. a) is simply a plot of jet

quality over all jets whereas b) displays the average jet quality as a function of η and ϕ. This plot is useful to spot whether a particular $\eta - \phi$ region is continuously resulting in bad quality jets.

A.2.3 EtaPhi

This directory shows various quantities binned in $\eta - \phi$. There is one entry per jet. There are two summary plots, Figures A.7a) and c).

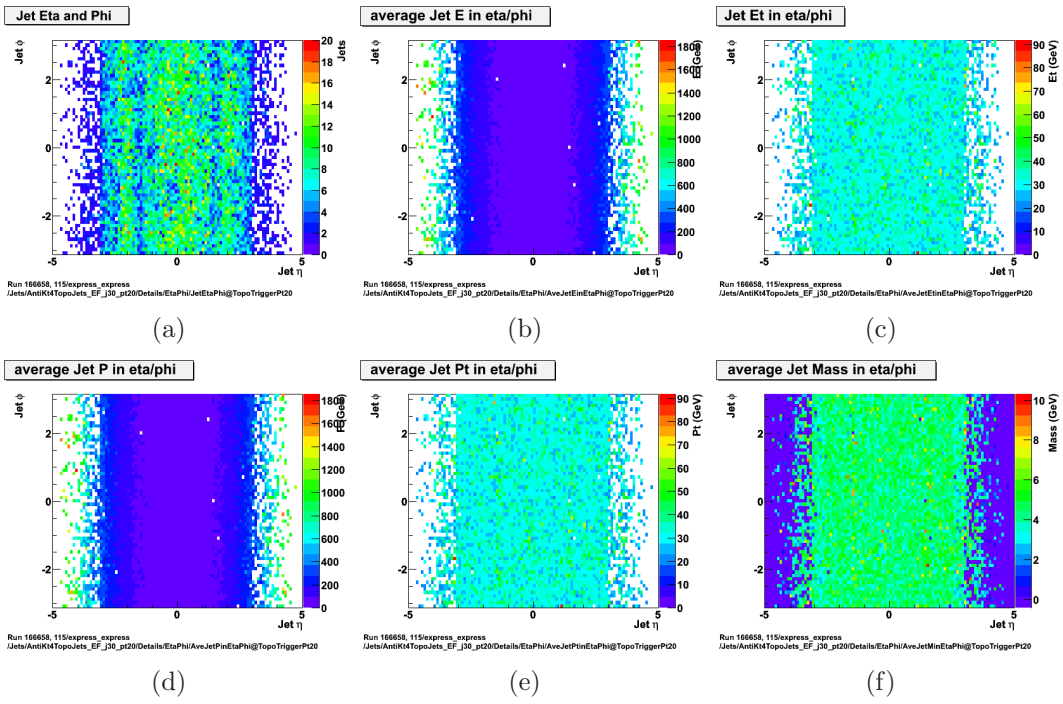

(a) (b) (c)

(d) (e) (f)

Figure A.7: a) Number of Jets in $\eta - \phi$. b)-f) Average "observable" in $\eta - \phi$.

The plots are the following:

A.7a). Jet $\eta - \phi$. Total number of jets for a given run in bins of $\eta - \phi$. Excess of jets in a given region is reported as a hot region. Note that there are a number of holes in the detector due to missing FEBs and optical links. These are partially compensated for by offline software corrections.

A.7b)-f). Average "observable" in $\eta - \phi$. The monitored observables in $\eta - \phi$ are energy, transverse energy, momentum, transverse momentum and mass of the jet. It shows the average of the observable over all jets passing the relevant directory cuts.

A.2.4 JetShapes

This sub-directory contains different plots of the jets constituents (topoclusters). There is one entry for each constituent of a jet. There are two summary plots, Figures A.8a) and A.10e).

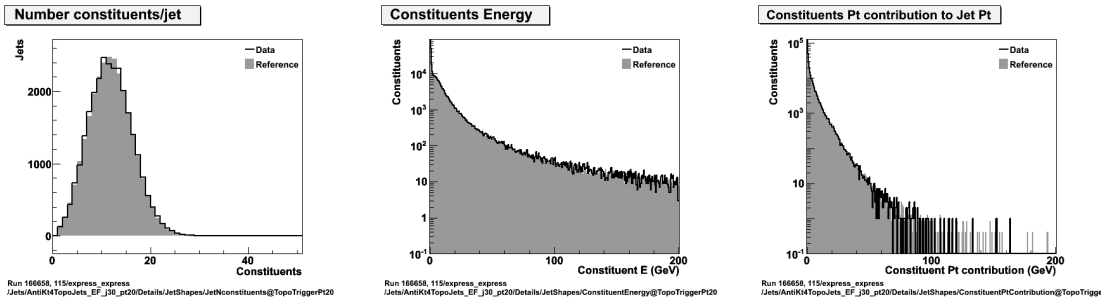

(a) (b) (c)

Figure A.8: Constituents distribution plots. See text.

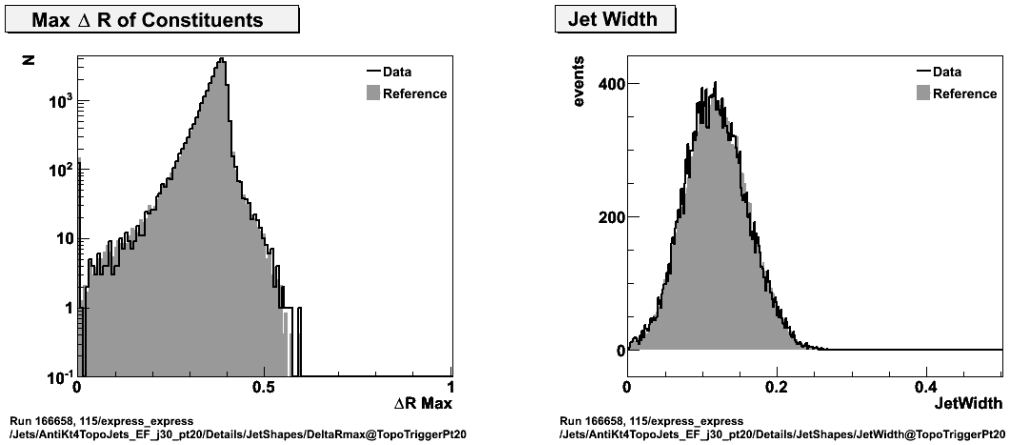

(a) (b)

Figure A.9: Size of the jets plots. See text.

The plots are the following:

A.8a). Number of Constituents per Jet. There should not be a large increase or decrease in the average from run to run.

A.8b). Constituents Energy and c) Constituents p_{T} Contribution of Jet p_{T} over all constituents of all jets. The quantity "constituents p_{T} contribution of Jet p_{T}" refers to the amount of p_{T} a particular constituent adds to

the p_{T} of the jet. The sum of all "constituents p_{T} contribution of Jet p_{T}" sums adds to the total p_{T} of the jet.

A.9a). Max ΔR of Constituents plot shows the distance in R space of the constituent that is the furthest from the jet-axis. No constituent should be much further than the "R-size" parameter of the jet. So for example, in the case of Anti-k_{T} 4 jets, it would be acceptable to have the furthest constituent at 0.5 or 0.6, but past that, it is flagged.

A.9b). Jet Width shows the calculated width of the jet, which is an energy weighted distance of the constituents to the jet axis. That should be smaller or equal to the "R-size" parameter of the jet collection monitored.

For the following "shape" plots, the plots are duplicated under a profile version and a 2D plot version. For the 2D plots, there is one entry per constituent. From the 2D plot, a profile plot is made. In both case, all the constituents from all the jets passing directory cuts are considered.

A.10a). Constituent (N) Integral plots show the integrated number of jet constituents divided by the total number of constituents in the jet, as a function of the distance from the jet axis. The jets are expected to have most of the constituents within a ΔR corresponding to their "R-size". Moreover, the curve should approach unity at the jet "R-size".

A.10b). Constituent (N) Profile plots show the number of constituents between r (the distance from the jet axis) and r+δr, as a function of r, where δr is the binning size. Plots b) are the derivatives with respect to r of plots a). Again there shouldn't be a large number of constituents at a distance larger than "R-size" from the jet axis.

A.10c). Integrated Jet Profile plots show the integrated p_{T} of the constituents divided by the jet p_{T} as a function of the constituent distance from the jet axis. Again it is expected that most of the integrated p_{T} is within the jet "R-size". In other words, 1 should be reached when r is equal to the jet "R-size".

A.10d). Normalized Jet profile plots show the p_{T} fraction of the jet constituents between r and r+δr, as a function of the distance from the jet axis.

Plots d) are the derivatives with respect to r of plots c). Most of the jet energy should come from the center of the jet.

A.10e). Fraction p_T vs Fraction Constituents (N) plots show the integrated p_T of the constituents divided by the jet p_T, vs integrated number of jet constituents divided by the total number of constituents, as the distance from the jet axis increases. Starting from the jet center, these plots show what fraction of jet p_T is given by a certain fraction of jet constituents. The curve should start at (0,0) and end at (1,1) and all the points should be above the x=y line, as one expects the main contribution coming from the constituents nearest to the jet axis.

A.2.5 Kinematics

In this section, the following jets kinematic quantities are monitored: energy (E), transverse energy (E_T), momentum (p), transverse momentum (p_T) and mass. For each of these quantities, 3 plots are generated: one for the distribution, and two profile histograms, one vs eta and one vs phi. There are also four plots related to vector and scalar sums. There are two additional plots. One is the number of jets per event (over all the events of the run) and the other is the jet eta asymmetry, described later. There are three summary plots, Figures A.11, A.15a) and b).

The plots are the following:

A.11. E, E_T, p, p_T and mass distributions. All these distributions should be "exponential decay" like, with possible small shoulders due to trigger turn-on effects.

A.12. Average E, E_T, p, p_T and mass vs phi. The average should be flat as function of phi

A.13. Average E, E_T, p, p_T and mass vs eta. The average should be symmetric around 0.

A.14a). Jets E and E_T scalar sum plots show the scalar sum (over all the jets in each event) of E and E_T. There is therefore one entry by event.

A.14b). Jets energy vector sum (and phi). The energy vector sum is obtained from adding the E_T vector over all the jets passing directory cuts in each event. There is therefore one entry per event.

A.15a). **Number of Jets**. Histogram of the number of jets per event over the run period.

A.15b). **Jet Eta Asymmetry**. A profile histogram for which an entry of +1 is entered if the jet η is positive and -1 if it is negative, vs the $|\eta|$ of the jet. All the jets of the run are considered. A flat line at 0 should be observed with some small fluctuations. Two similar plots are present one with the raw asymmetry and one normalized to the total number of jets per η bin. The fractional plot should vary within a 5-10% envelope.

A.2.6 LB

This directory contains the jet plots vs luminosity block number and vs number of vertices. Currently, eight plots are included: the average jet E, Et, sum Et, and average number of jets, as a function of both luminosity number, A.16 and number of vertices, A.17.

A.2.7 LeadingJet

This directory contains plots relating to the leading jet properties (ϕ, η, p_{T} and $\eta-\phi$) in all the events of the run. The leading (hardest) jet is the jet in the event with the highest p_{T}. A few plots also show the comparison between the leading and the next-to-leading jet (if present). For all these plots, there is one entry per event.

The plots are the following:

A.18a). **Leading Jet** p_{T} plot shows the momentum of the leading jet in the event.

A.18b)-d). **Leading Jet in eta-phi, eta and phi** plots show where the leading jet in each event is pointing.

A.19a). **Two hardest Jets** p_{T} **difference /** p_{T} **leading Jet.**

A.19b)-d). **Two hardest Jets (R, Eta and Phi) Distance** For di-jet events, the jets are expected to be back to back: $\Delta\phi = \pm\pi$, $\Delta\eta = 0$ and $\Delta R = \pi$.

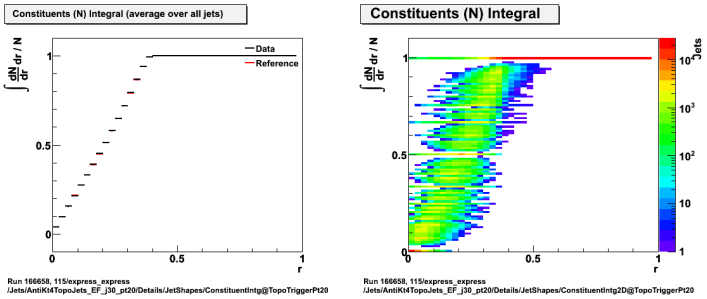

(a)

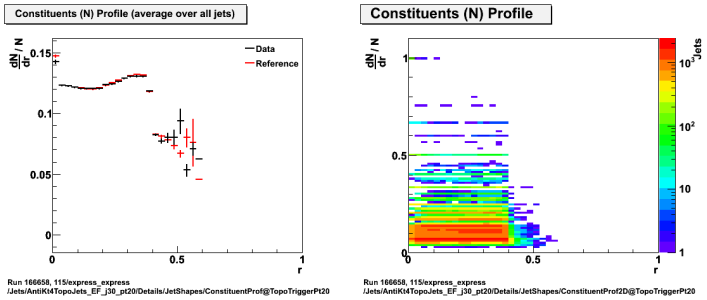

(b)

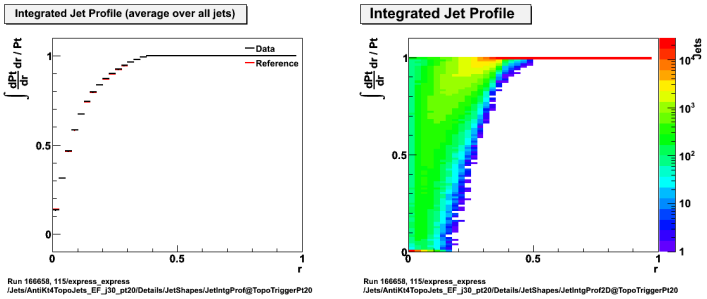

(c)

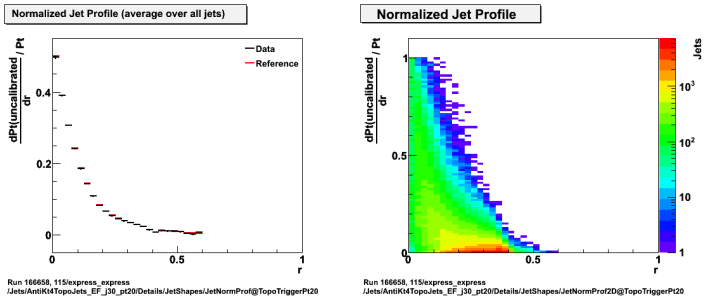

(d)

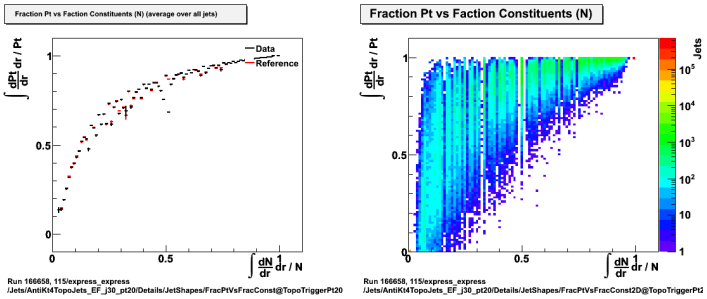

(e)

Figure A.10: The jets shape plots. See text.

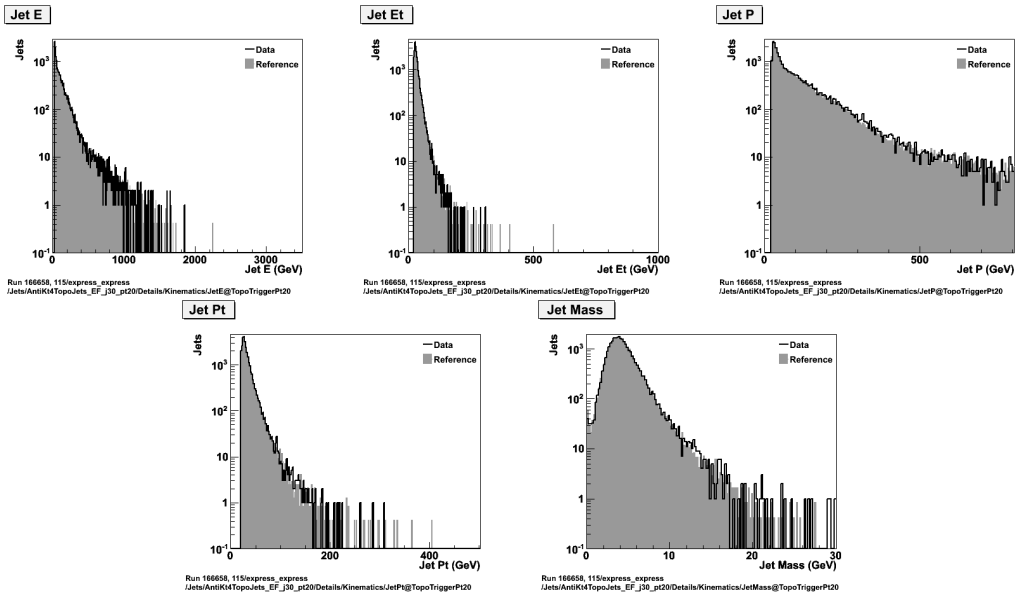

Figure A.11: E, E_T, p, p_T and mass distributions. See text.

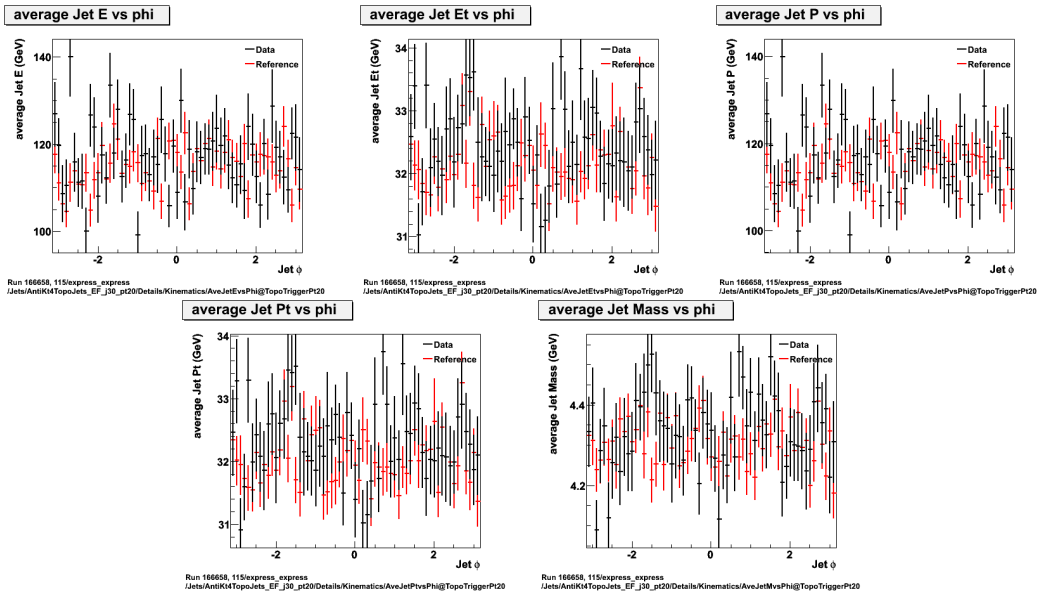

Figure A.12: Average E, E_T, p, p_T and mass vs phi. See text.

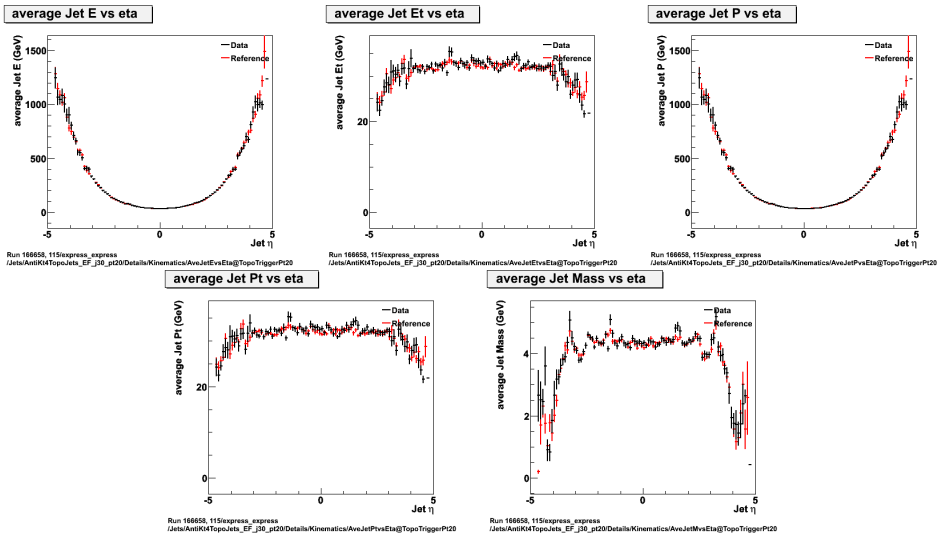

Figure A.13: Average E, E_T, p, p_T and mass vs eta. See text.

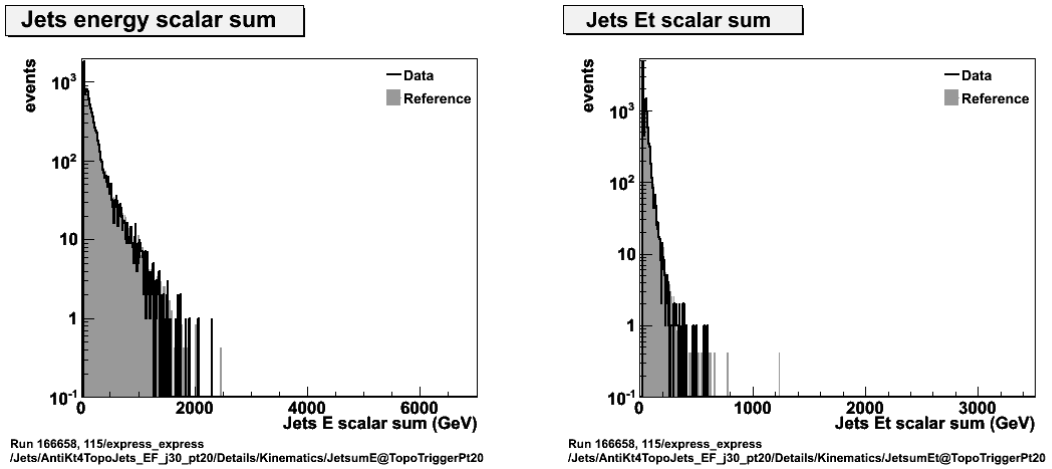

(a)

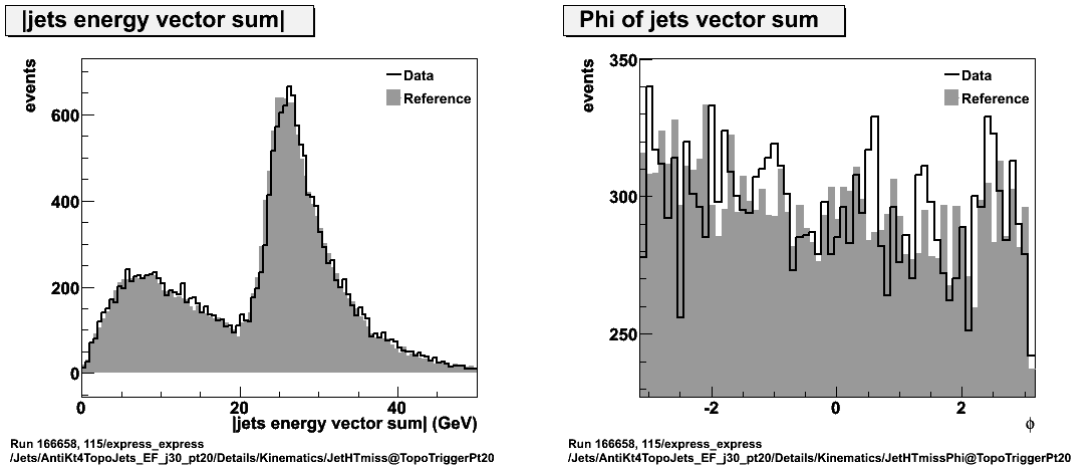

(b)

Figure A.14: The vector and scalar sum plots. See text.

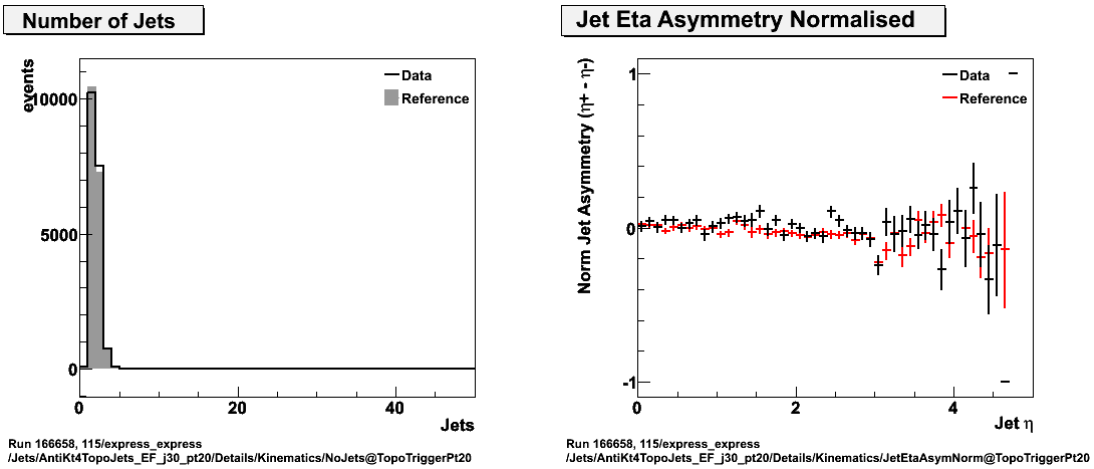

(a) (b)

Figure A.15: Number of Jets and Jet Asymmetry plots. See text.

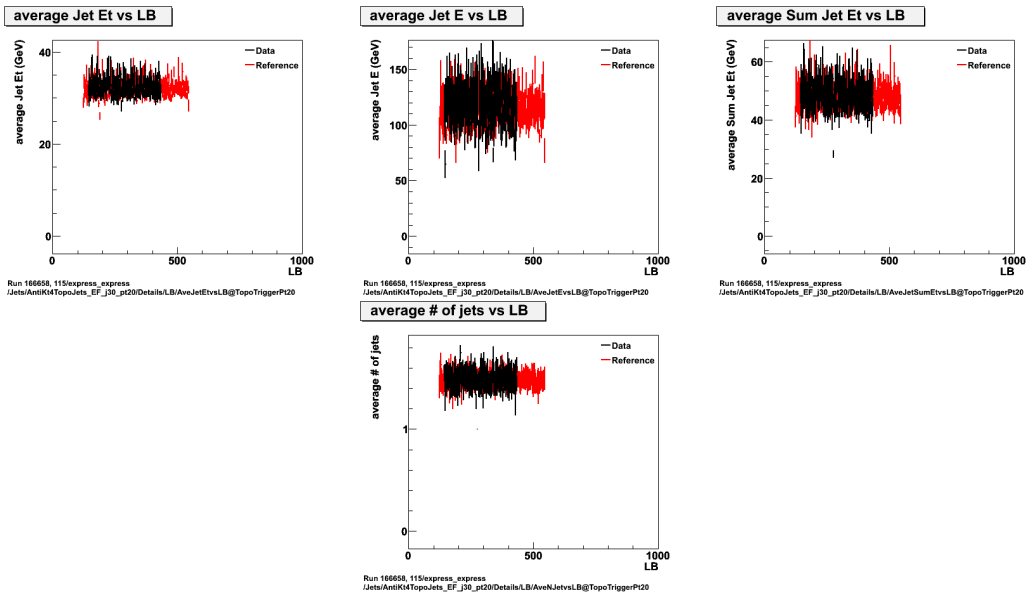

Figure A.16: Plots of average jet E_T, E, sum E_T, and number of jets as a function of luminosity block.

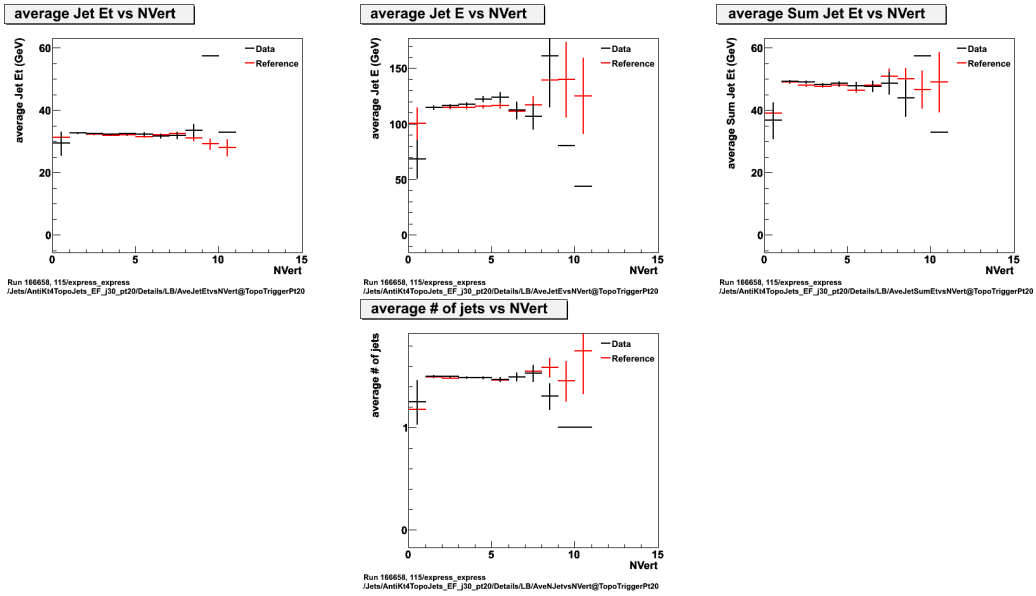

Figure A.17: Plots of average jet E_T, E, sum E_T, and number of jets as a function of the number of vertices.

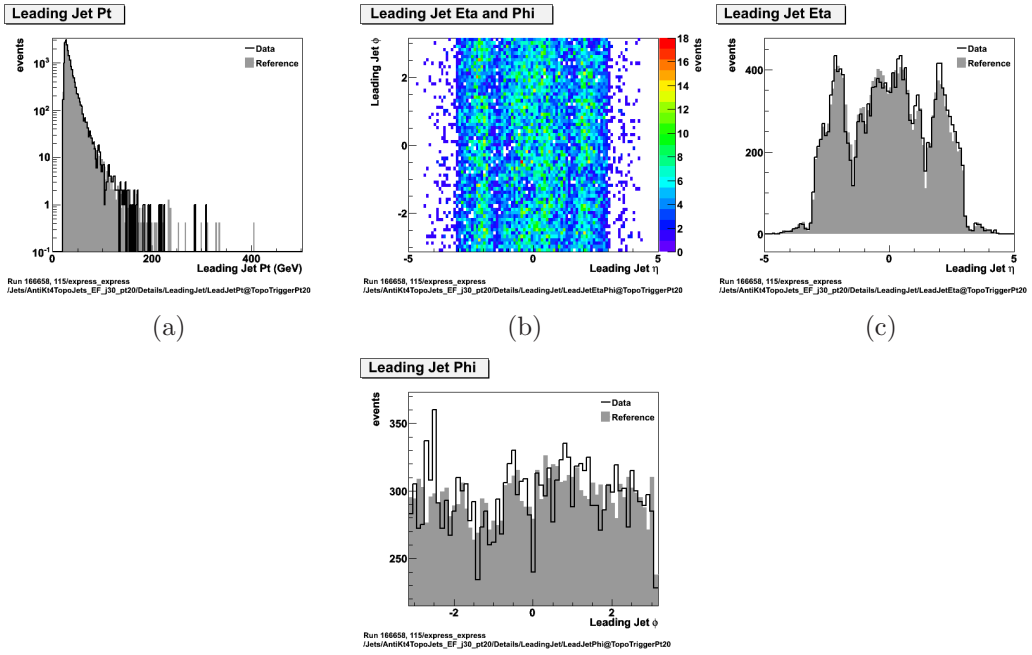

(a) (b) (c)

(d)

Figure A.18: Leading jet plots. See text.

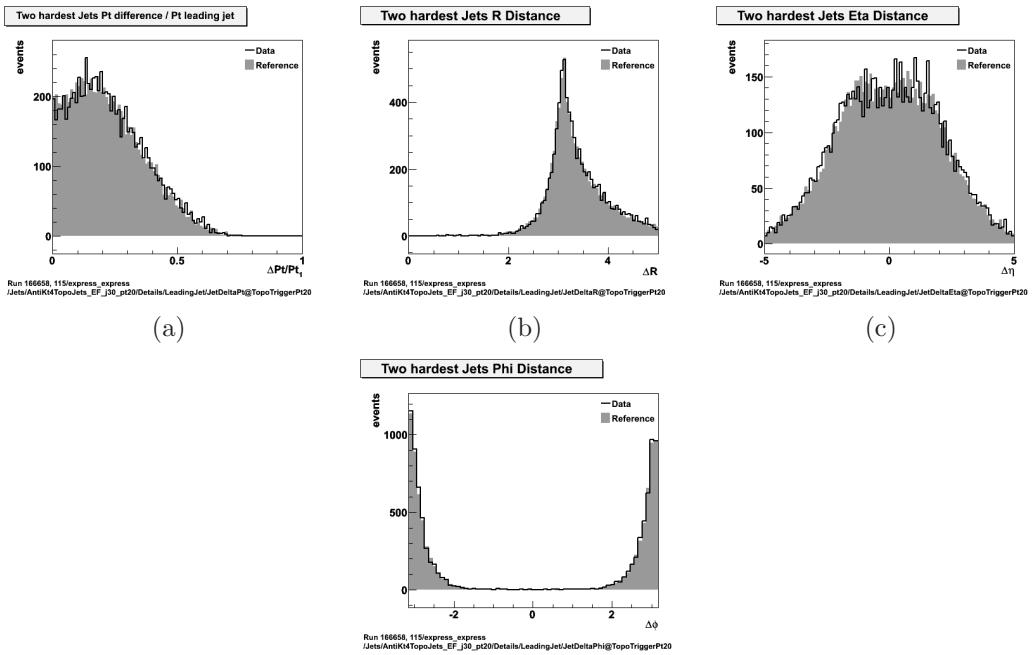

(a) (b) (c)

(d)

Figure A.19: Comparison of the two leading jets. See text.

A.3 Jet Data Quality Algorithms

There are four main automatic check algorithms used to identify problems in the jet observables distributions:

- *One Dimensional χ^2 Algorithm.* The one-dimensional χ^2 algorithm is a simple algorithm which calculates the χ^2 per degree of freedom between an histograms and its reference. This is done by first scaling the reference histogram to the same number of entries as the given histogram. This algorithm is applied to almost every one-dimensional histograms. Thresholds for GREEN are about 3 and thresholds of RED are 4 or 5.

- *Scatter χ^2 Algorithm.* The scatter χ^2 algorithm is based loosely on the one dimensional χ^2 algorithm. For input profile (scatter) histogram p and reference profile histogram r, the χ^2 is calculated by calculating the following:

$$\chi^2 = \frac{1}{\text{NDF}} \sum_i \frac{(y_{p,i} - y_{r,i})^2}{\sigma^2_{y_{p,i}} + \sigma^2_{y_{r,i}}}, \tag{A.1}$$

  where $y_{x,i}$ is the value of the contents in bin i, with error $\sigma_{y_{x,i}}$. This algorithm is applied to almost all profile histograms. Thresholds are often 3 for GREEN and 4 for RED. Unfortunately this algorithm is not always reliable. When dealing with a profile histogram, each bin i shows the average of all the entry values in that bin. The error $\sigma_{y_{x,i}}$ is the error on this average, $\sigma_{y_{x,i}} = \sigma_i/\sqrt{n}$, where σ_i is the standard deviation of the entry values and n is the number of entries in bin i. This contrast with the one dimensional χ^2 algorithm where the error used in the χ^2 calculation is the error on the number of entries, $\sqrt{n}$. For high statistics, the error term in the denominator of the scatter χ^2 algorithm is often very small which can blow up the χ^2. It does not necessarily mean that the run as a problem. There are more fluctuations between runs than predicted from statistical fluctuations alone.

- *Two Dimensional χ^2 Algorithm.* The two-dimensional χ^2 algorithm is slightly different than its one-dimensional counterpart. Instead of calculating an overall χ^2, this algorithm calculates the χ^2 for each individual bin (compared to a reference) and keeps track of the number of bins above some threshold value. The histogram will be flagged YELLOW or RED if the number of bins above that threshold is above a certain value. It is typically 5 bins for YELLOW and 10

for RED. In addition, if any bin has a χ^2 above some maximum, the histogram is automatically flagged RED. This algorithm is only applied to a handful of histograms (mostly the histograms binned in $\eta-\phi$). It can generally be trusted, except at low statistics and at larges values of $|\eta|$. One nice feature of this algorithm is that the $\eta-\phi$ of each flagged bin is printed allowing identification of the problematic region(s).

- *Bin Differences from Strip Median.* For 2 dimensional profile histograms (such as the jet p_T as a function of $\eta-\phi$), for each x-axis slice (strip), a median is calculated, and if any bin has a value some number of times greater than the strip median, the histogram is flagged accordingly. This works best for histograms that are assumed to be symmetric over the y-axis (or ϕ). The thresholds for flagging are usually in the range of 1.6 for GREEN and 3.0 for RED. This means that if a bins value is twice the median of the strip in which it is in, the histogram is flagged YELLOW. This algorithm is reliable, except at low statistics and at large values of $|\eta|$. One nice feature of this algorithm is that the (η,ϕ) of each flagged bin is printed allowing identification of the problematic region(s).

A.4 Jet Cleaning Cuts

While the goal of DQ flags and defects is to identify runs and luminosity blocks in which the jets are problematic, the jet cleaning cuts aim at removing problematic jets at the event level. That is, some jets can be discarded from an event when judged bad without throwing the event away. Such bad jets occur in every run and there are no fixes for it as this comes from detector effects. Examples of such effects are sporadic energy depositions "spikes" in the hadronic end-cap (HEC) or coherent noise in the EM calorimeter that cannot be suppressed. Both effects trigger fake jets. In addition to detector effects there are non-collision backgrounds such as cosmic rays, that can create unwanted jets. Fortunately, these faked and unwanted jets have some features that differentiate them from jets coming from collisions. Jet variables that give a handle on bad jets are the following:

- **EMf (emfrac)** is the fraction of the jet energy in the LAr EM calorimeter;

- **FMax (fracSamplingMax)** is the maximum fraction of the jet energy in one calorimeter layer;
- **HECf** is the fraction of the jet energy in the Hadronic End-Cap (HEC) calorimeter;
- **Q (jet quality)** is the fraction of LAr cells with a cell Q-factor greater than a predetermined threshold. The cell Q-factor is an indicator of the difference between the measured pulse shape and the predicted pulse shape that is used to reconstruct the cell energy;
- **HECq** is the same as Q except calculated only from calorimeter cells in the HEC;
- **NegativeE** is the sum of negative topoclusters in the jets;
- **t (timing)** is the jet time computed as the energy squared cells mean time;
- **n90** is the minimum number of cells containing at least 90% of the jet energy;
- **eta** is the pseudorapidity of the jet at its EM scale;
- **chf** is the jet charged fraction. It is the ratio of the sum p_{T} of tracks associated to the jets divided by the calibrated jet p_{T}.

Figure A.20 shows the conditions for which a jet is flagged as bad. There are three levels of cleaning cuts: loose, medium and tight. The medium and tight cleaning cuts will greatly enhance the purity of the jets at the cost of efficiency.

Another reason why some jets might not be optimal for physics analysis is that they point to a known problematic region of the detector. This can be due to the detector design (gap regions) or known hardware failure (dead regions). Jets that have a fraction of their energy larger than 50% in the Tile gap or from energy corrections to account for dead channels are considered *ugly*. Good jets are jets which are neither bad nor ugly.

	Loose	**Medium= Loose OR**	**Still under discussion Tight= Medium OR**
HEC spikes	HECf>0.5 && |HECQ|>0.5, or |neg. E| >60 GeV	HECf>1-|HECQ|	
EM coherent noise	**EMf>0.95 &&|LArQ| >0.8 && |eta|<2.8**	**EMf>0.9 && |LArQ|>0.8 && |eta|<2.8**	LArQ > 0.95 EMf > 0.98 && LArQ > 0.05
Cosmics & Non collision background	|t|>10 ns or **EMf<0.05 && Chf < 0.05 && |eta| < 2** or EMf<0.05 && |eta| > 2 or FMax > 0.99 && |eta|<2	**EMf<0.05 && Chf < 0.1 && |eta| < 2** or EMf>0.95 && Chf < 0.05 && |eta| < 2	**EMf<0.1 && Chf < 0.2 && |eta| < 2 or EMf<0.1 && |eta| > 2** or EMf>0.9 && Chf < 0.02 && |eta| < 2

Figure A.20: Jet cleaning cuts used for loose, medium and tight jets.

Appendix B

Virtual Flags

This appendix summarizes the composition of the DQ virtual flags used in the top GRLs.

B.1 Muon Virtual Flag

In the case of muon DQ, the CP_MU_MMUIDCB is required to be green. This flag is the result of the logical AND of the following requirements:

- Combined Muon ID Virtual Flag (CP_MU_MMUIDCB)
  - Magnetic Fields (ATLGL, ATLSOL, ATLTOR)
  - Inner Detector (PIX0, PIXB, SCTB, SCTEA, SCTEC, TRTB, TRTEA, TRTEC, IDAL and IDGL)
  - Muon Drift Tubes (MDTBA, MDTBC, MDTEA, MDTEC)
  - Resistive Plate Chambers (RPCBA, RPCBC)
  - Thin Gap Chambers (TGCEA, TGCEC)
  - Cathode Strip Chambers (CSCEA, CSCEC)
  - Combined Muon ID Primary Flag (MMUIDCB)

These flags are obtained both from Muon Spectrometer and muon reconstruction DQ. The detector-related flags are obtained looking at: hit multiplicities and noise levels, noisy and dead channels; spatial and time correlations of the trigger and precision chambers; charge (ADC) and time (TDC) spectra. The higher-level,

reconstruction-related flags (Muon ID flags), are based on: segment and track multiplicity, hit on segment/track multiplicity, hit quality and parameters, hit residuals, pulls, local spatial distributions, chamber and tube efficiencies, track p_{T} and charge ratio.
The available level of segmentation for the detector flags is twofold per each MS region: Side A ($\eta \geq 0$) and C ($\eta \leq 0$) for Barrel (B) and End-Caps (EC). On the other side, the MMUIDCB is evaluated for all the MS at once, allowing to accept only run periods in which the whole MS and ID pseudorapidity range are flagged as green.

B.2 Electron Virtual Flag

There are two virtual flags that indicate the DQ of the electrons used in top analyses, one for the barrel region ($\eta < |1.37|$) and another one for the endcap region ($|1.52| < \eta < |2.47|$). The *crack* region is ignored. The combination of primary flags that enters in each of them is as follows:

- Barrel Electron Virtual Flag (CP_EG_ELECTRON_BARREL)
  - Solenoid Magnetic Field (ATLSOL)
  - Inner Detector (PIX0, PIXB, SCTB, SCTEA, SCTEC, TRTB, TRTEA, TRTEC, IDAL)
  - LAr Barrel (EMBA, EMBC)
  - Tile (TILBA, TIEBA, TILBC, TIEBC)
  - Electron Barrel Primary Flag (EIDB)
- Endcap Electron Virtual Flag (CP_EG_ELECTRON_ENDCAP)
  - Solenoid Magnetic Field (ATLSOL)
  - Inner Detector (PIX0, PIXB, SCTB, SCTEA, SCTEC, TRTB, TRTEA, TRTEC, IDAL)
  - LAr Endcap (EMECA, EMECC, HECA, HECC)
  - Tile (TILBA, TIEBA, TILBC, TIEBC)
  - Electron Endcap Primary Flag (EIDE)

Additionally, there are two further data quality requirements applied for electrons:

- If an electron candidate goes through a dead module of the B-layer, the requirement of having a hit is relaxed.
- Candidate electrons pointing to dead OTX regions according to a look-up map, which is function of the run number, η and ϕ of the electron cluster, cannot make good electrons. For the MC, we use the map of run 159040, and differences with the data should be absorbed by the electron reconstruction.

B.3 Jet Virtual Flag

The overall DQ of the jets for a particular luminosity block is assessed through five DQ virtual flags: one for the barrel ($|\eta| < 1.5$), two for the end caps ($1.5 < |\eta| < 3.2$), and two for the forward regions ($|\eta| > 3.2$). Since jets with $|\eta| > 2.5$ are not used for any of the top analyses, jets will be considered to have good quality when the jet virtual flags for the barrel and the end caps are green. The jet virtual flags themselves are combinations of primary flags:

- Jet Barrel Virtual Flag (CP_JET_JETB)
  - LAr Barrel (EMBA, EMBC)
  - Tile Barrel (TILBA, TILBC, TIEBA, TIEBC)
  - Jet Barrel Primary Flag (JETB)
- Jet End Cap A (CP_JET_JETEA)
  - LAr End Cap A (EMECA, HECA)
  - Jet End Cap A Primary Flag (JETEA)
- Jet End Cap C (CP_JET_JETEC)
  - LAr End Cap C (EMECC, HECC)
  - Jet End Cap C Primary Flag (JETEC)

The detector DQ flags for the LAr and Tile calorimeter are first set by automatic checks and then reviewed by trained shifters and experts. The jet primary flags are set manually by a shifter and reviewed by experts based on the distributions of various observables: calibration factors applied to the jet, uniformity of jet occupancy

in η-ϕ space, fraction of the jet energy deposited throughout the multiple parts of the detector, the topological clusters within the jets, the distance between the two highest-p_{T} jets and additional kinematic quantities. The jet collection used for these distributions is Anti$-k_{\mathrm{T}}4$ at the EM scale. There are no extra jet flags for the other jet collections.

B.4 MetCalo and MetMuon Virtual Flags

Information about whether the $E_{\mathrm{T}}^{\mathrm{miss}}$ was properly reconstructed or not at the bulk level for a given luminosity block is stored in two Data Quality virtual flags, one that considers only contributions from the calorimeters and another that considers only contributions from the muon spectrometer. The primary flags for each of them are:

- $E_{\mathrm{T}}^{\mathrm{miss}}$ Calorimeter Virtual Flag (CP_MET_METCALO)
  - LAr (EMBA, EMECA, HECA, FCALA, EMBC, EMECC, HECC, FCALC)
  - Tile (TILBA, TIEBA, TILBC, TIEBC)
  - $E_{\mathrm{T}}^{\mathrm{miss}}$ Calorimeter Primary Flag (METCALO)
- $E_{\mathrm{T}}^{\mathrm{miss}}$ Muon Virtual Flag (CP_MET_METMUON)
  - Muon Drift Tubes (MDTBA, MDTBC, MDTEA, MDTEC)
  - Resistive Plate Chambers (RPCBA, RPCBC)
  - Thin Gap Chambers (TGCEA, TGCEC)
  - Cathode Strip Chambers (CSCEA, CSCEC)
  - $E_{\mathrm{T}}^{\mathrm{miss}}$ Muon Primary Flag (METMUON)

The detector DQ flags for the LAr, Tile and Muon Spectrometer are first set by automatic checks and then reviewed by trained shifters and experts. The $E_{\mathrm{T}}^{\mathrm{miss}}$ primary flags are set manually by a shifter and reviewed by experts based on the distribution of various $E_{\mathrm{T}}^{\mathrm{miss}}$ related observables: e_{T}, E_{x}, E_{y}, ϕ of $E_{\mathrm{T}}^{\mathrm{miss}}$ and h_{T}. The contribution to these observables coming from different sources, namely, the detectors, the physics objects and the various $E_{\mathrm{T}}^{\mathrm{miss}}$ algorithms (Base, Topo, MuonBoy, RefFinal...) is also monitored.